Effects of Nano-Sized Silicon Carbide Dispersion on Mechanical and Electrical Properties of Yttria Stabilized Zirconia

1998

Noriko Bamba

Department of Materials Chemistry
Faculty of Engineering
Osaka University

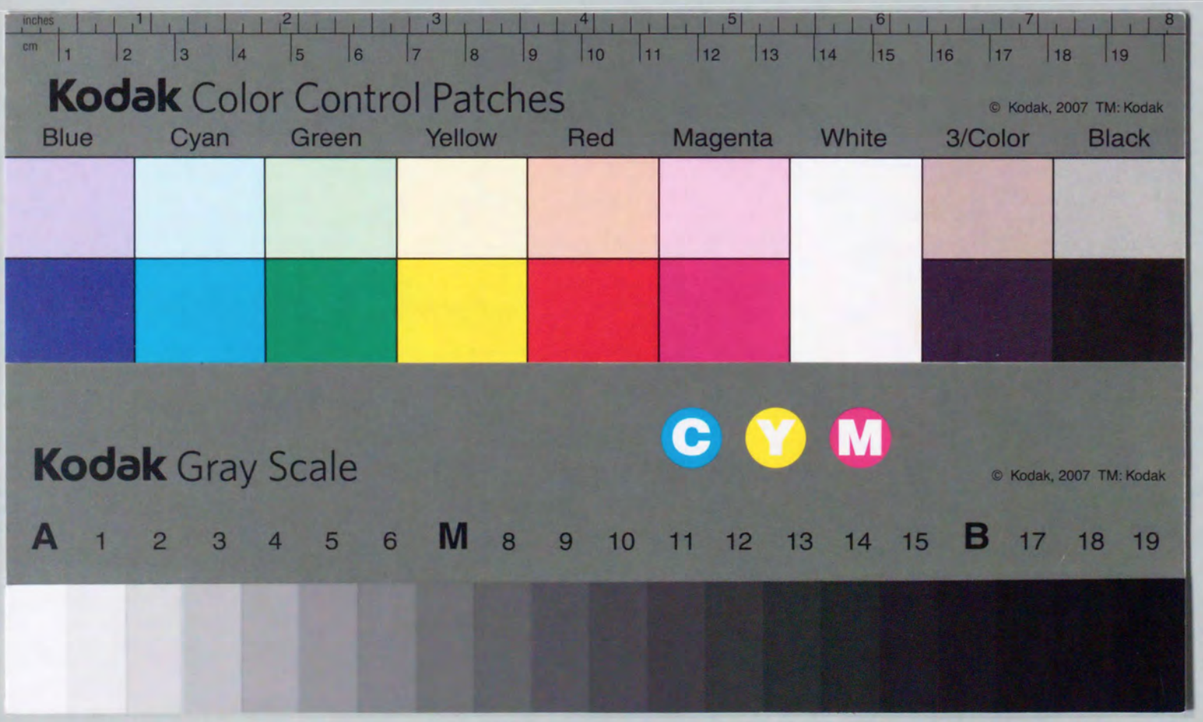

①

Effects of Nano-Sized Silicon Carbide Dispersion on Mechanical and Electrical Properties of Yttria Stabilized Zirconia

(イットリア安定化ジルコニアの機械的・電気的特性に及ぼす炭化ケイ素ナノ分散粒子の影響)

1998

Noriko Bamba

Department of Materials Chemistry
Faculty of Engineering
Osaka University

Contents

1 Introduction

1.1 Ceramics

Ceramics have been expected to be employed as structural materials under severe environments where metals and/or organic macromolecule materials can not be used, because ceramics have high melting point, high chemical resistance and relatively small density. Alumina (Al_2O_3), silicon nitride (Si_3N_4), silicon carbide (SiC) and tetragonal zirconia polycrystal (TZP) are representative structural ceramics, which have been applied to an engine, a cutting tool and a sealing material[1]. Recently, ceramics are developed in various fields such as electric and magnetic materials. Ceramics have played an important role in the industry; Al_2O_3 and mullite ($3Al_2O_3 \cdot 2SiO_2$) have been used as a insulator, zirconia (ZrO_2) as an ionic conductor[2] and some other ceramics, such as barium titanate ($BaTiO_2$), zinc oxide (ZnO) and lead zirconate titanate ($Pb(Zr,Ti)O_3$, PZT), as dielectric substance, semiconductor and piezoelectric ceramic.

Mechanical properties of ceramics strongly depend their atomic bond-state, i.e., ionic or covalent bond. Generally, ceramics have high Young's modulus and strength, in contrast with low fracture toughness, which results in brittle fracture. Such brittle fracture is undesirable, because the material is broken without notice. Thus many attempts have been made to improve fracture toughness of ceramics, including transformation toughening and composite techniques (i.e., second phase materials, such as ceramic fiber and whisker and metal particle reinforce ceramics[3,4]). ZrO_2 is one of materials which effectively utilize transformation toughening.

1.2 Zirconia

1.2.1 Crystallography and Phase Transformation

ZrO_2 was discovered in Brazil as natural mineral, baddeleyite, by Hussak in 1892[5]. It was Ruff and Ebert who first investigated crystal structure of pure ZrO_2, and identified monoclinic phase at low temperature and tetragonal phase at high temperature by using X-ray diffraction in 1929. It has been clear that the phase transformation of pure ZrO_2 occurs reversibly with hysteresis as following Eq. (1-1)[5],

$$\text{Monoclinic} \underset{850\text{-}1000^\circ C}{\overset{1170^\circ C}{\rightleftharpoons}} \text{Tetragonal} \overset{2370^\circ C}{\longleftrightarrow} \text{Cubic} \overset{2680^\circ C}{\longleftrightarrow} \text{Liquid} \qquad (1\text{-}1)$$

Fig. 1-1 shows three ZrO_2 polymorphs[3]. The cubic phase at high temperatures has fluorite-type crystal structure. The tetragonal and monoclinic phase are considered

distortions of the fluorite structure. The representative physical properties of ZrO_2 are summarized in Table 1-1[6]. In addition, Ruff and Ebert also found that phase transformation from tetragonal phase (t-ZrO_2) to monoclinic phase (m-ZrO_2) accompanies disruptive volume change, and that the cubic or tetragonal structure can be stabilized by the addition of CaO. After that, it has been found that various metal oxides also stabilize high-temperature polymorphs. Pure ZrO_2 could not be used for fabricating ceramic forms due to the disruptive volume change. However, adding stabilizer made difficult to occur the disruptive phase transformation during cooling process. Therefore the high temperature cubic fluorite type phase can be maintained at the room temperature.

In particular, Y_2O_3 stabilized ZrO_2 (Y-ZrO_2) system has been extensively studied. Fig. 1-2 shows Y_2O_3-ZrO_2 phase diagram at the ZrO_2-rich end proposed by Scott[7], nevertheless, boundaries among three phases have still uncertain. The hatched region in Fig. 1-2 indicates the nonequilibrium m-ZrO_2-t-ZrO_2 transition. Y-ZrO_2 system has two essential differences from other systems such as Ca-ZrO_2 and Mg-ZrO_2 in terms of transformation-toughening. First, the extent of the tetragonal solid solution range is much larger in the Y-ZrO_2, and second, the temperature of the t-ZrO_2 to m-ZrO_2 transformation is very low.

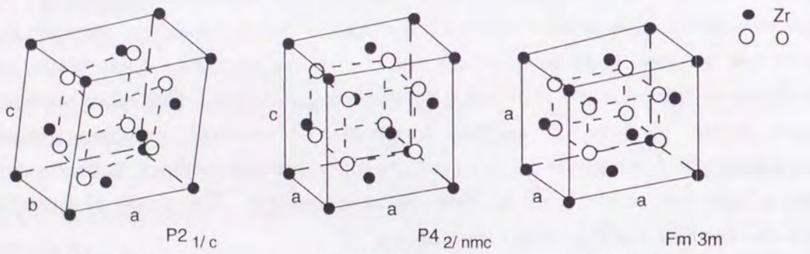

(a) Monoclinic (b) Tetragonal (c) Cubic

Fig. 1-1 Schematic illustrations of the three ZrO_2 polymorphs: (a) monoclinic, (b) tetragonal and (c) cubic. Their space groups are indicated. Black and white spheres correspond to Zr and O atoms.

Table 1-1 The physical properties of ZrO_2[6].

Molecular weight		123.22
Theoretical density	monoclinic	5.84 gcm^{-3}
	tetragonal	6.10 gcm^{-3}
Melting point		2680℃
Boiling point		3730℃
Coefficient of thermal expansion	-130 ~ -80℃	$2 \times 10^{-6} K^{-1}$
	-80 ~ -50℃	$8 \times 10^{-6} K^{-1}$
	500 ~ 1000℃	$8.8 \sim 12 \times 10^{-6} K^{-1}$
Thermal conductivity	1000℃	0.004 $cal \cdot s^{-1} \cdot cm^{-1} \cdot K^{-1}$
	1300℃	0.005 $cal \cdot s^{-1} \cdot cm^{-1} \cdot K^{-1}$

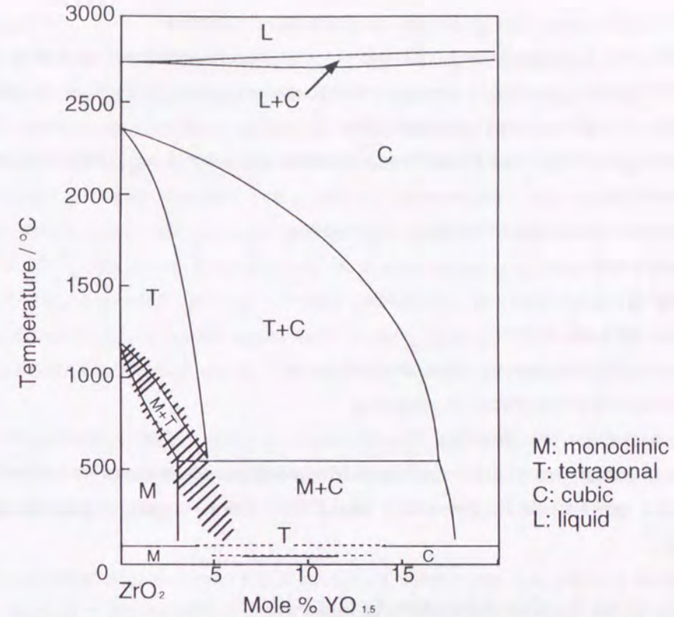

Fig. 1-2 ZrO_2-rich end of the Y_2O_3-ZrO_2 phase diagram. Nonequilibrium homogeneous phases are indicated at the lower margin. Hatched region indicates nonequilibrium monoclinic-tetragonal transition[7].

1.2.2 Phase Transformation Toughening

Garvie et al. reported that it is possible to toughen ZrO_2 by using the phase transformation in 1975[8]. Since their report, ZrO_2 has received much attention for structural materials due to the phase transformation toughening; ZrO_2 has been widely used as not only matrix but also second phase dispersion in composite system. The properties of ZrO_2 and ZrO_2 toughened ceramics (ZTC) strongly depend on the phase transformation, which is affected by the chemical species and content of stabilizer[9]. However, it has been reported that the transformability dramatically decrease with increasing in temperature due to increase in stability of tetragonal phase[10]. On the other hand, Swain et al.[11] suggested the limitation of strength-toughness for ZrO_2 ceramics toughened by transformation, it is difficult to cope with both strength and toughness for transformation toughened materials.

For the transformation toughening, retention of t-ZrO_2 at room temperature is important, because metastable t-ZrO_2 is the toughening agent and the increase in the toughness is caused by the transformation from t-ZrO_2 to m-ZrO_2[12]. Transformation deeply relates to microstructure, i.e., grain size, stabilizer content, thermal history, temperature, impurity and

defect[3,13,14], especially, grain size and stabilizer content.

3 mol% Y_2O_3 doped ZrO_2 (3Y-TZP) is a representative material which exhibits transformation toughening; it has much higher strength and fracture toughness than most other ceramics at ambient temperature.

The strengthening and toughening mechanisms for t-ZrO_2 and ZTC are classified as follows[3,6,15,16],

1. Stress-induced transformation toughening
2. Microcracking
3. Bridging
4. Crack deflection
5. Ferroelastic tetragonal domain switching
6. Surface transformation toughening
7. Residual stress toughening

Although, mechanisms of 2, 3 4 and 7 are observed for other ceramic based materials, those of 1, 5 and 6 are intrinsic for the t-ZrO2 and ZTCs. Each toughening mechanism is indicated as follows.

1. Stress-induced transformation toughening[12]

This toughening mechanism is considered as a dominant mechanism in the transformation toughened materials, and it is used to increase the fracture toughness of ZrO_2 based materials. This mechanism belongs to crack shielding mechanisms[3]. The toughening occurs via the development of transformed zone (process zone) around crack tip. The process zone is a source of stress, in which crack is closed by compressive stresses generated by volume expansion accompanied by the transformation of metastable t-ZrO_2.

The toughness for transformation toughening materials, $K_{IC}{}'$, can be expressed as following equation[17],

$$K_{IC}{}' = K_{IC}{}^{m} + \frac{\eta V_t \Delta V E h^{1/2}}{1-\nu} \qquad (1\text{-}2)$$

where $K_{IC}{}^{m}$, η, V_t, ΔV, E, h and ν are fracture toughness of material surrounding transformed ZrO_2, a constant, volume fraction of t-ZrO_2, coefficient of cubical expansion, Young's modulus, thickness of process zone and Poisson's ratio, respectively. Therefore the increase in thickness of process zone is effective to improve the fracture toughness. The increase in the thickness is caused by enlargement of grain size or decrease in the stabilizer content to a minimum value required to stabilized the t-ZrO_2. However, when transformation occurs too easy, the toughness increases contrary to the decrease in strength, which is caused by the limitation of strength suggested by Swain[11].

2. Microcracking[18]

Microcracking is one of crack-tip shielding toughening mechanisms. Ceramics that contain localized residual stresses are known to be capable of microcracking. Microcrack nucleation becomes more probable as the scale of the residual stress field increases.

During cooling in fabrication process, residual stresses can arise from the various sources. Common sources of these stresses are thermal expansion anisotropy and thermal expansion mismatch between phases or phase transformations. For t-ZrO_2 case, microcrack is classified into three: (i)*preexisting microcracks* generated around transformed ZrO_2 particles(m-ZrO_2 particles) during cooling processes, (ii)*stress-induced microcracks* generated by stress field accompanied with crack propagation and (iii) *microcrack accompanying transformation* generated by expansive strain via transformation from t-ZrO_2 to m-ZrO_2.

Microcrack toughening mechanism is characterized by following three mechanisms: (a)the formation of stress volumetric strain by microcrack formation, (b)the reduction of Young's modulus in process zone and (c)the local decrease in the fracture toughness at crack tip.

According to Evans et al.[19], when the microcrack-zone wake has uniform width and the crack shielding exhibits a steady-state value, microcrack toughening can be approximated by the following expression

$$K_C{}^{\infty}/K_C \approx (1+0.4f_S)+0.25f_S\theta\sqrt{h}E/K_C \qquad (1\text{-}3)$$

where $K_C{}^{\infty}$, K_C, f_S, θ, h and E are the toughness, the base toughness of the material, the volume fraction of microcracks at saturation (microcrack density), the dilatation, the fully developed wake of uniform width and Young's modulus before transformation, respectively. The first term is the toughening that derived from the difference in modulus between the microcrack process zone and the uncracked matrix. This term is independent of the size of the process zone. The second term reflects the influence of the dilatation on the toughness, and depends on the zone width, such that $K_C{}^{\infty} \approx \sqrt{h}$.

As shown in Fig. 1-3[19], the toughness is expected to increase with grain size up to the critical particle size for spontaneous microcracking. For large grains, the material is already microcracked prior to the application of stress, and further toughening will only arise if the microcrack density can increase. Increasing the volume fraction of the microcracks is clearly attractive, however, interaction effects may increase the likelihood of spontaneous transformation and microcrack linking could be a prime source of preexisting flaws in a material. These microcracks do not contribute to crack shielding.

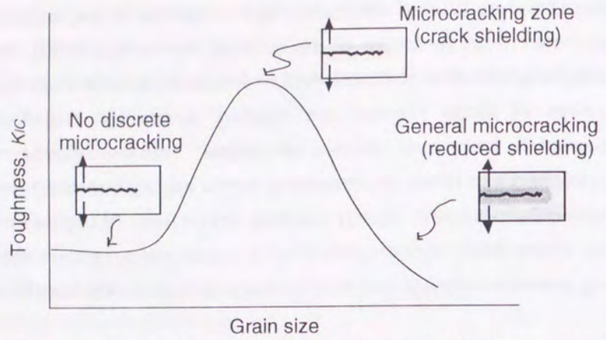

Fig. 1-3 Effects of grain size on toughness of microcracking brittle material.

3. Bridging and pull out

Bridging and pull out toughening mechanism is illustrated in Fig. 1-4. This mechanism can be observed in monolithic ceramics consisted of large grains or anisotropic grains such as Si_3N_4, and composites which are reinforced by whisker, fiber and large particulate. For this mechanism, the interfacial friction between matrix and second phase (bridging material) is important factor, particularly, for pull out. Whisker reinforced composite is focused on to understand bridging and pull out toughening effects. Whisker bridging can occur at the debonded whisker-matrix interface where the crack tip approaches. The crack bypasses the whiskers and leaves them available for load carrying and they completely bridge the crack. Behind the crack tip, the whiskers are pulled out of the matrix as the crack-opening displacement increases, until fracture of whisker. The ensuing failure, however, is not catastrophic as the fibers continue to pull out of the matrix. The toughness increases with increasing in the strength, volume fraction and whisker radius for reinforcing materials. The improvement in toughness, K^{WR}, can be expressed by following Eq. (1-4)[20],

$$dK^{WR} = 2\sigma^{C}(2D_B / \pi)^{1/2} \qquad (1\text{-}4)$$

where σ^C and D_B are the closure stress which is constant within the bridging zone and length of bridging zone, respectively. In general, bridging toughening accompanies crack deflection as explained in following part.

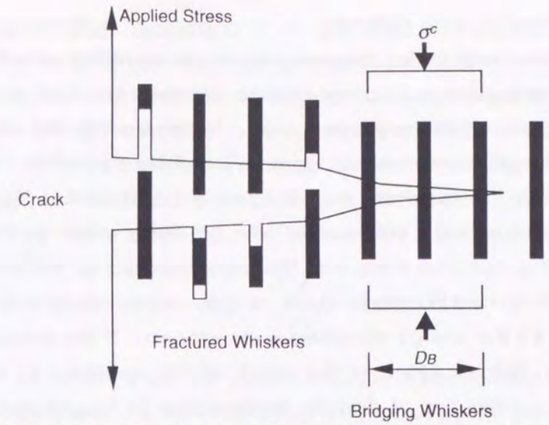

Fig. 1-4 Schematic illustration of whisker bridging zone behind the crack tip. The closure stresses(σ^C) are imposed on the crack surfaces. D_B is the length of bridging zone.

4. Crack deflection[21]

Crack deflection is one of toughening mechanisms; crack can be deflected by localized residual stress or by fracture resistant second phase as shown in Fig. 1-5. The deflection results in a toughening due to the reduced driving force on the deflected portion of the crack. The deflection angles are function of the volume fraction and shape of the deflecting material. The largest deflection angles can be obtained in the case of rods, intermediate in discs and the least in spheres, the toughness increases with increase in

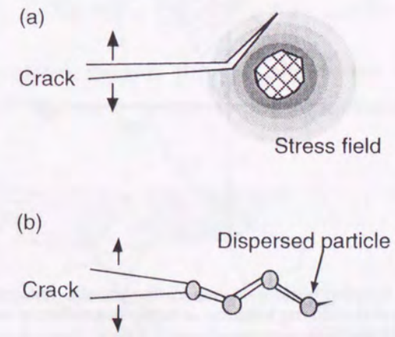

Fig. 1-5 Schematic illustrations for crack deflection by (a) stress field and(b) dispersed particles.

5. Ferroelastic tetragonal domain switching

This toughening mechanism was proposed by Virkar et al.[22], which different from transformation toughening, because of no change of crystal structure in this mechanism; only reorientation occurs within the process zone. Within the stability of the tetragonal phase field, the toughening by ferroelastic domain switching is possible. In the materials exhibits this toughening, the hysteresis loop is observed as shown in Fig. 1-6, and large residual strain can be obtained. Within stress field around a crack tip, if the local stress exceeds σ_c, which is the coercive stress with the area enclosed by the loop representing mechanical energy dissipated in a single cycle, domain reorientation may occur and the shaded area in Fig. 1-6 is the energy absorbed in the process. If the domain reorientation occurs to a distance, h, form plane of the crack tip at the condition of criticality (crack extension), then the contribution of domain reorientation to toughening, ΔG_C, and the toughness, K_C, are given by Eqs. (1-5) and (1-6),

$$\Delta G_C = 2h\int_{\substack{\text{shaded}\\ \text{area}}} \sigma d\varepsilon \qquad (1\text{-}5)$$

$$K_C = K_C^{\,0}\left[1+\frac{2hE}{1-\nu^2(K_C^{\,0})^2}\int_{\substack{\text{shaded}\\ \text{area}}} \sigma d\varepsilon\right]^{1/2} \qquad (1\text{-}6)$$

in which ε is the spontaneous strain, K_C^0 is the toughness in the absence of domain switching, E is Young's modulus of elasticity and ν is Poisson's ratio.

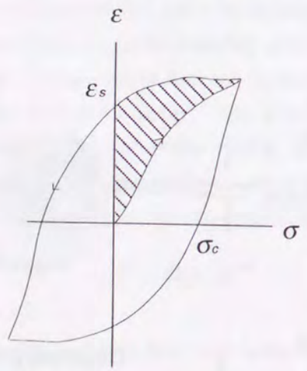

Fig. 1-6 Schematic illustration showing hysteresis loop for ferroelastic material. The shaded area is the energy absorbed in reorientation of domains during fracture. ε_s is the spontaneous strain and σ_c is the coercive stress with the area enclosed by the loop representing mechanical energy dissipated in a single cycle.

6. Surface transformation toughening

The surface transformation toughening is modification for the external surface by the phase transformation. In ceramics containing t-ZrO_2, compressive stresses in the surface layer are produced by the localized volume expansion which can be induced by grinding, sand blasting or a low-temperature treatment as described in Fig. 1-7[16]. Table 1-2 shows some techniques for the introduction of compressive stresses summarized by Claussen et al.[16]. The compressive stress, σ_{com}, can be expressed by following equation,

$$\sigma_{com} = \frac{V_f E}{1-\nu}(e^T - \Delta\alpha\Delta T) \qquad (1\text{-}7)$$

where V_f, E, e^T, $\Delta\alpha$, ΔT and ν are the volume fraction of transformed t-ZrO_2, Young's modulus of transformed layer, the volume change accompanied by the transformation (≈ 0.04), the thermal expansion mismatch between the t-ZrO_2 and the matrix, the temperature difference from temperature starting stress accumulation to room temperature and Poisson's ratio. The fracture strength of a surface-toughened ceramic, σ, can be predicted by Eq. (1-8),

$$\sigma = \frac{K_{IC}}{y\sqrt{\pi a}} + \frac{MV_f E}{1-\nu}(e^T - \Delta\alpha\Delta T) \qquad (1\text{-}8)$$

where K_{IC}, y and a are the fracture toughness of the composite, geometrical factor and flow size, respectively. M is the correction factor, which depends on the ratios of both the flow size and to the thickness of plate is given by Eq. (1-9),

$$M = 1-(2a/\pi s) \qquad 0 \le a \le s \qquad (1\text{-}9)$$

The surface toughening, K_{ST}, can be expressed by the critical stress intensity factor, K_c,

$$K_{ST} = K_{IC} + K_C = K_{IC} + y\sigma_{com}\sqrt{\pi a \cdot M} \qquad (1\text{-}10)$$

The effect of the compressive stresses strongly affects the strength, and thus t-ZrO_2 containing ceramics exhibit high wear resistance and impact resistance by this toughening mechanism.

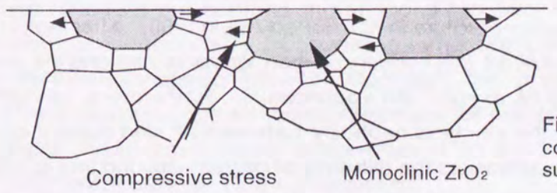

Fig. 1-7 Schematic illustration of the compressive stress imposed on the surface by the phase transformation.

Table 1-2 Possible techniques for introduction of residual compressive stresses[16].

Technique	Transformation induced	Example
Grinding Sand blasting Quenching	By stresses	Al_2O_3-ZrO_2, PSZ*1
Heat treatment in HfO_2 powder in air in vacuum	Chemically	 Al_2O_3-ZrO_2 Si_3N_4-ZrO_2, Mg-PSZ, Mg-CSZ*2
Cooling in liquid He or N_2 for short periods	Low temperature (T_c*3 < M_s*4)	Al_2O_3-ZrO_2
Coating with (a)higher vol. fraction (b)larger particle size	M_s of coating > T*5 M_s of bulk > T	Al_2O_3-ZrO_2

*1: Partially stabilized zirconia.
*2: Cubic stabilized zirconia.
*3: The cooling temperature.
*4: The start temperature of transformation on cooling.
*5: The application temperature.

7. Residual stress toughening[3]

The residual stresses can arise due to thermal expansion anisotropy, thermal expansion mismatch between matrix and second phase or transformed ZrO_2. The stresses affect other toughening mechanism, such as microcracking, crack deflection, however, the stresses have effect of closing cracks directly when the stress are compressive. This toughening mechanism is important in composites incorporating second phase with large mismatch of coefficients of thermal expansion and Young's modulus compared with matrix.

1.2.3 Ionic Conductivity

CaO, MgO, Y_2O_3 and rare earth oxides doped ZrO_2 ceramics exhibit oxygen ionic conduction, which are widely used as a solid oxide electrolytes. It was Nernst who first recognized a conduction at high temperature in Y_2O_3 doped ZrO_2 in 1900. After that, in 1943, Wagner established that the stabilized ZrO_2 contains oxygen ion vacancies and the defects of doped ZrO_2 are composed of oxygen ion vacancies[5]. Furthermore, oxygen ion vacancy is created to achieve the electrical neutrality between Zr^{4+} and dopant cations. The increase in oxygen vacancy enhances the diffusivity of oxygen ion, and thus some ZrO_2 with oxides dopants possess high oxygen ionic conductivity. In the case of Y_2O_3 doped

ZrO_2, oxygen ion vacancies (Vö) are formed as follow;

$$Y_2O_3 \xrightarrow{ZrO_2} 2Y'_{Zr} + V_O^{\cdot} + 3O_O \qquad (1\text{-}11)$$

where Y'_{Zr} and Oo are yttrium (Y) which substituted for zirconium (Zr) having negative charge and oxygen (O) which substituted for O.

The ionic conductivity deeply depends on the temperature, the defect structure and the defect concentration, which are essentially fixed by dopant type and content and are independent of temperature and surrounding atmosphere[23]. The conductivity of doped ZrO_2 follows an Arrhenius behavior over a wide temperature range with activation energy of ≈ 1 eV, which increases with increasing in temperature. On the other hand, the conductivity as a function of dopant content indicates a maximum at or near the lowest dopant concentration required to stabilized the cubic phase (c-ZrO_2), and decreases with increasing dopant concentration as shown in Fig. 1-8[23]. The decrease in conductivity is attributed to defect ordering, clustering, electrostatic interactions, precipitation of a second phase, etc. In addition to the features above mentioned, doped ZrO_2 has thermal and chemical stabilities, and the conduction is truly electrolytic, with the transport number for oxygen ions nearly unity and the transport number for electrons << 1 % at over a wide temperature range.

The ionic conductivity of stabilized ZrO_2 is utilized in a variety of devices. The major applications include an oxygen sensor, an electrochemical oxygen pump, a high temperature fuel cell, a susceptor for induction heating, a resistance heating element, an electrodes for power generation by magnetohydrodynamics, etc.

Y_2O_3 partially and fully stabilized ZrO_2 are one of the most widely used solid electrolytes. This system appears, at present, to have the best combination of electrical and mechanical properties. The use of partially stabilized ZrO_2 arose from an interest in improving the mechanical properties by precipitation hardening a fluorite matrix phase. The presence of a second phase such as t-ZrO_2, however, might be expected to compromise the desired electrolyte conductivity. In addition, for partially stabilized ZrO_2, transformation to m-ZrO_2 results in the degradation of the mechanical properties during cyclic utilization. On the other hand, fully stabilized ZrO_2, for instance, 8 mol% Y_2O_3 stabilized ZrO_2 (8YSZ) which is extensively known as a solid electrolyte in solid oxide fuel cell (SOFC) at high temperatures around 1000°C, is not a strong material and has poor thermal conductivity, in spite of excellent ionic conductivity. Considering some applications, the mechanical properties and the thermal mismatch between electrolyte and other components consist of cell may be solved, because high mechanical stress causes due to stacking which is to obtain high efficiency, the inhomogeneous temperature in the electrolyte and the thermal mismatch between electrolyte and the components.

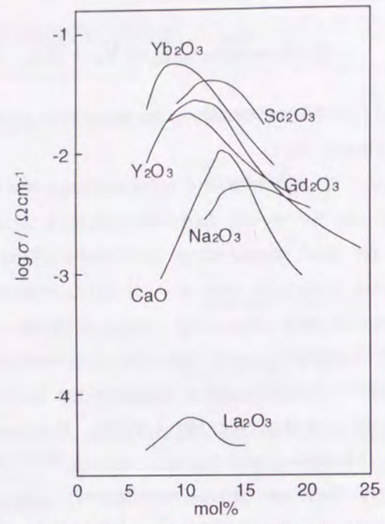

Fig. 1-8 The ionic conductivity of ZrO_2 stabilized with different oxides at 800°C.

1.3 Composites

Ceramic based composites are classified into two: microcomposites and nanocomposites. The former is micro-sized second phase dispersed composites. Whisker, fiber, platelet and micro-sized particle are used as a second phase, which mainly locates at the grain boundaries of matrix. The improvement in fracture toughness by bridging, crack deflection toughening is expected for microcomposites case.

The latter is one of the particulate reinforced composites, in which the nano-sized particulate is dispersed within the matrix grains and/or at the grain boundaries. Nanocomposites are further classified into four types as shown in Fig. 1-9[24], (a) intragranular-type, (b) intergranular-type, (c) intra/intergranular-type and (d) nano/nano-type nanocomposites. Recently various kinds of ceramic based nanocomposites in the ceramic/ceramic[25,26,27,28,29], ceramic/metal[30,31,32,33] and intermetallic/ceramic[34] composite systems have been researched. Of these nanocomposites, the oxide based nanocomposites demonstrated significantly improved mechanical properties even at high temperatures. For example, the fracture strength[25] and creep resistance[2627] of Al_2O_3 were improved by 3 to 5 times and by 3 to 4 orders by incorporating only 5 vol% nano-sized SiC particulate, respectively.

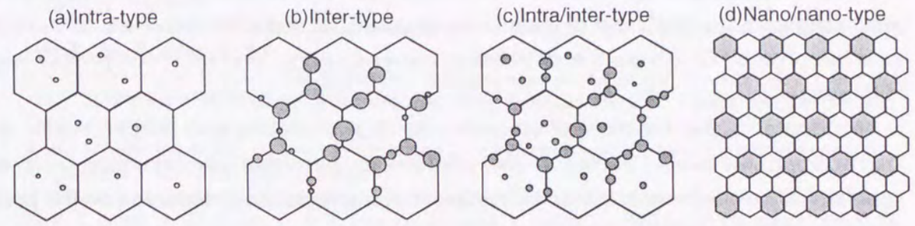

Fig. 1-9 The schematic illustration of typical four types of nanocomposites.

1.4 Purpose

As mentioned above, 3Y-TZP has excellent mechanical properties at ambient temperature. However, degradation of the properties occurs with increasing in temperature. On the other hand, 8YSZ possesses high ionic conductivity, which is widely used as a solid electrolyte, however, its mechanical properties are quite low at both ambient and high temperatures. Thus it is important to improve the mechanical properties for both materials at ambient and high temperatures to widen their applications.

In this study, the improvements in high-temperature strength for 3Y-TZP and the mechanical properties for 8YSZ were attempted by using the nanocomposite technique which is valuable to strengthening and toughening. Nano-sized SiC particulate was selected as a second phase, because SiC possesses high fracture strength at elevated temperatures, high thermal shock resistance and low coefficient of thermal expansion. The purpose of the present work is to investigate the effects of nano-size SiC dispersion on the microstructure including densification and grain growth, and on the mechanical properties for 3Y-TZP and 8YSZ. For 3Y-TZP, the effects of SiC particles on the transformation was also studied because the transformation toughening strongly affects its mechanical properties. Meanwhile, for 8YSZ, the SiC dispersion effect on the ionic conductivity was discussed. To clarify the effects of nano-sized particles, several micro-sized SiC particles dispersed microcomposites was also fabricated and their mechanical properties were evaluated.

The contents of this thesis are as follows.

In this chapter the properties of TZP and fully stabilized ZrO_2, the toughening mechanisms

for transformation materials and related composites and ceramic composites were reviewed and the objective of the present work were described.

In Chapter 2, fabrication processes for ZrO_2 (3Y-TZP and 8YSZ)/SiC nano- and micro-composites were demonstrated, and the effects of nano- and micro-sized SiC particles on densification and grain growth were investigated. The difference of residual stresses, which depends on coefficient of thermal expansion (CTE) mismatch between ZrO_2 and SiC and morphology of SiC particle distribution, between nano- and microcomposites were discussed.

In Chapter 3, the mechanical properties for ZrO_2 monoliths and ZrO_2/SiC nano- and microcomposites were studied. The relationship between microstructure and the mechanical properties was clarified. For 3Y-TZP, the effects of SiC dispersion on the phase transformability were discussed.

In Chapter 4, the high-temperature fracture strength for both 3Y-TZP/SiC and 8YSZ/SiC nanocomposite systems, and toughness for 3Y-TZP/SiC nanocomposite systems were evaluated. The effects of nano-sized SiC particulate on the properties and deformation behavior were discussed.

In Chapter 5, the ionic conductivity for 8YSZ monoliths, 8YSZ/SiC nano- and microcomposites was evaluated by impedance analysis. The effects of SiC dispersion on the grain boundary and lattice conductivity were investigated.

In Chapter 6, the results of present work were summarized.

Reference

1 Y. Moriyoshi, T. Sasamoto, K. Uematsu and Y. Ikuma, Fundamental Science of Ceramics (in Jpn.), Uchida Rokakuho Publishing Co., Ltd., Tokyo, 1990, pp. 113-116.

2 N. Q. Minh, Ceramic Fuel Cell, J. Am. Ceram. Soc., 76 [3](1993) 563-88.

3 D. J. Green, R. H. J. Hannink and M. V. Swain, Transformation Toughening of Ceramics, CRC Press, Inc., Florida, 1989, pp. 57-95.

4 Y. Kagawa and H. Htta, Tailoring Ceramic Composites, Agune Shouhusha, Tokyo, 1990, pp. 124-125.

5 E. C. Subbarao, Zirconia- an overview, in Advance in Ceramics, vol. 3, Science and Technology of Zirconia, Eds. by A. H. Heuer and L. W. Hobbs, Am. Ceram. Soc., Ohio, pp. 1-24.

6 S. Hori, *Kyoujin Zirconia* (in Jpn), Uchida Rokakuho Publishing Co. Ltd., Tokyo, 1990, p.14.

7 H. G. Scott, Phase relationships in the zirconia-yttria system, J. Mater. Sci., 10 [9](1975) 1527-1535.

8 R. C. Garvie, R. H. Hannink and R. T. Pascoe, Ceramic Steel ?, Nature, 258 (1975) 703-704.

9 K. Tsukuma and M. Shimada, Hot isostatic pressing of Y_2O_3 partially stabilized zirconia, Am. Ceram. Soc. Bull., 64 [2](1985) 310-313.

10 K. Nakajima and T. Masaki, High-temperature mechanical properties of Y-PSZ formed by hot isostatic pressing in an oxygen-containing atmosphere, in Advance in Ceramics, vol. 3, Science and Technology of Zirconia, Eds. by A. H. Heuer and L. W. Hobbs, Am. Ceram. Soc., Ohio, pp. 625-633.

11 M. V. Swain and L. R. F. Rose, Strength limitations of transformation-toughened zirconia alloys, J. Am. Ceram. Soc., 69 [7](1986) 511-518.

12 A. G. Evans, D. B. Marshall and N. H. Burlingame, Transformation toughening in ceramics, in Advance in Ceramics, vol. 3, Science and Technology of Zirconia, Eds. by A. H. Heuer and L. W. Hobbs, Am. Ceram. Soc., Ohio, pp. 202-216.

13 F. F. Lange, Transformation toughening part 1 size effects associated with the thermodynamics of constrained transformations, J. Mater. Sci., 17 (1982) 225-234.

14 I. W. Chen, Y. H. Chiao and K. Tsuzaki, Statistics of martensitic nucleation, Acta Metall., 33 [10](1985) 1847-1859.

15 A. G. Evans and R. M. Cannon, Toughening of brittle solids by martensitic transformations, Acta Metall., 34 [5](1986) 761-800.

16 N. Claussen and M. Rühle, Design of transformation-toughened ceramics, in Advances in Ceramics, vol. 3, Science and Technology of Zirconia, Eds. by A. H. Heuer and L. W. Hobbs, Am. Ceram. Soc., 1982, pp. 137-163.

17 R. M. McMeeking and A. G. Evans, Mechanics of transformation-toughening in brittle materials, J. Am. Ceram. Soc., 65 [5](1982) 242-246.

18 D. J. Green, Microcracking mechanisms in ceramic, in Fracture Mechanics of Ceramics, vol. 5, Eds. by R. C. Bradt, A. G. Evans, D. P. H. Hasselman and F. F. Lange, Plenum Press, New York, 1983, pp. 457-478.

19 A. G. Evans and K. T. Faber, Crack-growth resistance of microcracking brittle materials, J. Am. Ceram. Soc., 67 [4](1984) 255-260.

20 P. F. Becher, C. H. Hsueh, P. Angelini and T. N. Tiegs, Toughening behavior in whisker-reinforced ceramic matrix composites, J. Am. Ceram. Soc. 71 [12](1988) 1050-1061.

21 K. T. Faber and A. G. Evans, Crack deflection processes -I. theory, Acta Metall., 31 [4](1983) 565-576.

22 A. V. Virkar and R. L. K. Matsumoto, Ferroelastic domain switching as a toughening mechanism in tetragonal zirconia, J. Am. Ceram. Soc., 69 [10](1986) C224-C226.

23 Y. Saito, Electrical conduction of stabilized zirconia and oxygen sensor, in Zirconia Ceramics, vol. 1, *Uchida Rokakuho* Publishing Co., Ltd., Tokyo, 1983, pp. 109-125.

24 K. Niihara, New design concept of structural ceramics-ceramic nanocomposites. J. Ceram. Soc. Jpn., 99 [10](1991) 974-982.

25 K. Niihara, A. Nakahira, T. Uchiyama and T. Hirano, High-temperature mechanical properties of Al_2O_3-SiC composites, in Fracture Mechanics of Ceramics, vol. 7 Eds. by R. C. Bradt, A. G. Evans, D. P. H. Hasselman and F. F. Lange, Plenum Press, New York, 1986, pp. 103-116.

26 A. Nakahira and K. Niihara, Microstructure and fracture behaviors at high temperatures for Al_2O_3-SiC nanocomposites, in Fracture Mechanics of Ceramics, vol. 9 Eds. by M. Sasaki, R. C. Bradt, D. P. H. Hasselman and D. Munz, Plenum Press, New York, 1992, pp. 165-178.

27 T. Ohji, A. Nakahira, T. Hirano and K. Niihara, Tensile creep behavior of alumina/silicon carbide nanocomposite, J. Am. Ceram. Soc., 77 [12](1994) 3259-3262.

28 E. Yasuda, Q. Bao and K. Niihara, The effects of fine SiC particles on the creep of MgO at high temperatures, J. Ceram. Soc. Jpn., 100 [4](1992) 514-519.

29 G. Sasaki, H. Nakase, K. Suganuma, T. Fujita and K. Niihara, Mechanical properties and microstructure of Si_3N_4 matrix composite with nano-meter scale SiC particles, J. Ceram. Soc. Jpn., 100 [4](1992) 536-540.

30 T. Sekino, A. Nakahira, M. Nawa and K. Niihara, Fabrication of Al_2O_3/W nanocomposites, J. Jpn. Soc. Powder Powder Metall., 38 (1991) 326-330.

31 M. Nawa, T. Sekino and K. Niihara, Fabrication and mechanical behavior of Al_2O_3/Mo nanocomposites, J. Mater. Sci., 29 (1994) 3185-3192

32 T. Sekino and K. Niihara, Microstructural characteristics and mechanical properties for Al_2O_3/metal nanocomposites, Nanostruct. Mater., 6 (1995) 663-666.

33 M. Nawa, K. Yamazaki, T. Sekino and K. Niihara, Microstructure and mechanical behavior of 3Y-TZP/Mo nanocomposites possessing a novel interpenetrated intragranular microstructure, J. Mater. Sci., 31 (1996) 2849-2858.

34 A. Nakahira, H. Tamada and K. Niihara, Microstructure and mechanical properties of Ti-Al based composites, J. Jpn. Soc. Powder Powder Metall., 41 (1994) 514-517.

2 Fabrication, Microstructure and Residual Stresses of ZrO_2/SiC Composites

2.1 Introduction

3 mol% Y_2O_3 doped tetragonal ZrO_2 (3Y-TZP) is a representative structural material and has excellent mechanical properties due to the transformation toughening from tetragonal (t-) to monoclinic (m-) ZrO_2[1]. However, transformation toughening is only effective at ambient temperature. The rapid degradation of mechanical properties can be observed with increasing temperature employed, because the transformation toughening effect decreases at higher temperatures due to the increase in stability of t-ZrO_2[2]. Many attempts have been made to resolve this degradation of 3Y-TZP, for example, by dispersing second phase materials such as whiskers, platelets, fibers or particles with high Young's modulus[3,4,5,6,7,8]. In addition, composite techniques have been also applied to improve the poor mechanical properties of 8 mol% Y_2O_3 fully stabilized ZrO_2 (8YSZ) [9,10,11], which is well-known as a solid electrolyte with high oxygen ionic conductivity over wide ranges of temperature and oxygen partial pressure[12,13,14]. It is expected that the improvement in mechanical properties at both ambient and elevated temperatures widens the application for both 3Y-TZP and 8YSZ.

Conventional composite technique that micro-sized secondary reinforcing phases are dispersed into matrix (denoted by microcomposites) is one of the most effective methods to improve mechanical properties, especially fracture toughness, and widely used. In such a composite, the micro-sized second phase are predominantly located at grain boundaries of the matrix grains. However, the improvement has not been sufficient in these microcomposites. Recent researches exhibit that ceramic composites incorporating nano-size particulate within matrix grains and/or at the grain boundaries (nanocomposites) possess excellent mechanical properties at both room and high temperatures[15,16]. In the nanocomposite systems, it has been reported that dispersing ultra-fine (50-300 nm) second phase particles with lower coefficient of thermal expansion (CTE) into the matrix with higher CTE contributes significant strengthening. In composite materials, the stresses depending on the CTE mismatch arise in all over matrix and dispersed second phase[17,18,19]. In addition, other stress and strain are generated due to constriction by neighbor grains for polycrystalline materials, which are called nonuniform stress and strain[20]. Both stresses and strains are generated in cooling process from sintering temperature to room temperature. It has been reported that these stresses and strains contribute to strengthening and toughening of ceramic composites.

In this work, nanocomposite technologies are applied to both 3Y-TZP and 8YSZ in order to improve mechanical properties at ambient and elevated temperatures. Nano-sized SiC particulate is used as a second phase, because SiC has much lower CTE, higher Young's modulus than 3Y-TZP and 8YSZ and excellent mechanical properties at not only room temperature, but also high temperatures. It will be effective to improve their mechanical properties.

In this chapter, first, the details of the fabrication process of ZrO_2 (3Y-TZP and 8YSZ)/SiC composites were described. Second, the sintering behavior and microstructure of ZrO_2 monoliths and ZrO_2/nano-sized SiC composites (nanocomposites) were investigated, because they are essential parameters in order to understand toughening and strengthening mechanisms and other properties. In addition, to make clear effects of nano-sized SiC particles on the microstructure, nanocomposites were compared with micro-size SiC dispersed ZrO_2 composites. Furthermore the stresses and strains generated in fabrication processes were also discussed.

2.2 Residual Stress and Strain

There has been increased interest in strengthening and toughening polycrystalline ceramics by incorporating particles or whiskers within the matrix. With incorporating a second phase which has different thermal expansion from matrix, the stresses arise in the material, which influence the mechanical properties such as toughness and strength. The differences in not only the thermal expansion but also the elastic constants (Young's modulus) of matrix and second phase result in generation of stresses. These stresses are imposed all over the material, which are classified uniform stresses, and thus the uniform strains arise in lattice. On the other hand, the nonuniform stresses and strains which are produced by the restraint by its neighbor also impose the material, even monolith. Uniform and nonuniform strains are described as follows and shown in Fig. 2-1[20]. The both stresses and strains can be measured by X-ray diffraction analysis[21,22,23,24,25]

Uniform strain: If the grain is given a uniform tensile strain at right angles to the reflecting planes, their lattice spacing becomes larger than original spacing, d_0, and the corresponding diffraction peak shifts to lower angles but no shape change (Fig. 2-1 (b)). The uniform strain is generated by machining stress and/or thermoelastic stresses which can be calculated by using the difference of CTE, $\Delta\alpha$, and Young's modulus, ΔE, between matrix and second phase. The thermoelastic stresses also influence the nonuniform stress and generate the localized stresses.

Nonuniform strain: It is generated by the nonuniform stress, which is localized and different from neighbors, depending on grain size, crystal structure and geometry as explain following. The change in shape of any grains, is determined not only by the uniform stress applied to whole material, but also by the fact that each grain retains contact on its boundary surfaces with all its neighbors because of this interaction between grains. Nonuniform stress generates mainly at grain boundary and as a result of the restraint by its neighbors and forms a gradient of stress field. A plastically deformed grain in a solid aggregate usually has regions of its lattice left in an elastically bent or twisted condition and imposed nonuniform strain, that is, grain is bent and the strain is nonuniform (Fig. 2-1 (c)); the lattice spacing on the top (tension) side exceeds d_0, while that on the bottom (compression) side is smaller than d_0. This grain is composed of a number of small regions with different lattice spacing, and as a whole, the broadened diffraction line is observed.

The nonuniform stresses and strains are enhanced by incorporating second phase with different character. Such difference of CTE, Young's modulus, sintering rate, diffusion rate between matrix/matrix and matrix/second phase should cause difference of relaxation.

According to Choa[26], ΔT, the temperature change from the temperature at which stresses begin to be accumulated in the material to room temperature, depends on a kind of creep processes as described in Fig. 2-2. The detail of stress accumulation mechanism is explained as follows: although the stresses and strains are generated during cooling in sintering process, the stress relaxation by diffusional creep processes also occurs during cooling. Lattice and grain boundary diffusional creep are important factors to relax the stresses. In addition, slip or grain boundary sliding which are described in Chapter 4 may be important factors of stress relaxation at high temperatures. Only diffusional creep mechanisms, however, are considered as stress relaxation mechanism, because the grains are constrained and continuous sliding without diffusion can not take place as long as the grain boundaries remain coherent in dense polycrystalline. In cooling process from sintering temperature, the stress relaxation by the lattice diffusional creep stops at first, and then, the relaxation by grain boundary diffusional creep stops at lower temperatures. Thus the stress is gradually accumulated with decreasing temperature.

Three kinds of typical materials are shown in Fig. 2-2: a single phase polycrystalline material, a microcomposite and a nanocomposite which have two phases with different properties. For single phase polycrystalline material, nonuniform stresses arise in polycrystalline material due to thermoelastic factor and constraint by anisotropy of grains and neighbors, however, amount of the stresses is influenced on its anisotropy. The stresses increase with increasing grain size. In monolithic case, grain boundary diffusional creep may be dominant mechanism to relax any stresses developed.

For microcomposite, second phase materials are mainly located at grain boundary of the matrix as illustrated. The thermoelastic differences between matrix and second phase

should become larger compared with those between matrix and matrix. They enhance not only uniform stress, but also the nonuniform stress generated at the grain boundaries. Internal stress of second phase may be relaxed mainly by grain boundary diffusional creep mechanism of matrix.

For nanocomposite, the internal stresses in matrix grains and dispersed second phase particles within matrix grains could be relaxed by both grain boundary and lattice diffusional creep mechanisms. The lattice diffusion is usually active at temperatures several hundred degrees higher than the grain boundary diffusion, therefore, the relaxation by the former stops higher temperature than that by the latter during cooling down process. The internal stresses for matrix grains incorporating second phase are always higher than those for intergranular dispersion, unless other relaxation mechanisms work. In addition, composite materials display that the diffuison in matrix/second phase interface is depressed[27], which exhibits significantly higher creep resistance[28].

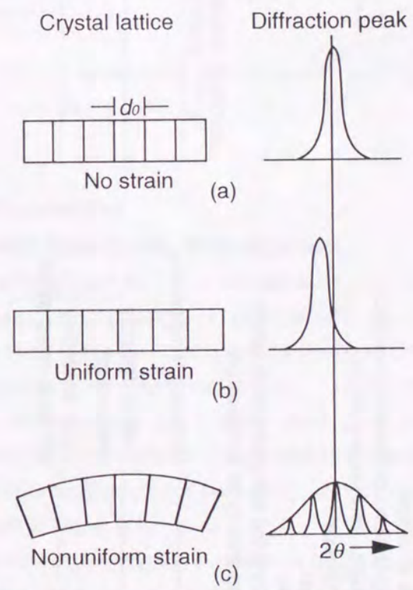

Fig. 2-1 Effect of lattice strain on diffraction peak width and position.

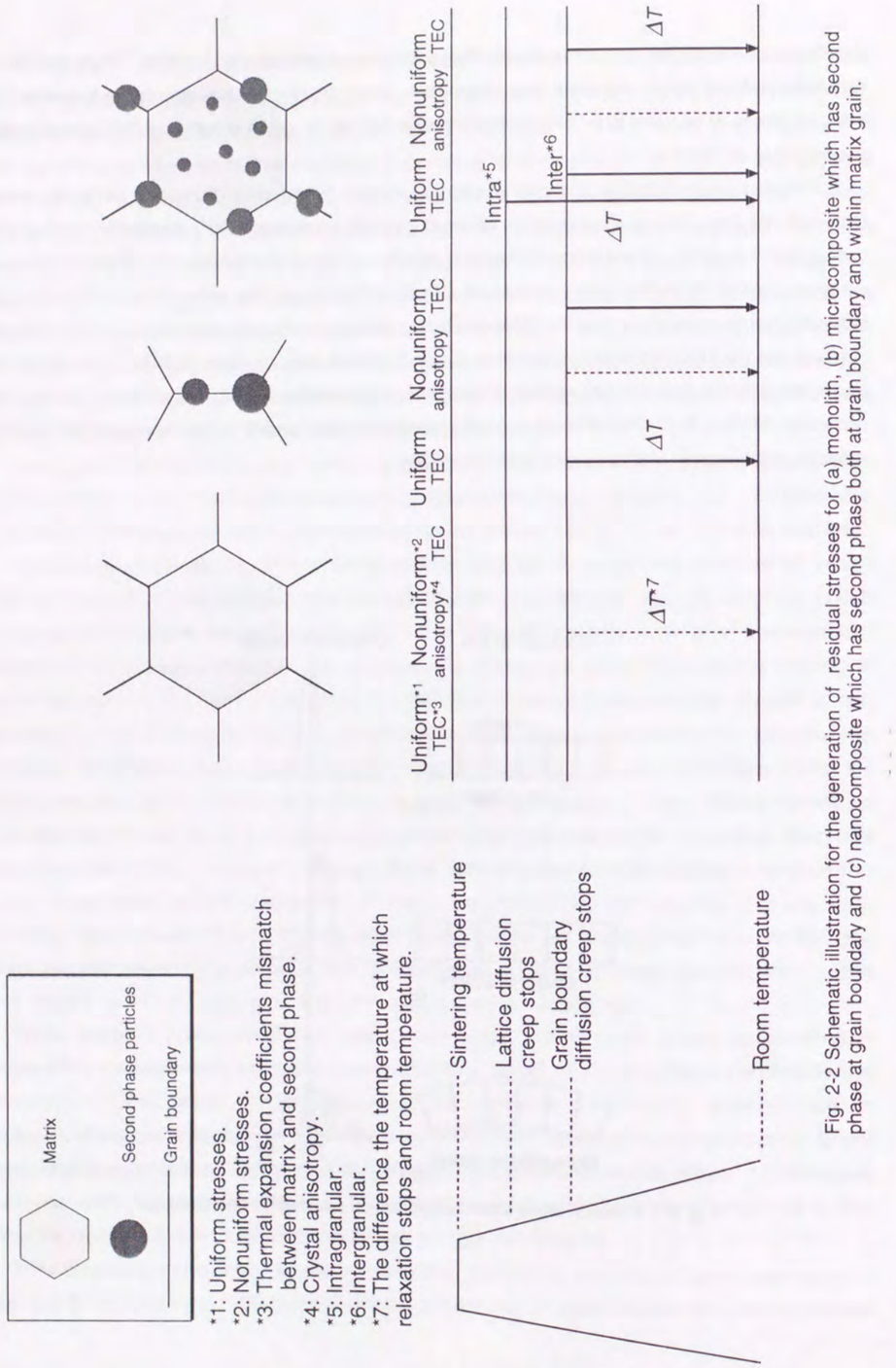

*1: Uniform stresses.
*2: Nonuniform stresses.
*3: Thermal expansion coefficients mismatch between matrix and second phase.
*4: Crystal anisotropy.
*5: Intragranular.
*6: Intergranular.
*7: The difference the temperature at which relaxation stops and room temperature.

Fig. 2-2 Schematic illustration for the generation of residual stresses for (a) monolith, (b) microcomposite which has second phase at grain boundary and (c) nanocomposite which has second phase both at grain boundary and within matrix grain.

In fact, the stresses depend on the $\Delta\alpha$ and ΔE can be calculated by using following Eq. (2-1)[18]

$$\sigma_m = \frac{2 f_p \beta \alpha_1^*}{(1-f_p)(\beta+2)(1+\nu_m)+3\beta f_p(1-\nu_m)} E_m \tag{2-1}$$

$$\sigma_p = \frac{-2(1-f_p)\beta \alpha_1^*}{(1-f_p)(\beta+2)(1+\nu_m)+3\beta f_p(1-\nu_m)} E_m$$

where σ, f, α_1^*, E and ν are the average stress, the volume fraction, the CTE misfit strain, Young's modulus, Poisson's ratio, and subscripts p and m indicate dispersed particulate and matrix, respectively; α_1^*, β are expressed by Eqs. (2-2) and (2-3),

$$\alpha_1^* = \int_{T_P}^{T_R} (\alpha_p - \alpha_m)\delta dT \tag{2-2}$$

$$\beta = \frac{1+\nu_m}{1-2\nu_p} \cdot \frac{E_p}{E_m} \tag{2-3}$$

where T_P, T_R, α and δ denote processing temperature, room temperature, CTE and the isotropic tensor (Kronecker's delta), and $\Delta T = T_P - T_R$.

2.3 Experimental Procedure

2.3.1 Fabrication and Specimen Preparation

3 mol% and 8 mol% Y_2O_3 doped ZrO_2 powders with an average crystalline size of 20 nm (Sumitomo Osaka Cement Co. Ltd.) and β-SiC powder with average particle size of 150 nm (Mitsui touatsu Kagaku Ltd.) were used as a matrix and a second phase to fabricate the 3Y-TZP/SiC and 8YSZ/SiC nanocomposites, respectively. Furthermore, SiC powders with 1.2, 4.0 and 30 μm (Fujimi Abrasives Co. Ltd.) were used as a second phase to fabricate microcomposites in order to confirm effects of dispersed second phase size on densification, microstructure and mechanical/electrical properties of composites. The details of the powders used are shown in Table 2-1.

Fig. 2-3 indicates the overall fabrication procedure adopted in this study. 3Y-TZP or 8YSZ and SiC powders were mixed by conventional wet ball-milling method in EtOH using zirconia balls. Ball-milling time for nanocomposites, 1.2, 4.0 and 30 μm microcomposites, was 48 h, 3 h, 1 h and 2 h, in order to ensure the homogeneity, respectively. After wet ball-milling, the mixed powders were dried, then the powders were dry-ball milled for 12 h,

3 h, 1 h, and 2 h to eliminate agglomerated powders, respectively.

The mixed powders were placed in a graphite die coated with BN slurry to avoid reaction between the powder and die. Hot pressing was performed in Ar atmosphere under 30 MPa of applied pressure for 1 h at temperature range from 1350 to 1850°C for 3Y-TZP system and from 1300 to 1900°C for 8YSZ system, respectively. The details of hot pressing program is shown in Fig. 2-4. The heating rate was 20°C/min from room temperature to sintering temperature. In order to eliminate residual humidity from the powder, it was kept at 500°C for 40 min in vacuum condition. The pressure of 30 MPa was applied after holding at 500°C, and then Ar gas was introduced at 1100°C. After holding the specimen at the hot pressing temperature for 1 h, the specimen was cooled down to 1100°C with 20°C/min in cooling rate, and then, the electric power of furnace was turn off. The samples were cooled inside the furnace cooling and applied pressure was released at 400°C. The obtained hot pressed samples which were 44 mm in diameter 5 mm in thickness were cut with a diamond saw, ground with a diamond whetstone and polished with 0.5 μm diamond slurry to rectangular bars with 3 x 4 x 36 mm. Surface of perpendicular direction to hot-pressing direction was used for various evaluations for mechanical properties.

Table 2-1 Characteristics of ZrO_2 (3Y-TZP and 8YSZ) and β-SiC powder used.

	Average grain size / μm	Major impurities / wt%
3Y-TZP(3 mol% Y_2O_3)*1	0.023#	Al_2O_3:0.0007, SiO_2:0.0027, Fe_2O_3:0.0006, TiO_2:0.0006, Na_2O:0.0003, Cl:0.0103,
8YSZ(7.97 mol% Y_2O_3)*1	0.019#	Al_2O_3:0.0024, SiO_2:0.0054, Fe_2O_3:0.0005, TiO_2:0.0001, Na_2O:0.0011, Cl:0.0086,
Nano β-SiC*2	0.15	SiO_2:0.12, free-C:0.10 Fe:0.019, Cr:0.007, Al:0.003 Ca:<0.002
Micro β-SiC (#8000)*3	1.2	free-C:2.0, Fe:0.3
Micro β-SiC (#3000)*3	4.0	free-C:2.0, Fe:0.3
Micro β-SiC (#400)*3	30	free-C:0.5, Fe:0.3

*1: Sumitomo Osaka Cement Co., Ltd. (Japan)
*2: Mitsui Touatsu Kagaku Ltd. (Japan)
*3: Fujimi Abrasives Co., Ltd. (Japan)
#: Crystalline size measured by X-ray diffraction

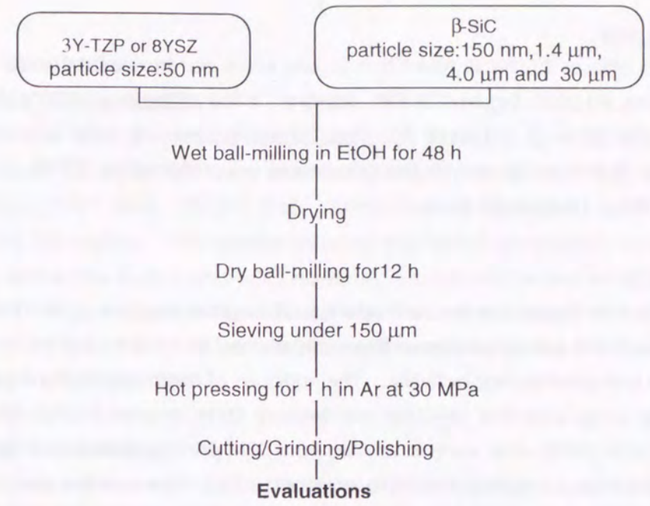

Fig. 2-3 Fabrication procedure for 3Y-TZP/SiC and 8YSZ/SiC nano- and microcomposites.

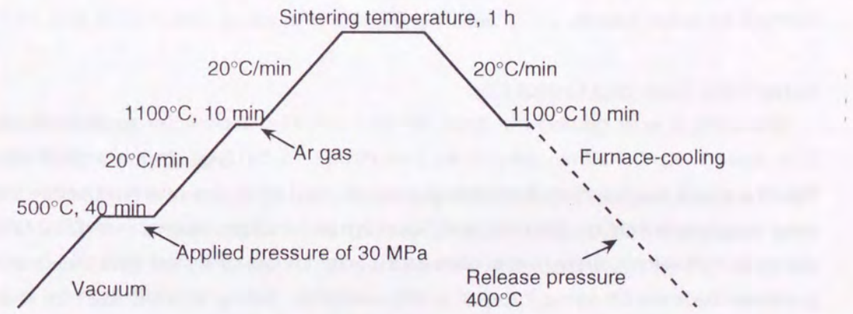

Fig. 2-4 Hot pressing program

2.3.2 Evaluation

Relative density

Density of the specimen was measured by the Archimedes method using toluene at room temperature. The relative density was determined by dividing the apparent density by the theoretical density which was calculated assuming the specific gravity of 3Y-TZP, 8YSZ and β-SiC to be 6.08, 5.96 and 3.22 g/cm^3, respectively.

Characterization

Crystalline phases of the sintered specimens were determined by x-ray diffractometry (50 kV, 150 mA, RU-200B, Rigaku Co. Ltd., Japan). X-ray diffraction (XRD) pattern was taken using CuKα radiation (λ = 1.5418 Å). The 2θ angle scanning rate was 4°/min, and the identification of phases present in the specimens was referred to JCPDS (Joint Commit of Power Diffraction standards) data.

Microstructure

In order to investigate the microstructure such as grain structure or distribution of second phase addition, the specimens were thermally etched at 1300 to 1450°C in air for monolith and in Ar for composites, respectively. The surfaces of thermally etched specimens were observed by using scanning electron microscopy (SEM, model S-5000, Hitachi Co. Ltd.). Grain size and its distribution were analyzed from SEM photographs by using image analysis technique (NIH image, National Institute of Health, USA). Transmission electron microscopy (TEM, H-8100, Hitachi Co. Ltd.) was used at an accelerating voltage of 200 kV to observe the distribution of SiC particles. TEM samples were prepared using conventional thinning procedure, that is, mechanically grinding down to 150 μm, and then, drilling by using ultrasonic to obtain 3 mm diameter discs. The obtained thin discs were dimpled and finally thinned by Ar ion beam.

Nonuniform Strain and Crystal Size

XRD analysis was carried out from 45° to 110° using Si powder as an internal standard. Scan speed was 0.30°/min using CuKα radiation(λ = 1.5418Å). In this work, it was assumed that the peak broadening depended on both crystalline size and nonuniform strain, which were approximated by Cauchy and Gauss types functions, respectively[23,24,25]. Crystal size and nonuniform strain were calculated from peaks of Si and 8YSZ ($Y_{0.15}Zr_{0.85}O_{1.93}$) in XRD pattern obtained by using integral width method. Integral width can be expressed by following Eq. (2-4),

$$\frac{(d2\theta)^2}{\tan^2\theta_0} = \frac{K\cdot\lambda}{L}\cdot\frac{d2\theta}{\tan\theta_0\cdot\sin\theta_0} + 16\cdot e^2 \qquad (2\text{-}4)$$

where θ, θ_0, L and e are Bragg angle, angle of diffracted beam, crystal size and strain, and K is 1.07, respectively. When $(d2\theta/\tan\theta_0)^2$ is plotted against $d2\theta/(\tan\theta_0 \sin\theta_0)$ for some diffracted beams, crystal size and nonuniform strain can be obtained from an intercept and slope.

2.4 Results

2.4.1 Phase Analysis

2.4.1.1 3Y-TZP/SiC Composites

3Y-TZP monolith, 3Y-TZP/3-20 vol% SiC nanocomposites (denoted by 3Y3S, 3Y5S, 3Y10S and 3Y20S) and 5 and 20 vol% SiC with average particle size of 1.2, 4.0 and 30 μm microcomposites (3Y5*1.2SM, 3Y20*1.2SM, 3Y5*4.0SM, 3Y20*4.0SM, 3Y5*30SM and 3Y20*30SM) were fabricated. XRD analysis showed that all the composites were consisted of mainly t-ZrO_2 and a little m-ZrO_2 and β-SiC, however, no reaction phase were observed as shown in Fig. 2-5. High resolution transmission electron microscopic (HRTEM) image as shown in Fig. 2-6 also exhibited that no reaction phases existed at the interface between 3Y-TZP matrix grain and SiC particle.

2.4.1.2 8YSZ/SiC Composites

XRD analysis showed that all the composites were composed of only $Y_{0.15}Zr_{0.85}O_{1.93}$ and β-SiC, and free from reaction phases as shown in Fig. 2-7. The HRTEM of the 8YSZ/5 vol% SiC nanocomposite (8Y5S) sintered at 1700°C (8Y5S1700) indicated that no reaction phases existed at the interface between 8YSZ grain and SiC particle as shown in Fig. 2-8 similar to 3Y-TZP/SiC composite system. In the HRTEM image, glassy phase existed at the triple points consisted from two 8YSZ matrix grains and one SiC particle.

2.4.2 Densification

2.4.2.1 3Y-TZP/SiC Composites

Fig. 2-9 (a) indicates the variation of relative density with sintering temperature for 3Y-TZP monolith and 3Y5S, 3Y10S and 3Y20S. The density of each composition increased with increase of the sintering temperature. The densification was depressed by SiC addition, however, fully densified body could be obtained in each composition. The sintering temperature for obtaining fully densified body became higher with increasing SiC content. For monolith, fully dense sample was obtained at 1450°C, while 1500°C, 1600°C and 1750°C were required for 3Y5S, 3Y10S and 3Y20S, respectively. For microcomposites except for 3Y20*30SM, about 99.8 % of theoretical density can be obtained as shown in Table 2-2. The relative density of 3Y20*30SM was 98.9 %, and this should be due to microcracking as shown in Fig. 2-10.

2.4.2.2 8YSZ/SiC Composites

Figure 2-9 (b) shows the variation of relative density with the sintering temperature for the 8YSZ monolith, 8Y5S and 8YSZ/20 vol% SiC nanocomposites (8Y20S). Relative densities of microcomposites incorporating 5 and 20 vol% of 1.2 μm SiC particulate (8Y5SM and 8Y20SM)

were also displayed in same figure. Higher sintering temperatures were necessary to densify the mixed powders incorporating fine SiC particles, compared with the monolith, for instance, 1600°C and 1800°C are required for 8Y5S and 8Y20S to obtain over 99.9 % of the theoretical density, respectively. Thus SiC dispersion inhibited the densification of 8YSZ matrix obviously. In 8YSZ system, the decrease in the density was observed for monolith sintered at 1600°C. This is due to overfiring in which pores are trapped into matrix grain at higher sintering temperature, different from 3Y-TZP system[29,30]. For 8Y5S and 8Y20S, however, no intragranular-pore was observed.

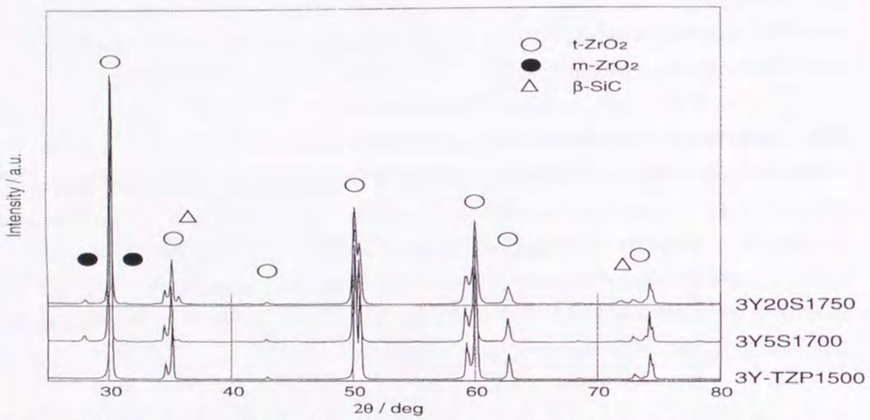

Fig. 2-5 X-ray diffraction pattern for 3Y-TZP monolith sintered at 1500℃ (3Y-TZP1500), Y-TZP/5 vol% SiC nanocomposite at 1700℃ (3Y5S1700) and 3Y-TZP/20 vol% SiC at 1750℃ (3Y20S1750).

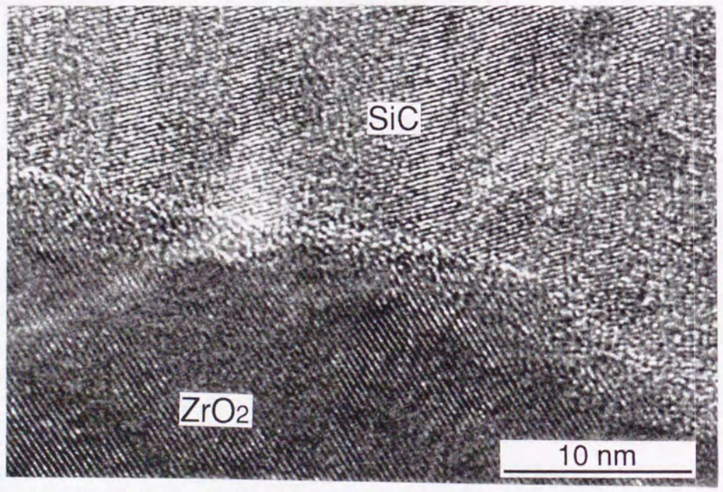

Fig. 2-6 HRTEM image of 3Y-TZP/5 vol% SiC nanocomposite sintered at 1700℃.

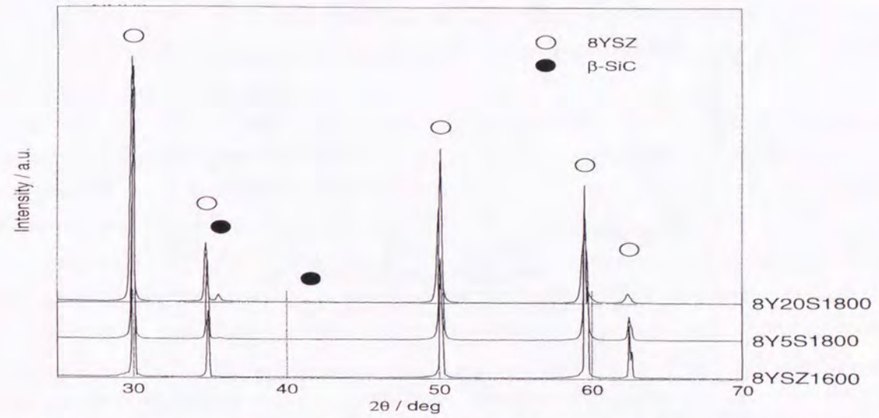

Fig. 2-7 X-ray diffraction pattern for 8YSZ monolith sintered at 1600℃ (8YSZ1600), 8YSZ/5 vol% SiC nanocomposite at 1800℃ (8Y5S1800) and 8YSZ/20 vol% SiC at 1800℃ (8Y20S1800).

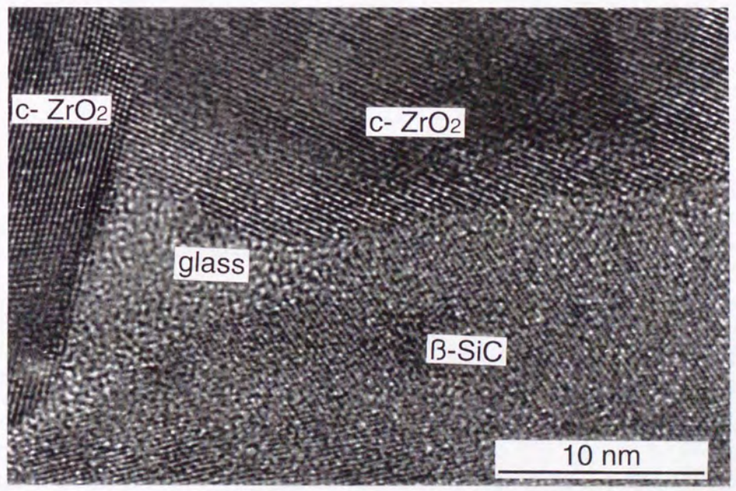

Fig. 2-8 HRTEM image of 8YSZ/5 vol% SiC nanocomposite sintered at 1700℃.

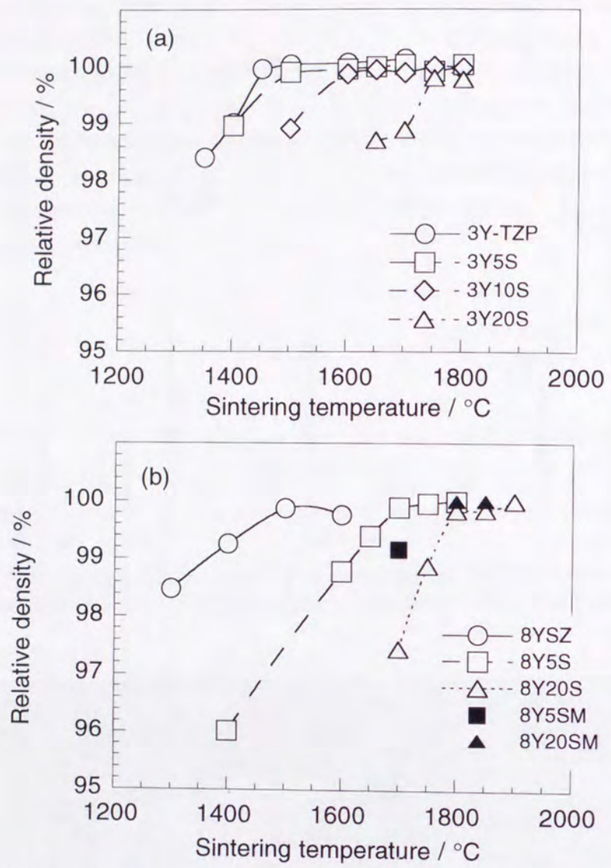

Fig. 2-9 The variations of relative density with sintering temperature for (a) 3Y-TZP monolith and 3Y-TZP/SiC nanocomposites and (b) 8YSZ monolith and 8YSZ/SiC nano- and micro composites.

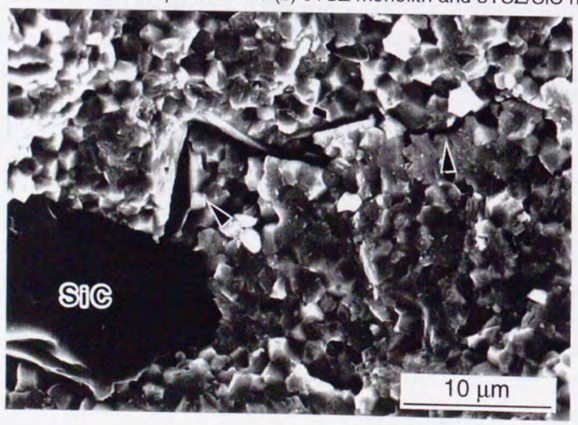

Fig. 2-10 SEM image of microcrack for 3Y-TZP/20 vol% SiC with 30 μm in particle size microcomposite sintered at 1750℃.

2.4.3 Microstructure

2.4.3.1 3Y-TZP/SiC Composites

Fig. 2-11(a) shows the variation of mean matrix grain size with the sintering temperature for 3Y-TZP monolith, 3Y5S, 3Y10S and 3Y20S, and mean grain size for 3Y5SM and 3Y20SM is shown in Table 2-2. For nanocomposite system, grain growth of 3Y-TZP matrix was suppressed by fine SiC particles, and the grain growth became smaller with increase amount of SiC content.

The grain size distributions for 3Y-TZP monolith, 3Y5S, 3Y20S and 3Y5*4.0SM sintered at 1700°C are shown in Fig. 2-12. The 3Y-TZP monolith had exaggerate grain with about 4.1 μm in grain size, while the maximum grain size for the 3Y5S, the 3Y5*4.0SM and 3Y20S were 2.5 μm, 3.4 μm and 1.9 μm, respectively. Nano-sized SiC dispersion inhibited not only normal grain growth but also abnormal grain growth. For nanocomposites, more amount of SiC dispersion strongly suppressed grain growth of matrix, thus the 3Y20S had narrower grain size distribution than the 3Y5S. Nanocomposite systems had fine and homogeneous microstructure, however, dispersing coarse SiC with several micron in particle size can not inhibit normal grain growth but abnormal grain growth in this system.

Fig. 2-13 (a) shows a TEM image of the 3Y5S sintered at 1700°C. The TEM image indicates that SiC particulate was homogeneously dispersed within the 3Y-TZP matrix grains and/or at the grain boundaries. The SiC particles with sub-micron size were mainly located at the grain boundaries, while the finer ones were within the matrix grains. The dislocation can be observed around intragranular SiC due to relaxation of the stress caused by CTE mismatch[26].

Table 2-2 The mean grain size for 3Y-TZP/5 vol% SiC and 20 vol% SiC nano- and microcomposites.

SiC particle size	5 vol% SiC / μm*1	20 vol% SiC / μm*2
0.15 μm (Nano)	1.08	0.75
1.2 μm	1.24	1.30
4.0 μm	1.31	1.91
30 μm	1.34	2.43

*1: Sintering temperature was 1700℃.
*2: Sintering temperature was 1750℃.

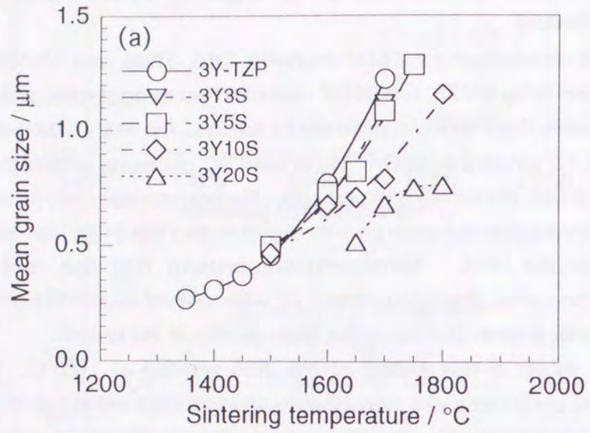

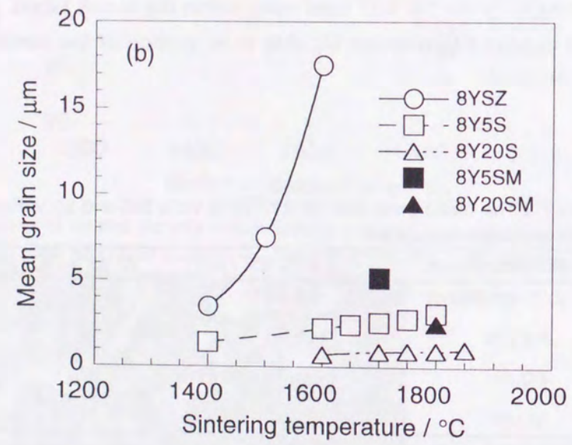

Fig. 2-11 The mean grain size as a function of sintering temperature for (a) 3Y-TZP monolith and 3Y-TZP/SiC nanocomposites and (b) 8YSZ monolith and 8YSZ/SiC nano- and micro composites.

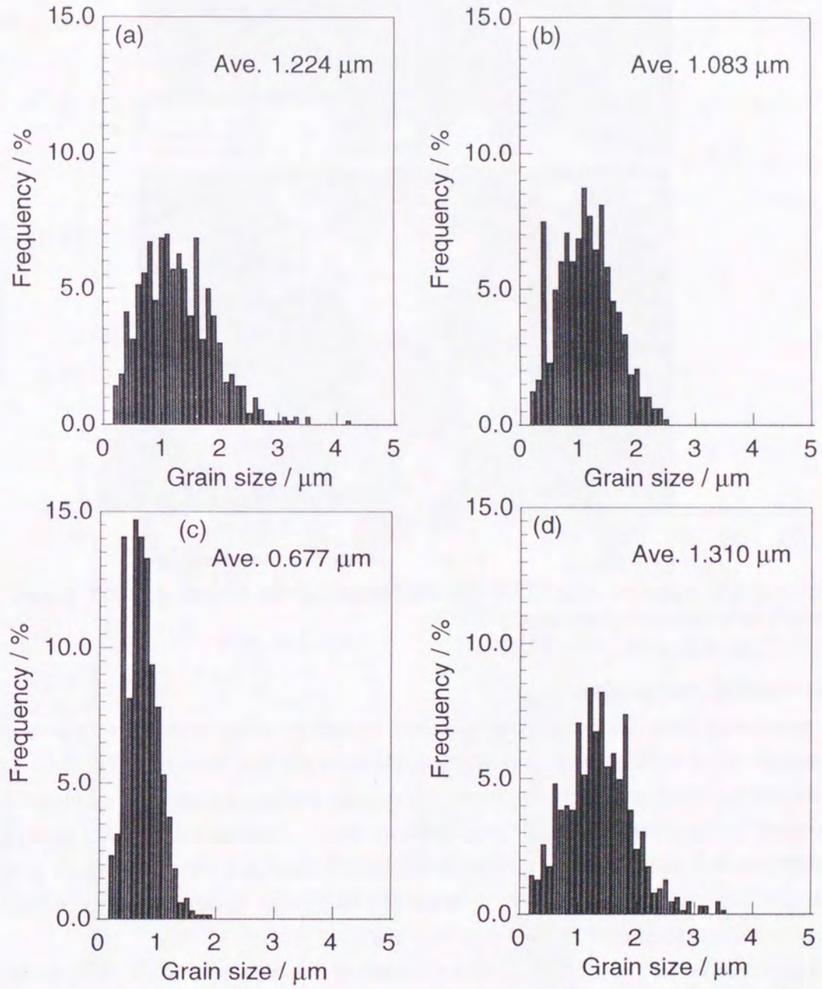

Fig. 2-12 The grain size distribution for (a) 3Y-TZP monolith, (b) 3Y-TZP/5 vol% SiC nanocomposites, (c) 3Y-TZP/20 vol% SiC nanocomposites and (d) 3Y-TZP/5 vol% SiC with 4 μm microcomposite sintered at 1700℃.

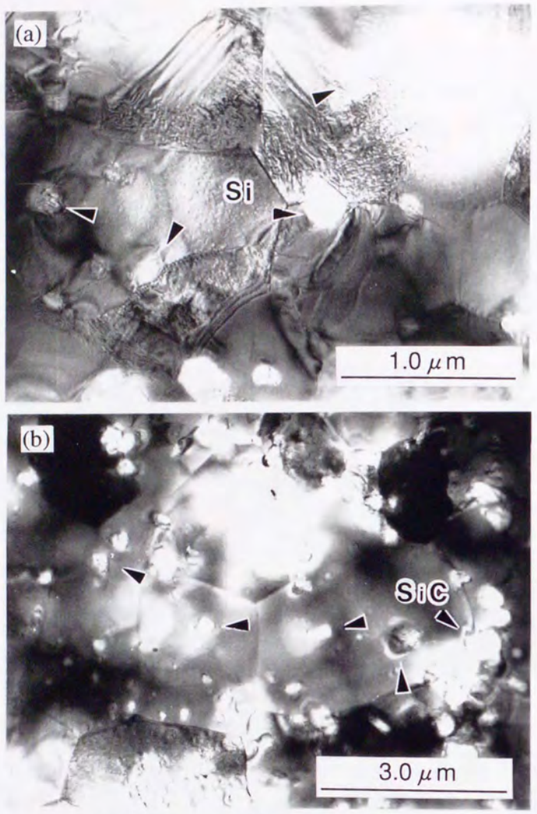

Fig. 2-13 TEM images for (a) 3Y-TZP/5 vol% SiC nanocomposite sintered at 1700℃ and (b) 8YSZ/5 vol% SiC nanocomposite at 1700℃.

2.4.3.2 8YSZ/SiC Composites

The variations of the mean matrix grain size as a function of the sintering temperature for 8YSZ monolith, 8Y5S, 8Y20S 8Y5SM and 8Y20SM are shown in Fig. 2-11 (b). The grain size of 8YSZ monolith became larger and grain growth rapidly progressed with increasing sintering temperature, compared with 3Y-TZP monolith as shown in Section 2.4.3.1. For composite case, grain size was quite small, and thus SiC addition remarkably depressed grain growth. For example, the grain size of monolith sintered at 1600°C was about 23 μm and that of the 5 vol% SiC nanocomposite at 1600°C was only 2 μm.

Grain size distributions for 8YSZ monolith sintered at 1400°C (8YSZ1400), 8Y5S at 1800°C (8Y5S1800), 8Y20S at 1800°C (8Y20S1800) and 8Y20SM at 1800°C (8Y20SM1800) are shown in Fig. 2-14. 8YSZ1400 displayed the wide grain size distribution from 1 μm to 25 μm, while nanocomposite systems had narrower distribution even though sintering temperature was higher than the monolith. The maximum grain size for 8Y5S sintered at 1800°C was below 10 μm. The grain growth was more suppressed with increase SiC content, and thus grain

size of 8Y20S sintered at 1800°C was under 3 μm. Nanocomposite systems possessed narrow and homogeneous grain size distribution by dispersing fine SiC particle. On the other hand, micro-sized SiC dispersion also inhibited not only matrix grain growth but also abnormal grain growth, therefore the mean grain size for 8Y20SM1800 was 2.6 μm and maximum grain size was below 15 μm. The inhibition effect became small with increasing particle size dispersed.

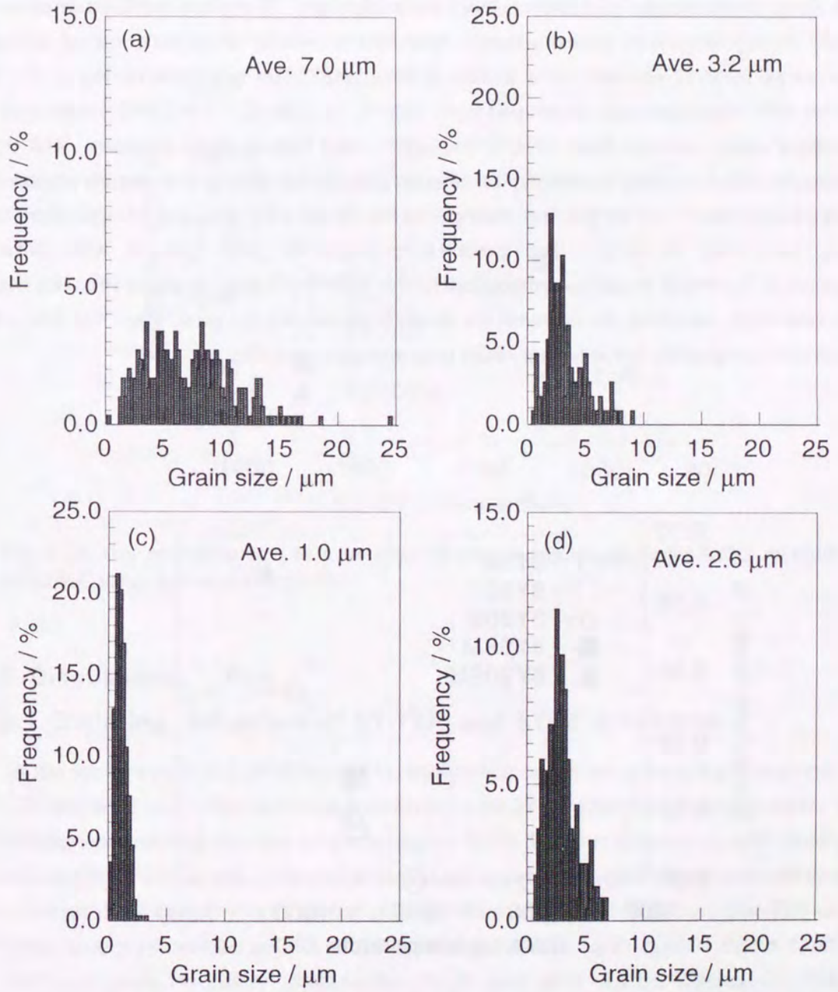

Fig. 2-14 The grain size distribution for (a) 8YSZ monolith sintered at 1400℃, (b) 8YSZ/5 vol% SiC nanocomposites at 1800℃, (c) 8YSZ/20 vol% SiC at 1800℃ and (d) 8YSZ/20 vol% SiC with 1.2 μm microcomposite at 1800℃.

Fig. 2-13 (b) is TEM image of the 8Y5S1700. SiC particulate was well dispersed in the 8YSZ matrix grain and at the grain boundary. Nano-sized SiC particles were located in the matrix and coarser ones at grain boundary.

2.4.4 Nonuniform Lattice Strain for 8YSZ/SiC Composites

For 3Y-TZP, stresses should be relaxed by the transformation to monoclinic phase, thus exact nonuniform stresses and strain cannot be evaluated. Therefore nonuniform strain for 8YSZ/SiC composites was investigated. Nonuniform strains as a function of sintering temperature for 8YSZ monolith, 8Y5S, 8Y5SM, 8Y20S and 8Y20SM are shown in Fig. 2-15. The strain for 8Y5S monotonously increased from 1600°C to 1800°C. For 8Y20S, there was an immediate sharp increase from 1750°C to 1800°C and then a slight increase. This sharp increase should be related to density, the stresses can not be arise at low density region and should be released. For 8Y20S, the change of the strain with sintering temperature was smaller than that for 8Y5S. The great suppression of grain growth with sintering temperature for 8Y20S should be attributed to the difference in increase of strain between 8Y20S and 8Y5S, because the nonuniform strain is influenced by grain size. On the other hand, microcomposites have higher strain than nanocomposites.

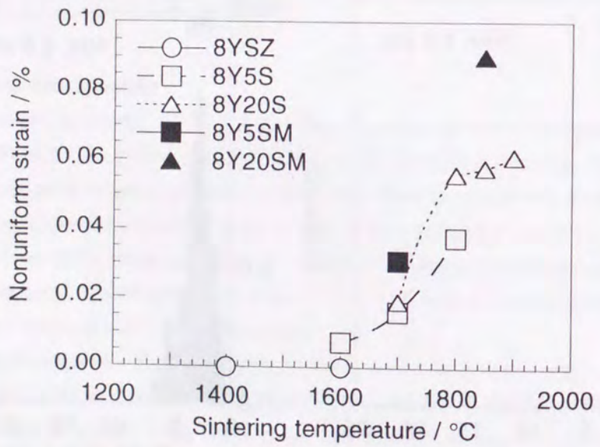

Fig. 2-15 The nonuniform lattice strain measured by X-ray diffraction analysis as a function of sintering temperature for 8YSZ monolith and 8YSZ/SiC nano- and microcomposites.

Crystalline size measured by XRD as function of sintering temperature for 8YSZ monolith, 8Y5S, 8Y5SM, 8Y20S and 8Y20SM is shown in Fig. 2-16. Crystalline size became smaller with increasing SiC content and decreasing SiC particle size as well as the mean grain size. For 8YSZ monolith and 8Y5S, crystalline size increased with increase sintering temperature, while the crystal size for 8Y20S decreased after slightly increase. The decrease in crystalline size might be due to formation of sub-grain boundary by the relaxation of the thermoelastic stresses.

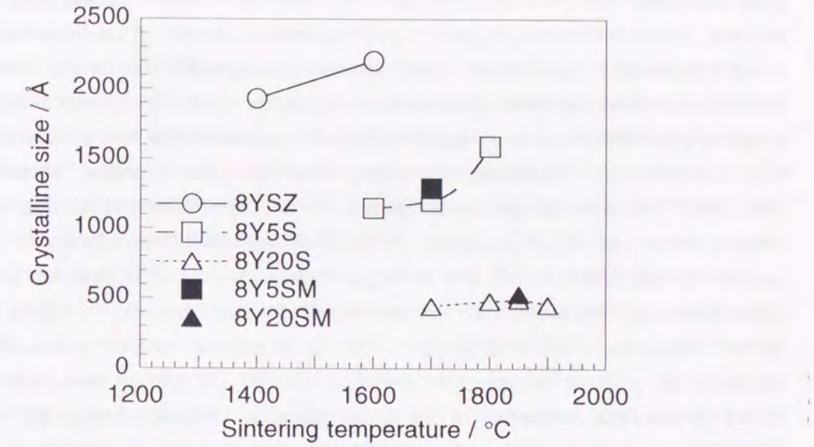

Fig. 2-16 The crystalline size as a function of sintering temperature for 8YSZ monolith and 8YSZ/SiC nano- and microcomposites.

2.5 Discussions

2.5.1 Sintering Behaviors of 3Y-TZP and 8YSZ Monoliths

In this section, from the differences of densification and grain growth behaviors between 3Y-TZP and 8YSZ monoliths, sintering mechanisms for 3Y-TZP and 8YSZ are discussed. In the final stage of sintering process which is above 90-95 % in the relative density, mainly two mechanisms could be important as a mater transport path: *grain boundary diffusion* from sources on the boundary and *lattice diffusion* from sources on the boundary[31] and the sintering rate is influenced by the diffusivity of cations, such as Y^{3+} and Zr^{4+} in the Y-ZrO_2 case.

First, the grain boundary diffusion for 3Y-TZP and 8YSZ will be discussed. From the densification behaviors for both 3Y-TZP and 8YSZ monoliths, the both were fully densified at 1400 to 1450°C, and the both densification were progressed with almost similar rate as

shown in Figs. 2-9 (a) and (b). However, the difference was observed at sintering temperature of 1600°C, the density for 8YSZ monolith decreased due to the overfiring. The overfiring is contributed to the secondary recrystallization (abnormal grain growth) occurring at higher temperatures before the elimination of pores, which indicates the grain boundary mobility is quite higher than pore mobility[29]. That is, the grain boundary mobility for 8YSZ should be high, which strongly influences not only on densification but also on the grain growth. For the grain size as shown in Fig. 2-11, remarkable difference was observed in both monoliths. The grain growth for 8YSZ monolith rapidly progressed, different from 3Y-TZP monolith. This is due to high grain boundary mobility for 8YSZ. The grain boundary mobility is proportional to its curvature which is related to grain size and to the rate at which atoms can jump across the grain boundary. Thus the effect of curvature which is inversely proportional to grain size should be small in this system, because particle size of each starting powder is almost same. On the other hand, the activation energy for jumping across the boundary should correspond approximately to the activation energy for boundary diffusion. Therefore, 8YSZ should have high grain boundary diffusivity compared with 3Y-TZP because of rapid grain growth for 8YSZ monolith and no degradation in the relative density for 3Y-TZP monolith. It has been reported that activation energy of grain growth is 105 kcal/mol for the tetragonal ZrO_2 and 69 kcal/mol for the cubic ZrO_2, respectively[32], therefore, it makes sure that 8YSZ has higher grain boundary diffusivity than 3Y-TZP. From these results and discussions, grain growth for 8YSZ proceeds much more quickly even at lower temperature because of its low activation energy[33].

This remarkable difference of the grain boundary diffusivity between both monoliths appears to depend on the content and the distribution of Y_2O_3 as a stabilizer. In 3Y-TZP and 8YSZ cases, doped Y_2O_3 into ZrO_2 generates oxygen vacancy, and oxygen vacancy increases with increasing Y_2O_3. Therefore, 8YSZ should have high grain boundary diffusivity, because the defects enhance the diffusion. Furthermore, Y_2O_3 segregation can be considered as a factor which depresses the grain boundary diffusivity/mobility for 3Y-TZP. It has been reported that Y_2O_3 (Y^{3+}) is prone to segregate in the grain boundary for 3Y-TZP[32], therefore the gradient of Y_2O_3 concentration exists in a 3Y-TZP grain and concentration increase from the center to the grain boundary. The concentration gradient, however, decreases with increasing Y_2O_3 content, therefore enrichment of Y_2O_3 cannot be observed in cubic ZrO_2 grains[32]. The segregated Y_2O_3 appears to depress the grain boundary mobility of 3Y-TZP, which is similar to the tendency reported that grain boundary mobility was depressed when small amounts of soluble impurity were added to high purity metals by a number of researchers[34,35]. This is the impurity drag force, in which the impurities are dragged along by the grain boundary. By adding the impurity drag force, the force needed to keep a boundary moving with that velocity in the pure material and velocity-driving force is related to the composition and temperature. While the impurity drag force

does not act in cubic ZrO_2 (c-ZrO_2) grains in 8YSZ, because Y_2O_3 is not impurity in homogeneous composition such as c-ZrO_2. Therefore the grain boundary diffusivity/mobility for 8YSZ is higher than that for 3Y-TZP.

Second, the difference of lattice diffusivity between 3Y-TZP and 8YSZ will be discussed. From densification behavior for 3Y-TZP and 8YSZ monoliths, it is suggested that the lattice diffusivity for 3Y-TZP is higher than that for 8YSZ, because the both sintering behaviors below 1600°C were similar in spite of the higher grain boundary diffusivity for 8YSZ. This is due to the concentration gradient of Y^{3+} as mentioned above. Tetragonal ZrO_2 (t-ZrO_2) composed of 3Y-TZP is metastable phase at lower temperatures. ZrO_2 tends to discharge Y_2O_3 at the region where monoclinic ZrO_2 (m-ZrO_2) is stable during sintering, both heating and cooling processes. t-ZrO_2 transforms to m-ZrO_2 which is stable phase at room temperature and has low Y_2O_3 content, therefore 3Y-TZP has high chemical potential in 3Y-TZP grain which has the concentration gradient of Y^{3+}. The chemical potential should enhance the lattice diffusion in 3Y-TZP. Comparing with 8YSZ, however, 3Y-TZP should have high lattice diffusivity due to the chemical potential effect, even though oxygen vacancy for 3Y-TZP is less than 8YSZ. On the other hand, c-ZrO_2 is more stable than t-ZrO_2; c-ZrO_2 does not transform to t-ZrO_2 or m-ZrO_2. Thus 8 mol% Y_2O_3 forms homogeneous solid solution with ZrO_2 at any temperatures. Therefore 8YSZ has lower lattice diffusivity than 3Y-TZP due to its low chemical potential.

Consequently, 3Y-TZP has higher lattice diffusivity which should be dominant mechanism for densification and lower grain boundary diffusivity compared with 8YSZ, thus densification without grain growth would be possible and sintered body had fine grains. On the other hand, 8YSZ has high a grain boundary diffusivity and mobility promote of grain growth would occur during densification. The differences in lattice and grain boundary diffusivities between 3Y-TZP and 8YSZ generate the different sintering behaviors between 3Y-TZP and 8YSZ.

2.5.2 Effects of SiC Dispersion on Microstructure

SiC particles obviously inhibited both densification and grain growth as shown in Figs. 2-9 and 2-11. First, SiC effect on densification is focused on in this section. The inhibition in densification is due to the increase of the interface area between ZrO_2 and SiC particle, in which the surface diffusion of matrix ions around second phase inclusion is limited due to difference in diffusion rate. Thus the diffusion was suppressed[27,36], and the densification is further inhibited with increasing SiC content because of the increase of the interface with low diffusivity. Furthermore, since SiC addition makes microstructure to be fine, the grain boundary diffusion path becomes longer in proportion to the diameter of the SiC particulate. Thus the grain boundary diffusivity strongly was decreased by adding second phase.

For SiC added ZrO_2 composites, on the other hand, the lattice diffusion was not so

effective on densification and grain growth for whole sintering schedule, compared with grain boundary diffusion. From Fig. 2-9, higher sintering temperature was necessary to densify 8YSZ/SiC nanocomposites compared with 3Y-TZP/SiC nanocomposites, that is, densification for 8YSZ was more depressed. This is related to the difference of densification mechanism between 3Y-TZP and 8YSZ. Densification and grain growth for 8YSZ was remarkably inhibited due to the depression of its grain boundary diffusion. While SiC particulate does not do influence on not only densification but also grain growth for 3Y-TZP because of its dominant mechanism, i.e., lattice diffusion. As mentioned above section, dominant densification mechanisms for 3Y-TZP and 8YSZ were supposed lattice and grain boundary diffusion, respectively. Therefore, SiC addition should have larger effect on 8YSZ than on 3Y-TZP.

In addition to the increase in the interface with low diffusivity, pinning effect of SiC particles can be considered as a factor which suppresses densification and grain growth. SiC particles pin the grain boundary movement, that is, grain boundary movement as a dominant mechanism for grain growth should be depressed. The dispersed particles, in general, inhibit grain boundary migration of the matrix [27,36,37,38,39]. It is evident from SEM images in Fig. 2-17 that grain boundary migration was inhibited by SiC particles. Grain boundaries for composites were distorted, compared to the quite straight boundaries of the ZrO_2 monolith. From these SEM images, it was confirmed that the SiC particles with sub-micron size were located mainly at the grain boundaries, while the finer ones were trapped within the matrix grains. Dispersed SiC particles modified matrix microstructure obviously, and the observed morphologies could be explained as follows. For the finer SiC particles, the matrix grain boundary can easily pass through the SiC particles, which are captured into the matrix grains. On the contrary, the large SiC particles remain at the grain boundaries without being incorporated into the matrix grain, because the grain boundary cannot pass through the larger SiC particulate. Thus, in microcomposite case, almost SiC particles located at grain boundary. This behavior is attributed to the interaction between the pinning force by one particle and the driving force for grain boundary migration [2739]. Fig. 2-18 is a schematic illustration for pinning of grain boundary by second phase particle with r in radius, in which γ_{ss} is surface tension and θ the angle between the particle and grain boundary. The pinning force, f, is expressed as following equation [40],

$$f = \pi r \gamma_{ss} \sin 2\theta \qquad (2\text{-}5)$$

The pinning force becomes maximum value at $\theta = 45°$, and then $f = \pi r \gamma_{ss}$. Thus the pinning force for a particle becomes with increasing of particle radius, however, total pinning force depends on not only particle radius, but also the number of particles. Total pinning effect, F, is expressed by Eq. (2-6),

$$F = n_s \pi \bar{r} \gamma_{ss} \qquad (2\text{-}6)$$

where n_s and $\bar{r}$ is the number of particles per unit area and mean particle radius, respectively. For example, in the case that micro-sized SiC, $2\bar{r}_{micro}$ is 1.2 μm and nano-sized SiC, $2\bar{r}_{nano}$, is 150 nm, $\bar{r}_{micro}/\bar{r}_{nano}$, is about 8, while n_{snano}/n_{smicro} is about 500. Thus, nanocomposite should have higher pinning force than microcomposites. From these results, the number of the second phase particulate strongly influences on pinning force, thus ZrO_2 incorporating finer SiC particles demonstrated fine microstructure.

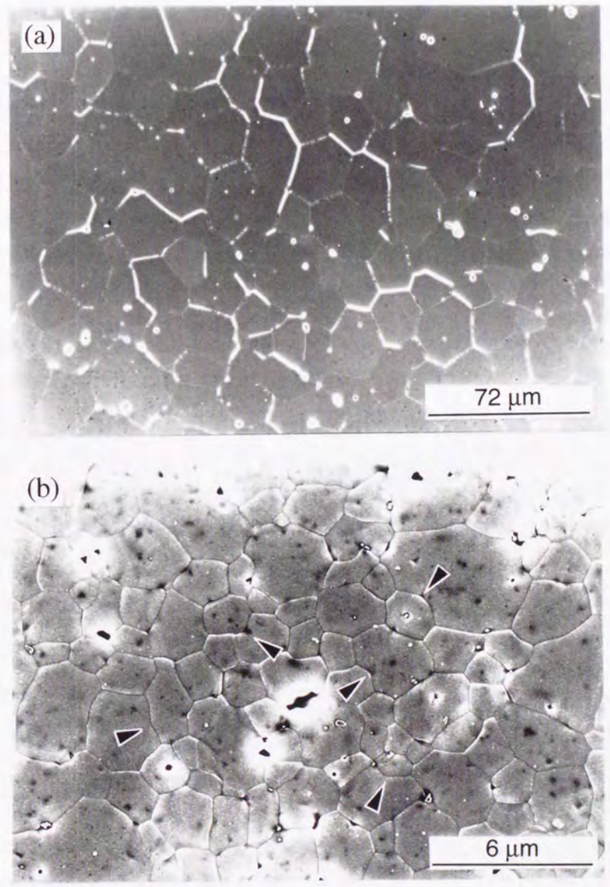

Fig. 2-17 SEM image of grain boundary distortion for (a) 8YSZ monolith sintered at 1400℃ and (b) 8YSZ/5 vol% SiC nanocomposite at 1700℃.

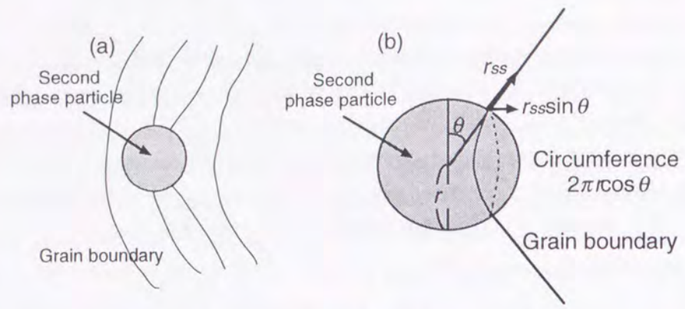

Fig.2-18 Schematic illustration of pinning effect.

The dependence of the grain size and content of second phase on the matrix grain size can be explained by using Zener's equation, Eq. (2-7), which suggests a relationship between grain size of matrix and volume fraction and particle size of the second phase[41].

$$\overline{G} = k\frac{r_p}{f_p} \qquad (2\text{-}7)$$

where $\overline{G}$, k, r_p and f_p are mean grain size for matrix, constant, radius and volume fraction of second phase particle, respectively. Eq. (2-7) clearly suggests that mean grain size ($\overline{G}$) decreases with decreasing SiC size and increasing volume fraction (f_p) of SiC.

SiC dispersion strongly influences on grain boundary diffusion due to the increase of the interface with low diffusivity and the pinning effect. It resulted in that densification and grain growth for 8YSZ , in which grain boundary diffusion and movement are fast, were more inhibited than 3Y-TZP. Thus 8YSZ incorporating finer SiC particles has fine and homogeneous microstructure compared with monolith.

However, For 3Y-TZP/SiC microcomposites which has lower pinning force than nanocomposites, too large SiC particulate has no effect on inhibition of grain growth. Grain size of matrix for microcomposites became larger than monolith, and become large with increasing SiC content. This is due to impurities in starting powders. In general, abnormal grain growth is enhanced by impurity[42]. Furthermore, according to Hillert[43], abnormal grain growth tends to occur, when size of dispersed particles is too large.

2.5.3 Stresses and Strains

As mentioned in section 2.2, the residual stress is classified into uniform and nonuniform stresses. First, uniform stresses and strains will be focused on theoretically. When all over

the polycrystalline is imposed the residual stress which depends on CTE mismatch, the lattice for 8YSZ left in a state of uniform tension.

The theoretical stresses depend on volume content of second phase, CTE and difference of temperature, ΔT, but do not depend on particle size of second phase. However, the uniform stress by CTE mismatch actually depends on the location whether SiC particles locate within matrix grains or at grain boundaries, as mentioned in section 2.2. Distribution of SiC particles is determined from the balance between the pinning force which is varied by second phase particle size and driving force of grain boundary movement which is related to surface tension and grain size of matrix. That is, the difference of particle size for second phase generates the difference of uniform stress and strain. In addition, fabrication temperature should also influence the distribution, because high temperature makes grain large, in which lots of second phases are incorporated within matrix grains. Assuming that all SiC particles locate at grain boundary or within matrix grains, and relaxations by lattice and grain boundary diffusion creep do not occur below at 1400°C and 1000°C, the uniform stress calculated by using Eqs. 2-1, 2-2 and 2-3 is shown in Table 2-3. The CTEs of SiC and ZrO_2 (3Y-TZP and 8YSZ) are 4.45 x 10^{-6} / K [44] and 10 x 10^{-6} / K (CTE of 3Y-TZP (10.6 x 10^{-6} K) [45] is similar to that of 8YSZ (10 x 10^{-6} K) [46]), respectively. The tensile stress on matrix increases with increasing the second phase content, while the high compressive stress on SiC particles decreases. The decrease in the compressive stress around SiC particles is due to cancellation by interference of stress field around each particles.

Uniform stress and strain

In this work, uniform stresses cannot be measured by XRD analysis, because peak of SiC can not distinguish from ZrO_2 peak at high 2θ angle; atomic scattering factor of ZrO_2 is much larger than that of SiC, and some of SiC peaks are overlapped ZrO_2 peaks. Thus, uniform stresses and strains are restrict within theoretical analysis. Many researchers[26,47] have been confirmed that theoretical value for matrix and large second phase particles or whisker are almost satisfied with experimental results, however, the compressive stress on nano-sized particulate measured by XRD is smaller than theoretical value in nano-sized SiC dispersed composites. This is due to relaxation by the formation of dislocation around nano-sized particles. In the present work, the temperatures at which the relaxation of the grain boundary diffusion creep and lattice diffusion creep stop are assumed to be 1000°C and 1400°C. The actual uniform stresses developed in nanocomposite may be smaller than the calculation values, because some of SiC particles existed at grain boundary as shown in Fig. 2-13. Both for micro- and nanocomposites, the tensile stress on matrix increases with increasing in the amount of SiC particles in matrix grains and the compressive stress SiC particles decrease with increasing SiC particulate. Thus, nanocomposites incorporating a lot of SiC particles in matrix grains have higher tensile stress and strain than

microcomposites, and the compressive stresses and strain become larger than microcomposites. For the tensile stress on matrix, ZrO_2 lattice should be expanded by the stress as illustrated in Fig. 2-1 (b).

Nonuniform stress and strain

On the other hand, nonuniform strain for 8YSZ matrix in 8YSZ/SiC composites was measured and the results are shown in Fig. 2-15. The uniform strain on matrix estimated from uniform stress in Table 2-3 is shown in Table 2-4 in order to compare with nonuniform strain. On the contrary to uniform strain, microcomposites, 8Y5SM and 8Y20SM, exhibit higher nonuniform strain than nanocomposites, 8Y5S and 8Y20S. For monolithic ZrO_2, nonuniform strain can be generated by the geometry, the difference in crystal face between each other and crystal anisotropy. When second phase exists, the CTE and Young's modulus mismatches should enhance to the nonuniform strains. Since 8YSZ monolith has cubic structure without crystal anisotropy, nonuniform strain is not imposed on the matrix. While, the nonuniform strain for composites is imposed by effects of some mismatches between matrix and second phase. Nonuniform stresses generate at grain boundaries, which is determined by the relationship between neighbors and the spacing of lattice planes depends on position in a grain. When SiC particles located at grain boundaries, the stress at grain boundary must enhance. Thus microcomposites demonstrated higher strain than nanocomposites. Some spacing of lattice planes should be more expanded than uniform strain when the nonuniform strain exists, however some of the spacing should be shrunk and narrow. When nonuniform stress become large, microcracks will be generated in order to relax the stress. Microcrack was observed in 3Y20*30SM should be attributed to the uniform and nonuniform stresses. The stresses enhanced transformation from tetragonal to monoclinic accompanied volume expansion, and then microcrack should be generated.

The difference in the lattice spacing affects ionic conductivity as will be discussed in Chapter 5, and the stresses influence their properties.

Table 2-3 Theoretical uniform stresses for ZrO_2 and SiC.

	ZrO_2 / MPa		SiC / MPa	
	Lattice*1	Grain boundary*2	Lattice*1	Grain boundary*2
8Y5S	90	63	1678	1199
8Y20S	350	250	1413	1009

*1 : The relaxation by lattice diffusion creep stops at 1400℃.
*2 : That the relaxation by lattice and grain boundary diffusion creep stops at 1000℃.

Table 2-4 Theoretical uniform strains calculated from uniform stresses in Table 2-3.

	Lattice (Nano)	Grain boundary (Micro)
8YSZ monolith	0	0
8Y5S	3.9×10^{-4}	2.8×10^{-4}
8Y20S	14.1×10^{-4}	10.0×10^{-4}

2.6 Conclusions

3Y-TZP/SiC and 8YSZ/SiC nano- and microcomposites were fabricated by hot-pressing technique, and effects of SiC particulate on densification, grain growth and residual stresses and strains were investigated. In addition, the difference of densification and grain growth between 3Y-TZP and 8YSZ were also investigated. The following results were obtained.

Dominant mechanism of densification and grain growth for 3Y-TZP and 8YSZ are different. For 3Y-TZP, lattice diffusion should be the dominant mechanism, while for 8YSZ grain boundary diffusion and movement. Therefore densification for 3Y-TZP progressed without grain growth, and enhancing grain growth occurs with densification for 8YSZ. The difference in lattice and grain boundary diffusivities between 3Y-TZP and 8YSZ monoliths generate the difference in their densification and grain growth behaviors, which influence the effects of SiC particulate.

SiC dispersion strongly influenced on grain boundary diffusion due to the increase of the interface between matrix and second phase which had lower diffusivity than the grain boundary between matrix and matrix and the pinning effect. Therefore the densification and grain growth for 8YSZ, in which grain boundary diffusion and movement were fast, were strongly inhibited. Thus 8YSZ incorporating finer SiC particles had finer and more homogeneous microstructure compared with monolith. For 3Y-TZP, which had fine microstructure, the effects of second phase dispersion on densification and grain growth was small, compared with 8YSZ case.

Dispersing SiC particulate generated the residual stresses and strains, which increased with increasing second phase content. The second phase content in matrix grain enhanced uniform stress and strain, while particles at grain boundary nonuniform stress and strain. Therefore, nanocomposites have higher uniform stress and strain than microcomposites, and thus the lattice spacing for nanocomposites should be more expanded.

The microstructure and the residual stresses discussed in this chapter will be related to the mechanical and electrical properties for both 3Y-TZP/SiC and 8YSZ/SiC composites in Chapters 3 and 5.

References

1 T. Masaki, Mechanical properties of toughened ZrO_2-Y_2O_3 ceramics, J. Am. Ceram. Soc., 69 [8](1986) 638-40.
2 T. Masaki, K. Nakajima and K. Shinjo, High temperature mechanical properties of Y-PSZ HIPed under an oxygen-containing atmosphere, J. Mater. Sci. Lett., 5 (1986) 1115-1118.
3 M. Hirano, H. Inada, Fracture toughness, strength and Vickers hardness of yttria-ceria-doped tetragonal zirconia/alumina composites fabricated by hot isostatic pressing, J. Mater. Sci., 27 (1992) 3511-3518.
4 F. Meschke, G. D. Portu and N. Claussen, Microstructure and thermal stability of fine-grained (Y, Mg)-PSZ ceramics with alumina additions, J. Eur. Ceram. Soc., 11 (1993) 481-486.
5 N. Claussen, K. -L. Weisskopf and M Rühle, Tetragonal zirconia polycrystals reinforced with SiC whiskers, J. Am. Ceram. Soc., 69 [3](1986) 288-92.
6 J. Hong, L. Gao, B. A. Show and D. P. Thompson, SiC platelet and SiC platelet-alumina reinforced TZP matrix composites, Br. Ceram. Transactions, 94 [5](1995) 201-204.
7 S. E. Dougherty, T. G. Nieh, J. Wadsworth and Y. Akimune, Mechanical properties of a 20 vol% SiC whisker-reinforced, yttria-stabilized, tetragonal zirconia composite at elevated temperature, J. Mater. Res., 10 [1](1995) 113-118.
8 H. L. Lee and K. M. Lee, Effect of SiC on the mechanical properties of 3Y-TZP/SiC composites, J. Mater. Sci. Lett., 13 (1994) 974-976.
9 S. Terauchi, H. Takizawa, T. Endo and M. Shimada, Ionic conductivity and mechanical properties of post-HIPed cubic zirconia/alumina composites, Materials and Manufacturing Processes, 9 [5](1994) 965-974.
10 L. M. Navarro, P. Recio, P. Duran, Preparation and properties evaluation of zirconia-based Al_2O_3 composites as electrolytes for solid oxide fuel cell systems, J. Mater. Sci., 30 (1995) 1931-1960.
11 K. Oe, K. Kikkawa, A. Kishimoto, Y. Nakamura and H. Yanagida, Toughening of ionic conductive zirconia ceramics utilizing a nonlinear effect, Solid State Ionics, 91 (1996) 131-136.
12 Y. Saito, Electrical conduction of stabilized zirconia and oxygen sensor. In Zirconia Ceramics 1, Ed. by. S. Somiya, Uchida Rokakuho, Tokyo, 1983, pp. 109-125.
13 J. F. Baumard, B. Cales and A. M. Anthony, Stabilized zirconia : basic science and applications. in Zirconia Ceramics 1, Ed. by S. Somiya, Uchida Rokakuho, Tokyo, 1983, pp. 127-144.
14 M. Takeuchi, O_2 sensor. Bull. Ceram. Soc. Jpn., 17 [6](1982) 433-438.
15 K. Niihara, New design concept of structural ceramics-ceramic nanocomposites. J. Ceram. Soc. Jpn., 99 [10](1991) 974-982.
16 M. Sternitzke, Structural Ceramic Nanocomposites, J. Eur. Ceram. Soc., 17 (1997) 1061-1082.
17 Z. Li and R. C. Bradt, Micromechanical stress in SiC-reinforced Al_2O_3 composites, J. Am. Ceram. Soc., 72 [1](1989) 70-77.
18 M. Taya, S. Hayashi, A. S. Kobayashi and H. S. Yoon, Toughening of a particulate-reinforced ceramic-matrix composites by thermal residual stress, J. Am. Ceram. Soc., 73 [5](1382-1391) 1382-1391.
19 W. Kreher and R. Janssen, On microstructural residual stresses in particle reinforced ceramics, J. Eur. Ceram. Soc., 10 (1992) 167-173.
20 Cullity, Elements of x-ray diffraction, 2nd Ed., Addison-Wesley Publishing Company, Inc., Massachusetts, USA, 1977, pp. 285-286.
21 J. B. Cohen, H. Dolle and M. R. James, in Accuracy in Powder Diffraction, NBS Special Publication No. 567. U.S., 1980, pp. 453-477.
22 I. C. Noyan and J. B. Cohen, Residual stress, Measurement by diffraction and interpretation, Springer-Verleg, N.Y., 1987, pp. 117-162.
23 W. Ruland, Acta Crystallogr., 18 (1965) 581.
24 F. R. L. Schoening, Acta Crystallogr., 18 (1965) 975.
25 N. C. Halder and N. J. Wanger, Acta Crystallogr., 20 (1965) 312.
26 Y. H. Choa, Ph. D. thesis, Osaka University, 1996.
27 A. Nakahira and K. Niihara, Sintering behaviors and consolidation process for Al_2O_3/SiC

nanocomposites, J. Ceram. Soc. Jpn., 100 [4](1992) 448-453.
28 T. Ohji, A. Nakahira, T. Hirano and K. Niihara, Tensile creep behavior of alumina/silicon carbide nanocomposite, J. Am. Ceram, Soc., 77 [12](1994) 3259-3262.
29 W. D. Kingery, H. K. Bowen and D. R. Uhlmann, Introduction to Ceramics, 2nd Ed., JOHN WILEY&SONS, NY, 1976, p507.
30 S. T. Kwon, D. Y. Kim, T. K. Kang and D. N. Yoon, Effect of sintering temperature on the densification of Al_2O_3. J. Am. Ceram. Soc., 70 [4](1987) C69-C70.
31 W., D. Kingery, H. K. Bowen and D. R. Uhlmann, Introduction to Ceramics, 2nd Ed., JOHN WILEY & SONS, NY, 1976, p481.
32 I. G. Lee and I. W. Chen, Sintering and grain growth in tetragonal and cubic zirconia, in Sintering '87, Eds. by S. Somiya, S. Shimada, M. Yoshimura and R. Watanabe, Elsevier, Amsterdam, The Netherlands, 1988, pp. 340-45.
33 S. A. Nightingale, H. K. Worner and D. P. Dunne, Microstructural development during the microwave sintering of yttria-zirconia ceramics, J. Am. Ceram. Soc., 80 [2](1997) 394-400.
34 J. W. Cahn, The impurity-drag effect in grain boundary motion, Acta Met., 10 (1962) 789-798.
35 K. Lücke and H. P. Stüwe, On the theory of impurity controlled grain boundary motion, Acta Met., 19 (1971) 1087-1099.
36 S. Hori, R. Kurita, M. Yoshimura and S. Somiya, Suppressed grain growth in final-stage sintering of Al_2O_3 with dispersed ZrO_2 particles, J. Mater. Sci. Let., 4 (1985) 1067-1070.
37 M. F. Ashby and R. M. A. Centamore, The dragging of small oxide particles by migrating grain boundaries in cupper, Acta Metall. 16 (1968) 1081-1092.
38 F. F. Lange and M. M. Hirlinger, Hindrance of grain growth in Al_2O_3 by ZrO_2 inclusions, J. Am. Ceram. Soc., 67 [3](1984) 164-168.
39 L. C. Stearns and M. P. Harmer, Particle-inhibited grain growth in Al_2O_3-SiC: I, experimental results, J. Am. Ceram. Soc., 79 [12](1996) 3013-3019.
40 N. Mizutani, Y. Ozaki, T. Kimura and T. Yamaguchi, Ceramic Processing, Ceramic Science Series, vol. 8, Eds. by T. Yamaguchi and H. Yanagida, Gihodo Shuppan, Tokyo, 1990, p. 134.
41 D. A. Porter and K. E. Easterling, Phase Transformations in Metals and Alloys, 2nd Ed., Chapman and Hall, London, 1992, pp. 139-142.
42 M. F. Yan, Microstructure control in the processing of electronic ceramics, Materials Science and Engineering, 48 (1981) 53-72.
43 M. Hillert, On the theory of normal and abnormal grain growth, Acta Metall., 13 (1965) 227-238.
44 Cyclopedia of Fine Ceramics, Eds. by H. Yanagida et al., Gihodo Press, Tokyo, 1987, p. 595.
45 D. J. Green, R. H. J. Hannink and M. V. Swain, Transformation Toughening of Ceramics, CRC Press, Inc., NW, p223.
46 Cyclopedia of Fine Ceramics, Eds. by H. Yanagida et al., Gihodo Press, Tokyo, 1987, p.228.
47 A. Abuhasan, C. Balasingh and P. Predecki, Residual stresses in alumina/silicon carbide (whisker) composites by X-ray diffraction, J. Am . Ceram. Soc., 73 [8](1990) 2474-2484.

3 Mechanical Properties of ZrO_2/SiC Composites

3.1 Introduction

In previous chapter, the effects of dispersed SiC particulate on the microstructure including the residual strains for 3Y-TZP/SiC and 8YSZ/SiC composites were investigated. Generally, the microstructure directly affects mechanical properties. Some researchers have reported nano-sized particulate dispersed composites have significant improvements in mechanical properties at both ambient and elevated temperatures[1,2,3,4,5]. For 3Y-TZP, phase transformation from tetragonal (t-ZrO_2) to monoclinic (m-ZrO_2) is an important factor affecting its fracture toughness and strength, in addition to the microstructure. On the other hand, Swain et al.[6] suggested a mechanism for the limitation of strength in transformation toughened ZrO_2, and it is difficult to improve both strength and toughness by only transformation toughening.

In this chapter, mechanical properties for 3Y-TZP/SiC and 8YSZ/SiC nano- and microcomposites were evaluated, and effects of nano- and micro-sized SiC dispersion on the properties were investigated in connection to its microstructure. Especially, for 3Y-TZP based composites, the effects of dispersoid size and content on the phase transformation were investigated, and the relationship between transformation toughening and grain size and/or the residual stresses were discussed.

3.2 Experimental Procedure

3.2.1 Specimen Preparation

3Y-TZP monolith, 3Y-TZP/3-20 vol% SiC composites, 8YSZ monolith and 8YSZ/5 and 20 vol% SiC composites were fabricated by using conventional method, and sintered bodies were machined to bar-shaped specimens as described in Chapter 2. The specimens were subjected to various evaluation as mentioned below.

3.2.2 Evaluations

Young's modulus

The specimens (3 x 4 x 36 mm) were coated by a carbon painting on one side in order to act as an electrode and then suspended on two thin tungsten wires in correspondence of the nodal points. Flexural vibrations were generated by electrostatic force and resonance frequencies were determined by using an oscilloscope. Young's modulus, E, was calculated by using the following Eq. (3-1),

$$E = 0.9465 \times \frac{M \cdot f^2}{w}\left(\frac{l}{t}\right)^3\left\{1 + 6.59\left(\frac{t}{l}\right)^2\right\} \qquad (3\text{-}1)$$

where M, w, t, l and f are the mass, the width, the thickness, the length of the specimen and the resonance frequency obtained, respectively.

Hardness

Hardness was measured by a Vickers indentation (AVK-2, Akashi Co. Ltd., Japan), and calculate by following Eq. (3-2),

$$Hv = \frac{2P\sin(\theta/2)}{d^2} \qquad (3\text{-}2)$$

where P is the applied load, d the diagonal of the indentation measured by optical microscope and θ is 136° which is the angle comprised between the two opposite faces of the pyramidal indenter. Load was applied and held constant during a period of 15 s.

Fracture strength

Fracture strength was measured by three point bending test with a span of 30 mm at a crosshead speed of 0.5 mm/min using an universal testing machine (Autograph, model AG-10TC, Shimazu Co. Ltd., Japan) based on the instructions of JIS-R 1601 in the JIS standardization. The bar-shaped specimens (3 x 4 x 36 mm) were used, whose tensile surfaces were polished with 0.5 μm diamond slurry and the edges were beveled at 45° to avoid the fracture from the edge. The strength, σ, was given by the following equation (3-3),

$$\sigma = \frac{3PL}{2bd^2} \qquad (3\text{-}3)$$

where P (kgf) is a fracture load with obtained by three point bending test, L is span of 30 mm in this case and b and d is the width and thickness of specimen, respectively.

Fracture toughness

Fracture toughness was evaluated by the Vickers indentation microfracture (IF) method using a micro Vickers diamond indenter based on the standard of JIS-R 1607. An indentation load of 196 N and 49 N was applied for 15 s on the polished surfaces of specimen at room temperature, respectively. The fracture toughness, K_{IC}, was calculated by the following equation (3-4)[7],

$$K_{IC} = 0.203(c/a)^{-3/2} a^{1/2} Hv \qquad (3\text{-}4)$$

where c and a are the lengths of median crack and half of the diagonal of the indentation, respectively. Hv is the Vickers hardness. For 3Y-TZP monolith and 3Y-TZP/SiC nanocomposite systems, heat treatment was carried out at 1300°C for 10 min in Ar to eliminate monoclinic phase generated by machining, and K_{IC} before and after the heat treatment were evaluated.

Quantitative analysis of monoclinic phase in 3Y-TZP[8]

To determine the content of m-ZrO_2 presented in the fracture surface of the specimens, the bent test piece was subjected to XRD, and the (111) and ($\bar{1}$11) reflections of m-ZrO_2 and the (111) of t-ZrO_2 were used. The volume fraction of the m-ZrO_2, V_m, was determined by using following equations,

$$V_m = PX_m/(1+(P-1)X_m) \qquad (3\text{-}5)$$

where P = 1.311 as a constant and X_m is the integrated intensity ratio determined by

$$X_m = (I_m(111)+I_m(\bar{1}11))/(I_m(111)+I_m(\bar{1}11)+I_t(111)) \qquad (3\text{-}6)$$

Subscripts m and t indicate the monoclinic and the tetragonal phases, respectively. I_m and I_t are the integrated intensities of these phases.

3.3 Results

3.3.1 3Y-TZP/SiC Composites

3.3.1.1 Mechanical Properties

Young's Modulus

Fig. 3-1 shows the variation of Young's modulus with the sintering temperature for 3Y-TZP monolith and 3Y-TZP/3-20 vol% SiC nanocomposites(3Y3S, 3Y5S, 3Y10S and 3Y20S). Young's modulus increased with increasing the density as described in Fig. 2-4 and with increasing volume fraction of SiC. After fully densified, Young's modulus was constant in all samples. These constant value coincides with theoretical value calculated by using the rule of mixture for spherical dispersoids as expressed by Eq. (3-7)[9],

$$\ln E_c = V_s \ln E_s + (1-V_s)\ln E_m \qquad (3\text{-}7)$$

where E and V_s are Young's modulus and volume fraction of second phase, subscript c, s and m indicate composite, second phase and matrix, respectively. Young's modulus for each 3Y-TZP microcomposites incorporating 5 and 20 vol% SiC with 1.2 μm, 4.0μm and 30 μm in

particle size (3Y5*1.2SM, 3Y5*4.0SM, 3Y5*30SM, 3Y20*1.2SM, 3Y20*4.0SM and 3Y20*30SM) are listed in Table 3-1. Young's modulus for 5 vol% microcomposites (3Y5SM), 3Y20*1.2SM and 3Y20*4.0SM were almost similar to that for nanocomposite, however, 3Y20*30SM has much lower Young's modulus. This should be due to generation of spontaneous microcrack as shown in Fig. 2-10.

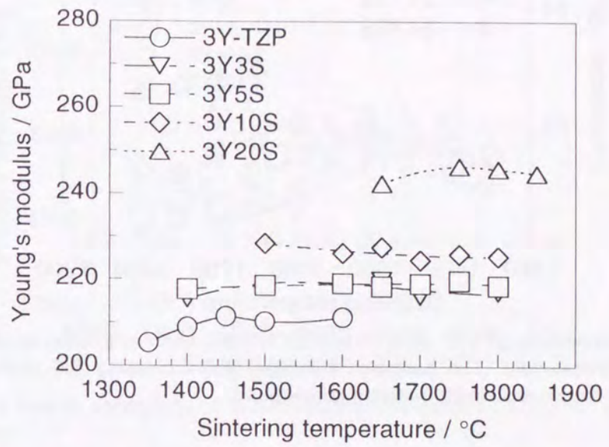

Fig. 3-1 The variation of Young's modulus for 3Y-TZP monolith and 3Y-TZP/SiC nanocomposites with the sintering temperature. Young's modulus increased as SiC content increased.

Hardness

Fig. 3-2 indicates the variation of hardness with the sintering temperature for 3Y-TZP monolith and 3Y3S, 3Y5S, 3Y10S and 3Y20S. The hardness increased with increasing the temperature, and then decreased, for instance, in the case of 3Y10S, the maximum value was obtained at 1600°C, and then hardness decreased. The increase in hardness is due to increase in density, on the other hand, the decrease is related to grain size. In general, the hardness reduces with increasing grain size. The relationship between hardness, H, and grain diameter, d, is expressed by Eq. (3-8)[10],

$$H = \frac{C}{d^{1/2}} \qquad (3\text{-}8)$$

where C is a constant. Hardness for microcomposites is shown in Table 3-1. The hardness for microcomposites becomes smaller than that for nanocomposites, and the hardness slightly decreased with the increasing SiC particle size.

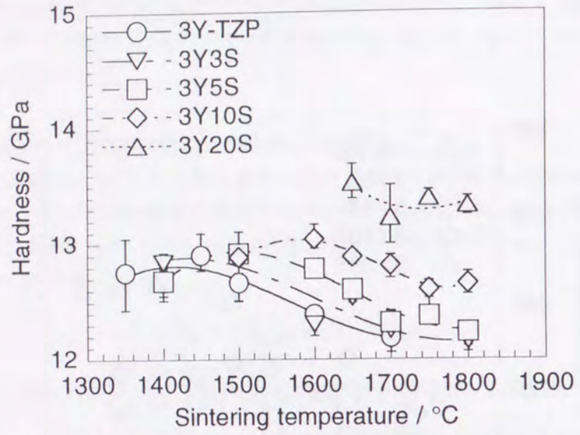

Fig. 3-2 The hardness for 3Y-TZP monolith and 3Y-TZP/SiC nanocomposites as a function of the sintering temperature. The hardness increased with increasing SiC content, which decreased with the increase in the sintering temperature.

Fracture Strength

The variations of fracture strength with the sintering temperature for 3Y-TZP monolith and 3Y3S, 3Y5S, 3Y10S and 3Y20S are shown in Fig. 3-3. The strength raised with increasing density, and then, maximum strength can be obtained over 1.5 GPa in each composition. There are little difference between the monolith and composites. Comparing microcomposites with nanocomposites, the former has lower strength, and the strength greatly reduced as the SiC particle size increased as shown in Table 3-1. 3Y20*4.0SM and 3Y20*30SM possessed low strength.

Fracture Toughness

Fracture toughness as a function of the sintering temperature for 3Y-TZP monolith, 3Y5S and 3Y20S are shown in Fig. 3-4. The toughness for the 3Y-TZP monolith and composites after annealing at 1300°C for 10 min in Ar flow are also displayed in Fig. 3-4. The toughness decreased after annealing, however, nanocomposites exhibited superior toughness to monolith both before and after annealing. The decrease in the toughness by annealing is due to the elimination of the surface imposed by residual compressive stresses by machining. It was confirmed that monoclinic phase was observed on the polished surface before annealing, however, the m-ZrO_2 conversely transformed to t-ZrO_2 after annealing. With

increasing the sintering temperature, the toughness for both monolith and composites were improved, because transformation from t-ZrO_2 to m-ZrO_2 can occur easily with increasing in grain size[11]. On the other hand, 3Y20SM exhibited higher fracture toughness than the nanocomposites.

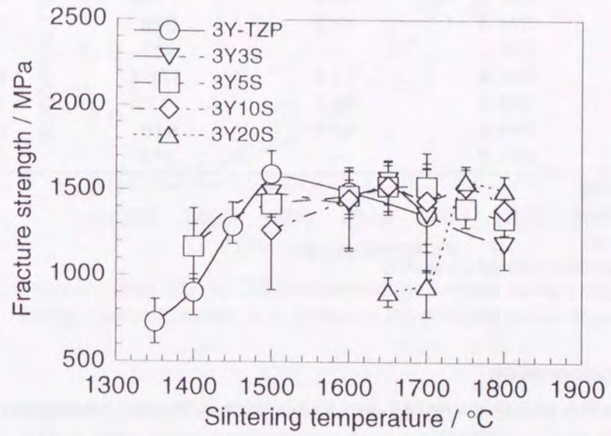

Fig. 3-3 The fracture strength for 3Y-TZP/SiC nanocomposites as a function of the sintering temperature.

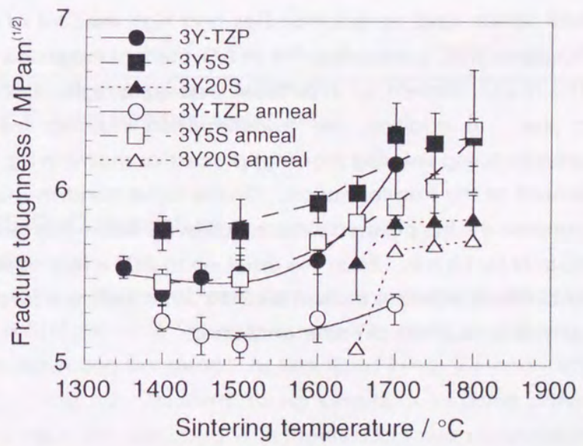

Fig. 3-4 The fracture toughness for 3Y-TZP monolith and 3Y-TZP/SiC nanocomposites as a function of the sintering temperature. The solid symbols mean the toughness before annealing and the open ones are that after annealing at 1300°C for 10 min in Ar.

Table 3-1 Mechanical properties for 3Y-TZP/5 vol% SiC nano and microcomposites sintered at 1700℃ and 3Y-TZP/20 vol% SiC nano and microcomposites sintered at 1750℃.

	E	*Hv*	σ	K_{IC}
3Y5S	218.7	12.4	1521	6.3
3Y5*1.2SM	218.7	12.4	1144	6.1
3Y5*4.0SM	221.6	12.2	926	6.3
3Y5*30SM	218.2	-	447	-
3Y20S	246.4	13.4	1554	5.8
3Y20*1.2SM	245.8	13.0	1172	6.5
3Y20*4.0SM	248.3	12.6	916	6.7
3Y20*30SM	219.4	-	374	-

E: Young's modulus
Hv: Vickers hardness
σ: Fracture strength
K_{IC}: Fracture toughness without annealing

3.3.1.2 Phase Transformation

Fig. 3-5 indicates the m-ZrO_2 content in fracture surface with the sintering temperature for 3Y-TZP monolith, 3Y5S and 3Y20S. The m-ZrO_2 increased with increasing sintering temperature. At same temperature, material with lower SiC content has higher m-ZrO_2 content, which means that the 3Y-TZP monolith can transform easily. Table 3-2 shows the m-ZrO_2 content for microcomposites. For 3 kinds of 5 vol% SiC microcomposites, m-ZrO_2 content were almost similar, and nanocomposites had high amount of m-ZrO_2 on the fracture surface. For 20 vol% SiC composites the m-ZrO_2 content increased with increasing SiC particle size. The m-ZrO_2 content for 3Y20*30SM was quite high. This is related to its large matrix grain size. In addition, the transformation induced the formation of spontaneous microcracks during sintering (cooling) process as shown in Fig. 2-10, and then m-ZrO_2 should be formed at the transformation. On the other hand, m-ZrO_2 produced by machining can be confirmed in the polished surface, however, the m-ZrO_2 disappeared after annealing at 1300°C in Ar for 10 min. From this result, no m-ZrO_2 which depend on the SiC dispersion might exist in the specimens except for 3Y20*30SM before a fracture. If the m-ZrO_2 pre-existed, the m-ZrO_2 must remain after annealing.

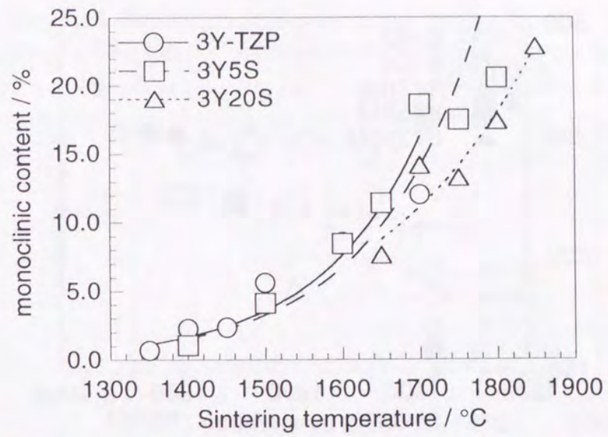

Fig. 3-5 The monoclinic ZrO_2 (m-ZrO_2) content in the fracture surface for 3Y-TZP monolith and 3Y-TZP/SiC nanocomposites as a function of the sintering temperature.

Table 3-2 Monoclinic ZrO_2 content on fracture surface for 3Y5S and 3Y20S nano- and microcomposites measured by XRD.

SiC particle size	5 vol% SiC / %*1	20 vol% SiC / %*2
0.15 μm (Nano)	19.7	17.3
1.2 μm	18.1	18.3
4.0 μm	17.9	21.4
30 μm	18.0	30.6

*1: Sintering temperature was 1700℃.
*2: Sintering temperature was 1750℃.

3.3.2 8YSZ/SiC Composites

Young's modulus

Fig. 3-6 shows the variation of Young's modulus with the sintering temperature for 8YSZ monolith and 8YSZ/5, 20 vol% SiC nanocomposites (8Y5S and 8Y20S). Young's modulus increased with increasing the density as described in Fig. 2-6 and with increasing volume fraction of SiC. After fully densified, Young's modulus became constant in all samples. These constant value are coincided with theoretical value calculated by using the rule of mixture as well as 3Y-TZP/SiC composites. Young's modulus for 8YSZ/5, 20 vol% SiC microcomposites (8Y5SM and 8Y20SM) were almost similar to that for nanocomposites.

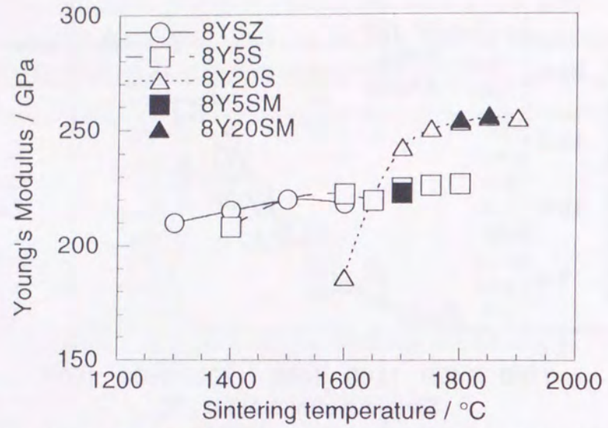

Fig. 3-6 The variation of Young's modulus for 8YSZ monolith and 8YSZ/SiC nano- and microcomposites with the sintering temperature. The open symbols mean nanocomposites and the solid ones the microcomposites. Young's modulus increased as SiC content increased and there is no difference between nano- and microcomposites.

Hardness

Hardness for 8YSZ monolith and 8YSZ/SiC nano- and microcomposites as a function of the sintering temperature are described in Fig. 3-7, which increased with increasing SiC content as well as Young's modulus. Although SiC content is same in both nano- and microcomposites, the nanocomposites exhibited higher hardness than microcomposites. This is related to the difference of grain size, and hardness reduced by grain growth, in general[10].

Strength

Fig. 3-8 displays fracture strength as a function of the sintering temperature for 8YSZ monolith and nano- and microcomposites. The strength for each composition increased with increasing the relative density. The monolithic 8YSZ sintered at 1400°C exhibited a maximum strength of 300 MPa, while the maximum strength of 8Y5S and 8Y20S were 580 and 750 MPa, respectively. The sintering temperature of those composites were 1700 and 1850°C. On the other hand, 8Y5SM sintered at 1700°C (8Y5SM1700) was 450 MPa and 8Y20SM at 1850°C (8Y20SM1850) was 550 MPa.

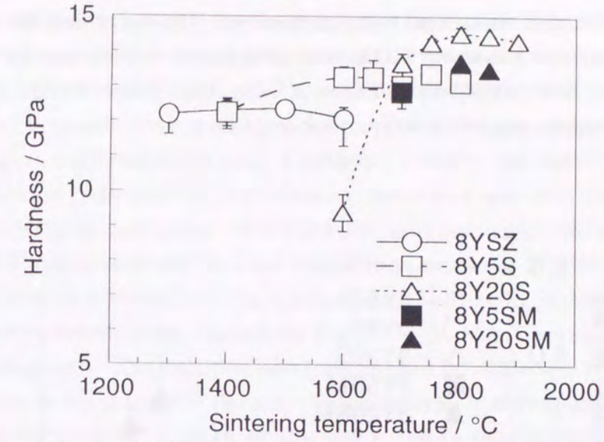

Fig. 3-7 The hardness for 8YSZ monolith and 8YSZ/SiC nano- and microcomposites as a function of the sintering temperature. The open symbols mean nanocomposites and the solid ones the microcomposites. The hardness increased with increasing SiC content, and the hardness for nanocomposite was higher than that for microcomposites.

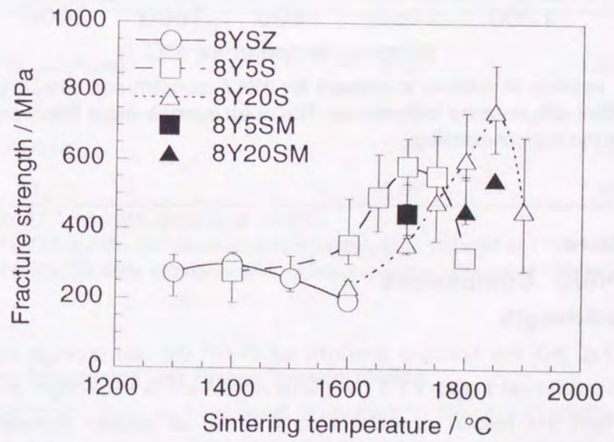

Fig. 3-8 The variation of fracture strength for 8YSZ monolith and 8YSZ/SiC nano- and microcomposites with sintering temperature. The open symbols mean nanocomposites and the solid ones the microcomposites. The strength improved by incorporating fine SiC particles.

Fracture toughness

Fig. 3-9 shows the variation of fracture toughness with the sintering temperature for 8YSZ monolith and 8YSZ/SiC nano- and microcomposites. The toughness for nanocomposites slightly increased with increasing SiC content, which were 2.0, 2.2 and 2.6 MPam$^{1/2}$ for 8YSZ monolith, 8Y5S and 8Y20S, respectively. On the other hand, microcomposites demonstrated higher toughness than nanocomposites.

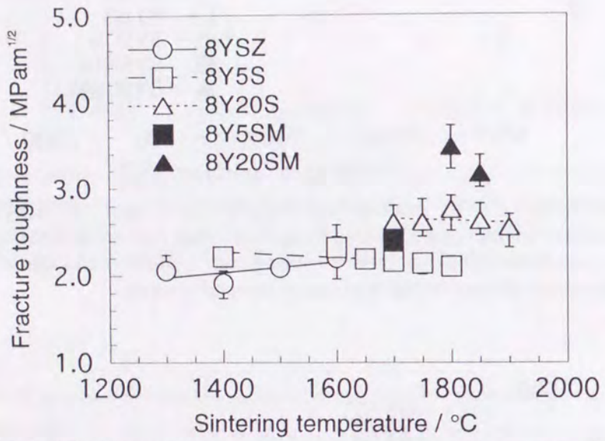

Fig. 3-9 The variation of fracture toughness for 8YSZ monolith and 8YSZ/SiC nano- and microcomposites with sintering temperature. The open symbols mean nanocomposites and the solid ones the microcomposites.

3.4 Discussions

3.4.1 3Y-TZP/SiC Composites

3.4.1.1 Fracture Strength

As shown in Fig. 3-3, the fracture strength for 3Y-TZP did not change by incorporating nano-sized SiC particles and about 1.5 GPa was achieved as maximum strength for each composition when the mixed powder was sintered at proper temperature in each composition. Microstructure greatly affects the mechanical properties, in particular for fracture strength. The relationship between strength, σ_f, and defect size, c, which relates to the microstructure is expressed as following equation[12],

$$\sigma_f = \frac{1}{Y}\frac{K_{IC}}{c^{1/2}} \qquad (3\text{-}9)$$

where Y and K_{IC} are shape factor of defect and the fracture toughness, respectively. The strength becomes high with decreasing defect size and is proportional to the toughness obviously. The toughness, which is discussed as following section, improved by dispersing SiC particles. The maximum grain size in the monolith sintered at 1500°C (3Y-TZP1500), the 3Y5S at 1700°C (3Y5S1700) and 3Y20S at 1750°C (3Y20S1750) which exhibit the maximum strength in each composition were 1.51 μm, 2.48 μm and 1.98 μm as shown in Table 3-3. The maximum grain size for densified body is generally similar to the defect size. The grain growth for 3Y-TZP during densification is suppressed compared with that for 8YSZ, however, the grain growth is slightly promoted. The maximum and mean grain size for fully densified composites, 3Y5S1700 and 3Y20S1750, are larger than those for 3Y-TZP1500. Since the strength depends on both defect size and fracture toughness, the large defect size is a main reason of no improvements in the strength for the 3Y-TZP/SiC nanocomposite in spite of the improving the toughness. On the other hand, micro-sized SiC dispersed 3Y-TZP composites exhibit a reduction in the strength. This is due to the increase in defect size. In the case of 3Y5*30SM and 3Y20*30SM, SiC particles and/or microcrack should be fracture origin.

Table 3-3 Maximum grain size for 3Y-TZP monolith, 3Y5S and 3Y20S nanocomposites with maximum strength in each composition and microcomposites.

SiC particle size	3Y-TZP1500 / μm*1	5 vol% SiC / μm*2	20 vol% SiC/ μm*3
	1.51		
0.15 μm (Nano)		2.48	1.98
1.2 μm		3.14	3.24
4.0 μm		3.44	4.02
30 μm		3.68	7.36

*1: 3Y-TZP monolith sintered at 1500℃.
*2: 3Y-TZP/5 vol% SiC nano- and microcomposites sintered at 1700℃.
*3: 3Y-TZP/20 vol% SiC nano- and microcomposites sintered at 1750℃.

3.4.1.2 Fracture Toughness and Phase Transformation

In general ceramics, fracture toughness is related to Young's modulus, E, and fracture energy, γ, which is necessary to propagate crack, and can be expressed by Eq. (3-10) [13].

$$K_{IC} = (2E\gamma)^{1/2} \qquad (3\text{-}10)$$

From this equation, the increase of Young' modulus as shown in Fig. 3-1 should be one of the factors to improve the toughness. Other factors included in fracture energy term, except

for the transformation toughening, would affect the toughness in this system. The fracture energy in Eq. (3-10) depends on some irreversible energy scatters and losses, and is expressed by Eq. (3-11)[14].

$$\gamma = (\gamma_S + \gamma_P + \gamma_{AE} + \gamma_D + \gamma_{etc})\mu \qquad (3\text{-}11)$$

where γ_S, γ_P, γ_{AE}, γ_D and γ_{etc} are thermodynamic surface energy, energy for the formation of process zone, energy for acoustic emission, dynamic energy and the other, respectively. The dynamic energy includes kinetic and oscillation energies for crack. μ is a coefficient. In addition to Young's modulus, lots of factor should affect the toughness. For instance, in the composites case, there are crack deflection, bridging and/or bowing[15]. For 3Y-TZP case, the phase transformability influences on the fracture toughness. In general, toughness improves when transformation easily occurs. As shown in Fig. 3-4, the fracture toughness increased by dispersing SiC particles. However, the amount of m-ZrO_2 in composites is smaller than in monolith at same sintering temperature as shown in Fig. 3-5. From this result, the fracture toughness for 3Y-TZP/SiC composites is affected not only by the phase transformation, but also by the addition of SiC. The improvement in toughness for 3Y-TZP/SiC nanocomposites should be attributed to the crack deflection and residual compressive stress toughening mechanisms which are effective in nanocomposite systems[16].

From now, the effect of SiC dispersion on the transformation is discussed. The toughness for transformation toughening materials, $K_{IC}{}^t$, can be expressed as following equation[17],

$$K_{IC}{}^t = K_{IC}{}^m + \frac{\eta V_t \Delta V E h^{1/2}}{1-\nu} \qquad (3\text{-}12)$$

where $K_{IC}{}^m$, η, V_t, ΔV, h and ν are fracture toughness for matrix, the constant, volume fraction of t-ZrO_2, coefficient of voluminal expansion, thickness of transformation zone and Poisson's ratio, respectively. From Eq. (3-12), it is obvious that the thickness of transformation zone is important factor on the toughness. Transformation relates to microstructure, i.e., grain size, and stabilizer content, impurity, temperature and defects[11,18,19,20,21,22,23]. Increasing stabilizer and temperature depressed the transformation[18] and increasing defect enhances martensitic nucleation and thus the transformation is promoted[19]. The phase transformation can easily occur with increasing grain size[11,20,21,22,23]. Fig. 3-10 shows the fracture toughness of 3Y-TZP monolith and 3Y5S as a function of the mean grain size after the surface compressive stress layer is eliminated by annealing. The 3Y5S exhibited higher toughness than the 3Y-TZP monolith at same grain size. The m-ZrO_2 content in the fracture surface as a function of the mean grain size is shown in Fig. 3-11. The m-ZrO_2 content increased with the grain size and the SiC content. These transformation behavior and

effects of SiC dispersion on the transformation will be explained following parts.

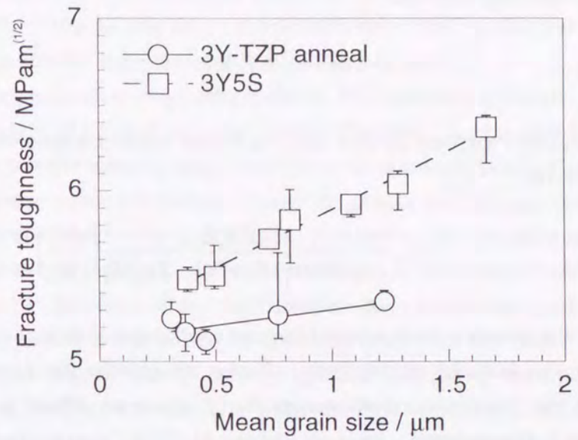

Fig. 3-10 The fracture toughness for 3Y-TZP monolith and 3Y-TZP/5 vol% SiC nanocomposites after annealing at 1300℃ for 10 min in Ar as a function of the mean grain size.

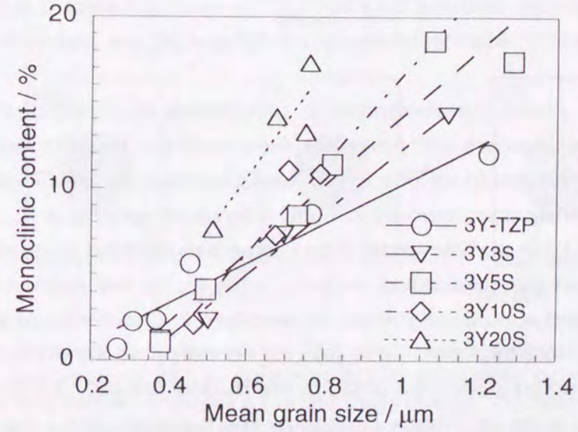

Fig. 3-11 The m-ZrO_2 content in the fracture surface for 3Y-TZP monolith and 3Y/TZP/SiC nanocomposites as a function of the mean grain size.

First, the effect of Young's modulus on the transformation will be considered. In the ZrO_2/SiC composite case, Young's modulus increases by adding SiC particles as shown in Fig. 3-1, and the composites have higher Young's modulus than monolith. According to Lange[21], the effect of the Young's modulus on the constraining matrix can be explained by assuming that the transformation only involves an isotropic volume expansion, ε^t, which can be expressed following equation,

$$\varepsilon^t = \frac{1}{3}\Delta V/V \qquad (3\text{-}13)$$

With this assumption, the strain energy of m-ZrO_2, U_{SE}, for the case of a spherical t-ZrO_2, can be expressed by Eq. (3-14),

$$U_{SE} = \frac{1}{6}\frac{2E_1E_2}{(1+\nu_1)E_2 + 2(1-2\nu_2)E_1}\left(\frac{\Delta V}{V}\right)^2 \qquad (3\text{-}14)$$

where E and ν are the Young's modulus and Poisson's ratio, and subscript 1 and 2 indicate matrix and transforming particles, respectively. That is, the greater the Young's modulus of constraining matrix, the greater the strain energy, thus it becomes difficult to transform from t-ZrO_2 to m-ZrO_2 due to the restraint. From this theory, 3Y-TZP/SiC composites which possess higher Young's modulus than monolith have strong constraint of the phase transformation. From experimental results, the increase in Young's modulus is about 10 GPa by incorporating 5 vol% SiC particulate. Therefore t-ZrO_2 grains should be restrained by the higher strain than monolith, and the transformation should be depressed. However, the results were different from this theory, and thus the effects of the residual stresses due to coefficient of thermal expansion (CTE) mismatch between 3Y-TZP and SiC are taken into consideration, secondly.

Generally, the phase transformation is progressed by applied stress, and the transformation rate increases with increasing the stress[24]. Thus, the increase in m-ZrO_2 content in composites should be due to the residual stresses by the CTE mismatch. First, only the effect of tensile stress imposed in matrix is discussed using Fig. 3-12. Initial state (a) and (b) in Fig. 3-12, t-ZrO_2 particle (grain) in both case is embedded in the material. In (a), no stress is imposed the surrounding material, while in (b) the residual tensile stresses including uniform and nonuniform stresses as described in Chapter 2 are imposed whole material. The transformation from (a) to (c) is the normal phase transformation, while from (b) to (c) is the phase transformation aided by the residual stresses. A t-ZrO_2 particle in Fig. 3-12 (c) undergoes a size and shape change by the transformation. The transformation from t-ZrO_2 to m-ZrO_2 accompanies volume expansion about 4.6 % in monolithic case[25], thus the material surrounding the particle will oppose the transformation, which is the strain

energy that involved in this constraint that allows the t-ZrO_2. On the other hand, when the stress for the transformation from (a) to (c) is defined by σ_n, and the residual tensile stress by σ_r, the stress required to transform (b) to (c) should be reduced by σ_r. Thus, the stress for the transformation is $\sigma_n - \sigma_r$. That is, comparing with the normal transformation, the transformation can easily occur under the imposition of the tensile stress. The theoretical residual tensile uniform stress in 3Y5S as shown in Table 2-3 can be assumed to be between 63 and 90 MPa. This tensile stress should enhance the transformation. However, this effect might be smaller than the effect of Young's modulus.

Next, the compressive stress imposed in SiC particles is taken into consideration. According to Choa[26], in the nanocomposites that the CTE of matrix is higher than that of second phase, the formation of dislocations around dispersed particles is caused by the high compressive stress which is imposed on second phase (i.e., SiC particulate), especially for the particles within the matrix grains. The dislocation can be observed in 3Y-TZP matrix grain as shown in Fig. 2-13 (a). As mentioned above, existence of defects promotes the transformation[19], therefore the transformation for composites easily occur comparing with the monolith due to the existence of the dislocations. The tensile stress increases and compressive stress decreases with increasing SiC content, while the localized stresses should increase. Thus, the transformation is enhanced by increasing SiC content, in spite of increasing Young's modulus by SiC addition. The transformability should be determined by the balance between Young's modulus and the residual stresses. From the result, the effect of residual stresses is more effective than increase of Young's modulus in the nanocomposite system.

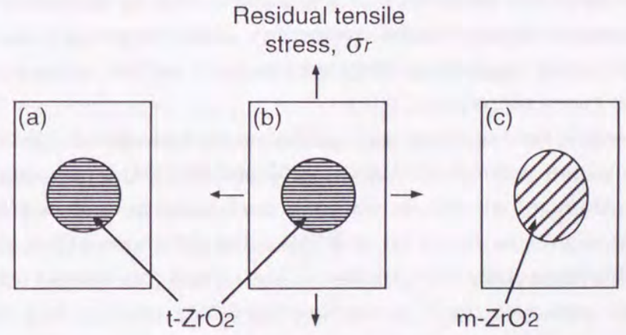

Fig. 3-12 The schematic illustration of the ZrO_2 phase transformation. The normal phase transformation from tetragonal ZrO_2 to monoclinic ZrO_2 is represented by going (a) to (c), and indicated that a ZrO_2 particle undergoes a size and shape change. The material surrounding the particle will oppose the transformation and it is the strain energy that involved in this constraint that allows the tetragonal ZrO_2 to be retained. the transformation from (b) to (c) can be aided by the residual tensile stress, σ_r, thus the transformation can occur easily with less stress.

On the other hand, the improvement in the toughness for microcomposites was also observed compared with 3Y-TZP monolith. 3Y5SM (3Y-TZP/5 vol% SiC microcomposites sintered at 1700°C) have a similar toughness as 3Y5S (3Y-TZP/5 vol% SiC nanocomposite sintered at 1700°C), in spite of small amount of m-ZrO_2 content, while the toughness of 3Y20SM (3Y-TZP/20 vol% SiC microcomposites sintered at 1750°C) increased with increasing SiC particle size and the m-ZrO_2 content also increased, compared with 3Y20S (3Y-TZP/20 vol% SiC nanocomposites sintered at 1750°C) as shown Tables 3-1 and 3-2. These behaviors can be explained as follows.

Next, the toughness and transformability for 3Y-TZP/5 vol% SiC nano- and microcomposite are discussed. An increased grain size with SiC particle size is shown in Fig. 2-11 and Table 2-2. That is, the transformation occurs more easily with increasing the SiC particle size. As can be seen, 3Y5S has high m-ZrO_2 content, and thus its transformation occurs more easily than 3Y5SM. In this composite system, the transformability depends on Young's modulus and the residual stresses as mentioned above. Effect of Young's modulus is taken into consideration; Young's modulus for 3Y5SM and 3Y5S are almost similar, which is about 218 GPa as shown in Table 3-1. Thus, the effect of Young's modulus is essentially the same for both composites.

Next, the effects of residual stresses will be discussed. In the microcomposite case, SiC particles were too large to be incorporated in the 3Y-TZP matrix grain. Therefore the both tensile and compressive stresses for microcomposites was smaller than those for nanocomposites as explained in Chapter 2. Thus the transformability for 3Y5S should be decreased comparing with that for nanocomposites. From experimental data, it can be seen that the toughness for 3Y5SM is almost same as that for 3Y5S, implying that there is other toughening mechanism for the composites. From these results, it is supported that except transformation toughening, bridging by large SiC particles act as a main toughening mechanism for microcomposites.

The difference of the toughness and transformability between 3Y-TZP/20 vol% SiC nano- and microcomposite sintered at 1750°C (3Y20S and 3Y20SM) is now considered. In the 3Y20SM, grain size increased with increasing SiC particle size as same as 3Y5SM, however its increasing rate was larger than that of 3Y5SM. The difference of the grain size strongly affects the transformability for 3Y20SM. The effect of Young's modulus on the transformability was quite small as mentioned in 3Y5SM case, so that the effect of the residual stresses is discussed. The residual stresses can be classified by uniform and nonuniform stresses as described in Chapter 2. Until now the residual stresses without distinction of uniform and nonuniform stresses are considered for the explanation. From now, they are strictly distinguished each other. The both tensile and compressive uniform stresses for microcomposites is smaller than those for nanocomposites as explained in Chapter 2, however, nonuniform stress for microcomposites, which should generate mainly

at grain boundary, is larger than that for nanocomposites. Thus localized stress for 3Y20SM is large, which increases with increasing SiC particle size. This localized stress should enhance the transformation. Especially, for 3Y20*30SM, spontaneous microcracks were generated by large localized stress to relax the stress, and then the transformation should occur accompanying microcrack formation. From those consideration, the improvement in the toughness for 3Y20SM is attributed to the increasing transformability due to large grain size, crack deflection and bridging by large SiC particles. In addition, microcracking is also important toughening mechanism for 3Y20*30SM.

3.4.2 8YSZ/SiC Composites

The fracture strength of 8YSZ was remarkably improved by incorporating SiC particles. Microstructure greatly affects the mechanical properties such as fracture strength and the relationship between strength and defect size as expressed by Eq. (3-9). Thus this remarkable improvement in the strength may be attributed to following reasons. The first is the refinement of the matrix grain size. Mean grain size of monolithic 8YSZ sintered at 1400°C was 7 μm, while nanocomoposites dispersed 5 and 20 vol% SiC were 3 and 1 μm, respectively, even though they were sintered at higher temperatures. In addition, from Fig. 2-14, the homogeneity in the matrix grain size distribution is given as a second reason. When large grain exists in the material, the grain becomes fracture origin. The relationship between (maximum grain size)$^{-1/2}$ and fracture strength for almost fully densified specimen is shown in Fig. 3-13. Densified 8YSZ, 8Y5S and 8Y20S exhibit that the strength is in proportional to (maximum grain size)$^{-1/2}$, so that the improvement in strength must be due to reduction of defect size, which is caused by the refine and homogenized microstructure by adding fine SiC particles. As expressed by Eq. (3-9), the strength relates to the fracture toughness, next, the effect of SiC particle on the toughness is investigated.

The improvement in the fracture toughness also affected the improvement in the strength. Increase in Young's modulus as shown in Fig. 3-6 should contribute to improvement in both the toughness and strength. In addition, the increase in fracture toughness is attributed to the crack deflection at crack tip by second phase. As shown in Fig. 3-14, the crack propagated straight through the 8YSZ grains for the monolith, while it was deflected by SiC particle for the 20 vol% SiC nanocomoposite. Therefore crack deflection may contribute to the toughness improvement in the composites. Faber et al.[27] reported the theoretical prediction of improvement in toughness only by deflection for various shapes of dispersion phase. According to their results, the toughness increment can be estimated about 20 % for 20 vol% SiC composite when SiC particulate is dispersed as a second phase. Theoretical and experimental fracture toughness are shown in Fig. 3-15, and the experimental results agreed well with theoretical one. The improvement in

toughness observed in this work may be mainly caused by the deflection at crack tip due to SiC particles. The deflection may be caused as a result of the stresses associated with differential Young's modulus and the coefficients of thermal expansion mismatch.

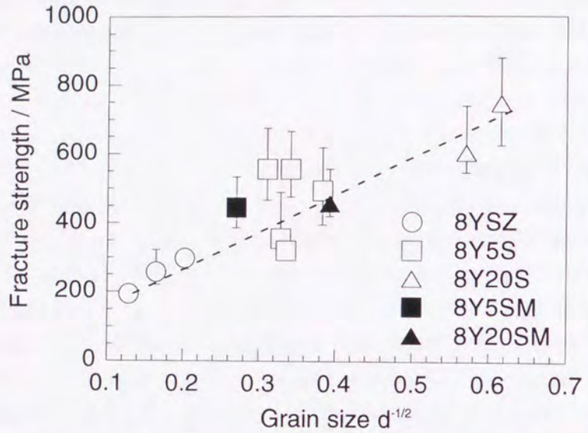

Fig. 3-13 The relationship between the strength and (maximum grain size)$^{-1/2}$ for 8YSZ monolith and 8YSZ/SiC nano- and microcomposites. The open symbols mean nanocomposites and the solid ones the microcomposites.

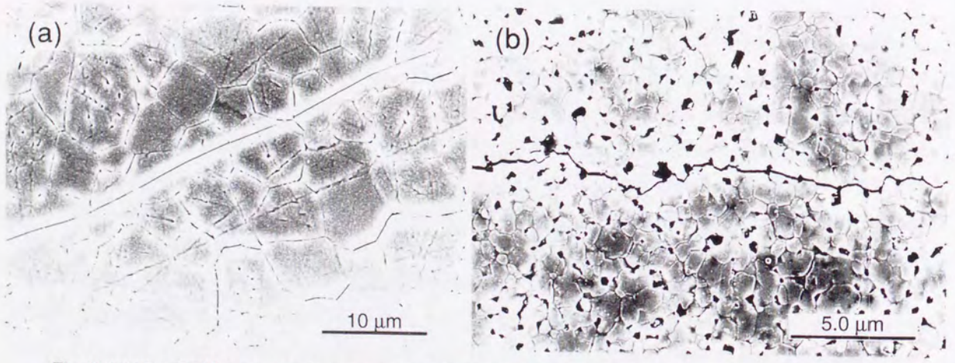

Fig. 3-14 The SEM images of crack propagation for (a) the 8YSZ monolith sintered at 1400℃ and (b) the 8YSZ/20 vol% SiC nanocomposite at 1800℃.

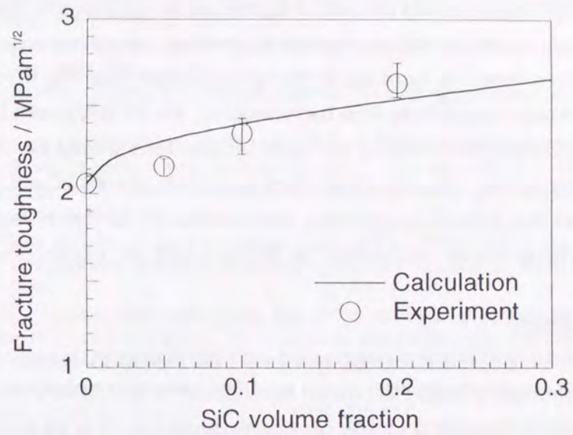

Fig. 3-15 The theoretical fracture toughness improved by crack deflection due to second phase and the experimental fracture toughness as a function of SiC volume fraction. The solid line and open circle are theoretical and experimental toughness, respectively.

3.5 Conclusions

In this chapter, the mechanical properties for 3Y-TZP/SiC and 8YSZ/SiC nano- and microcomposites were evaluated. The effects of SiC dispersion on the properties were investigated including the effect of their microstructure discussed in Chapter 2. For 3Y-TZP/SiC composites, the effects of SiC particulate on the phase transformation were also studied. Following conclusions were obtained.

3Y-TZP/SiC composites

Young's modulus and hardness increased with increasing SiC content.

The maximum fracture strength for each composition was about 1.5 GPa, no effect of SiC dispersion was observed. This is due to grain growth during sintering, because higher sintering temperature is necessary to densify the composites as SiC content increases. On the other hand, the strength for microcomposites strongly decreased with increasing SiC particle size, which is attributed to the increase of defect size by grain growth and large SiC particles.

The toughness was improved by SiC addition. This is due to crack deflection, crack shielding by the residual stresses and the increase in transformability. The phase transformability for each composition should be determined by the balance among following effects: Young's modulus of the material surrounding transformed particles which

suppresses the transformation, and the residual stresses which depend on CTE mismatch between 3Y-TZP and SiC and morphology. The tensile stress helps t-ZrO_2 to transform to m-ZrO_2, and dislocation, formed around intragranular SiC particles to relax the high residual compressive stress, promotes the martensitic nucleation. In this system, the residual stresses are more effective than the increase in Young's modulus, thus the transformability for the nanocomposites was larger than that for monolith. For 3Y-TZP/5 vol% SiC microcomposite case, the crack deflection, bridging by large SiC particles should be main reasons of the toughness improvement. On the other hand, for 3Y-TZP/20 vol% SiC microcomposites, large matrix grain and microcrack toughening also contribute to the increase in toughness, in addition to the toughening mechanism for 3Y-TZP/5 vol% SiC microcomposite.

8YSZ/SiC composites

Young's modulus and hardness increased with increasing SiC content.

The fracture strength strongly improved from 300 MPa to 750 MPa by 20 vol% nano-sized SiC addition. This is attributed to fine and homogeneous microstructure achieved by SiC addition.

The fracture toughness was also improved from 2.0 to 2.6 $MPam^{1/2}$ due to the crack deflection by SiC particles at the crack tip.

References

1 K. Niihara, New design concept of structural ceramics-ceramic nanocomposites. J. Ceram. Soc. Jpn., 99 [10](1991) 974-982.
2 M. Sternitzke, Structural ceramic nanocomposites, J. Eur. Ceram. Soc., 17 (1997) 1061-1082.
3 G. Sasaki, H. Nakase, K. Suganuma, T. Fujita and K. Niihara, Mechanical properties and microstructure of Si_3N_4 matrix composite with nano-meter scale SiC particles, J. Ceram. Soc. Jpn., 100 [4](1992) 536-540.
4 K. Niihara, A. Nakahira, T. Uchiyama and T. Hirai, High-temperature mechanical properties of Al_2O_3-SiC composites, in Fracture Mechanics of Ceramics, vol. 7, Eds. by R. Bradt, A. G. Evans, D. P. H. Hasselman and F. F. Lange, Plenum Press, New York, 1986, pp. 103-116.
5 E. Yasuda, Q. Bao and K. Niihara, The effects of fine SiC particles on the creep of MgO at high temperature, J. Ceram. Soc. Jpn., 100 [4](1992) 514-519.
6 M. V. Swain and L. R. F. Rose, Strength limitations of transformation-toughened zirconia alloys, J. Am. Ceram. Soc., 69 [7](1986) 511-518.
7 K. Niihara, R. Morena and D. P. H. Hasselmam, J. Mater. Sci. Lett., 1 (1982) 13-16.
8 H. Toraya, M. Yoshimura and S. Somiya, Calibration curve for quantitative analysis of the monoclinic-tetragonal ZrO_2 system by X-ray diffraction, J. Am. Ceram. Soc., 67 [6](1984) C119-C121.
9 Y. Kagawa and H. Htta, Tailoring Ceramic Composites (in Jpn), Agune Shouhusha, Tokyo, 1990, p. 97.
10 I. J. McColm, Ceramic Hardness, Plenum Press, London, 1990, p.120.
11 M. V. Swain, Grain size dependence of toughness and transformability of 2 mole % Y-TZP ceramics, J. Mater. Sci. Lett., 5 (1986) 1159-1162.
12 Kingery, W. D., Bowen, H. K. and Uhlmann, D. R., Introduction to Ceramics, 2nd Ed, John Wiley & Sons, Now York, 1976, pp. 783-790.
13 T. Nishida, Mechanical Properties Evaluation for Ceramics (in Jpn), Eds. by T. Nishida and E. Yasuda, Nikkan Kogyo Press, 1986, Tokyo, p. 100.
14 T. Nishida, Mechanical Properties Evaluation for Ceramics (in Jpn), Eds. by T. Nishida and E. Yasuda, Nikkan Kogyo Press, 1986, Tokyo, p. 98.
15 Y. Kagawa and H. Htta, Tailoring Ceramic Composites (in Jpn), Agune Shouhusha, Tokyo, 1990, pp. 120-126.
16 T. Ohji and K. Niihara, Comments on "physical limitations of the inherent toughness and strength in ceramic-ceramic and ceramic-metal nanocomposites", J. Ceram. Soc. Jpn., 104 [6](1996) 581-582.
17 R. M. McMeeking and A. G. Evans, Mechanics of transformation-toughening in brittle materials, J. Am. Ceram. Soc., 65 [5](1982) 242-246.
18 M. Yoshimura, Phase stability of Zirconia, Ceram. Bull., 67 [12](1988) 1950-1955.
19 I. W. Chen, Y. H. Chiao and K. Tsuzaki, Statistics of martensitic nucleation, Acta Metall. 33 [10](1985) 1847-1859.
20 F. F. Lange and D. J. Green, Effect of inclusion size on the retention of tetragonal ZrO_2: theory and experiments, in Advances in Ceramics, vol. 3, Science and Technology of Zirconia, Eds. by A. H. Heuer and L. W. Hobbs, Am. Ceram. Soc., Ohio, 1981, pp. 217-225.
21 F. F. Lange, Transformation toughening Part 1 Size effects associated with the thermodynamics of constrained transformations, J. Mater. Sci., 17 (1982) 225-534.
22 I. Müller and W. Müller, Size effect on transformation temperature of zirconia powders and inclusions, in Advances in Ceramics, vol. 12, Science and Technology of Zirconia II, Eds. by N. Claussen, M. Rühle and A. H. Heuer, Am. Ceram. Soc., Ohio, 1984, pp. 443-454.
23 R. C. Garvie and M. V. Swain, Thermodynamics of the tetragonal to monoclinic phase transformation in constrained zirconia microcrystals Part 1 in the absence of an applied stress field, J. Mater. Sci., 20 (1985) 1193-1200.
24 M. Matsui, T. Soma and I. Oda, Stress-induced transformation and plastic deformation for Y_2O_3-containing tetragonal zirconia polycrystals, J. Am. Ceram. Soc., 69 [3](1986) 198-202.
25 Cyclopedia of Fine Ceramics (in Jpn), Eds. by H. Yanagida et al., Gihodo Press, Tokyo, 1987, p. 218.
26 Y. H. Choa, Ph. D. thesis, Osaka University, 1996.
27 Faber, K. T., Evans, A. G. and Drory, M. D., A statistical analysis of crack deflection as a toughening mechanism in ceramic materials. In Fracture Mechanics of Ceramics, Vol. 6, Eds. by R. C. Bradt, A. G. Evans, D. P. H. Hasselman and F. F. Lange, Plenum press, New York, 1983, pp. 77-91.

4 High Temperature Mechanical Properties of ZrO_2/SiC Composites

4.1 Introduction

An increasing demand for high performance materials in modern-day technology has begun to emerge ceramics as attractive candidates for certain engineering applications both at ambient and elevated temperatures. The 3 mol% Y_2O_3 stabilized ZrO_2 (3Y-TZP)/SiC and 8 mol% Y_2O_3 stabilized ZrO_2 (8YSZ)/SiC nanocomposites have excellent mechanical properties at ambient temperature as described in Chapter 3. However, it has been reported that tetragonal ZrO_2 polycrystals (TZP) greatly degrade in its strength and toughness with increasing temperature, because of the lock in transformation toughening at high temperatures[1,2,3,4]. If the strength and toughness for TZP at high temperatures were improved, TZP based materials would be more attractive candidate for advanced structural applications, such as engine components. In fact, various types of composites, which include SiC and Al_2O_3 whiskers, fibers, platelet or particles, have been studied to improve high-temperature mechanical properties of TZP[5,6,7,8]. Tsukuma et al.[8] reported that strength of the Y-TZP/20 wt% Al_2O_3 composite was 700 MPa at 1000°C, while that of the Y-TZP monolith was 300 MPa at 1000°C. It is also important to improve the high temperature mechanical properties of 8YSZ, because it is used as a solid oxide fuel cell (SOFC) for high temperatures. The increase in high-temperature strength will widen its application.

Ceramic materials reinforced by nano-sized SiC particles have been reported to show superior mechanical properties even at high temperatures due to inhibition of the grain boundary sliding by SiC particles at grain boundaries[9,10,11,12].

In this chapter, high-temperature fracture strength of 3Y-TZP/SiC and 8YSZ/SiC nanocomposites was evaluated up to 1400°C, and the role of SiC dispersion on the strength was investigated. For 3Y-TZP/SiC composites, high-temperature fracture toughness was also evaluated by the single edge pre-cracked beam (SEPB) method.

4.2 Deformation Mechanism at High Temperatures

In general, ceramics with high melting point show brittle-fractured without plastic deformation at ambient temperature. However, plastic deformation and/or creep behavior can occur at elevated temperatures even brittle ceramics. It is important to make clear the deformation and fracture behavior at high temperatures when the materials are applied as structural materials. Characteristic phenomena observed in

fracture for ceramics at high temperatures are as follows[13]: (i) slow crack growth (SCG) that crack propagates along grain boundaries under the stress to extend the crack, (ii) blunting of crack tip and (iii) plastic deformation and creep. The plastic deformation for ceramics at high temperatures is caused mainly by dislocation climb, diffusional creep and grain boundary slip described as follows. The deformation of ceramics greatly depends on not only the temperature but also microstructure (i.e., grain size and porosity).

Dislocation climb[14]

Dislocation climb, that is the movement of dislocations out of their slip planes, requires a diffusional kind of jump of an atom above the dislocation line into the dislocation, and the climb process depends on the diffusion of lattice vacancies and the rate of deformation is controlled by diffusion. In the case of polycrystal ceramics, grain boundaries act as barriers to the glide of dislocations, and each grain blocks the shear of others with the result that the aggregate is not ductile. The grain size is important in determining the yield and fracture strength of ceramics. The Petch equation shows the relationship between the yield strength, σ, and the grain size, d, for a material which deforms by dislocation glide,

$$\sigma = \sigma_i + B/d^{1/2} \qquad (4\text{-}1)$$

where, B and σ_i are a constant and the friction stress which is a measure of the lattice resistance against deformation. The dislocation slip is a dominant mechanism for deformation at lower temperatures and high stress, and also controls deformation at high temperatures for the material consists of large grains. In general, ceramics are difficult to deform plastically by dislocation climb at ambient temperature, because Peierls stress for ceramics is larger than that for metals.

Diffusional creep[15]

In diffusional, or Nabarro-Herring, creep process, self-diffusion within grains of a polycrystalline solid allows the solid to yield under an applied stress. Deformation results from diffusional flow within each grain away from those boundaries where there is a normal compressive force (high chemical potential) toward boundaries having a normal tensile stress as shown in Fig. 4-1. The deformation by diffusional creep is always accompanied by grain boundary sliding.

Grain boundary sliding[16]

Grain boundary sliding is an important deformation mechanism in polycrystalline ceramic materials. It dominates the plastic flow in ultrafine grained ceramics and ceramic matrix composites at elevated temperatures. In the polycrystalline solid, grain boundary sliding is an integral part of diffusional creep. The total process can be treated either as

deformation by diffusional creep with grain boundary sliding, or as deformation by grain boundary sliding with diffusional creep.

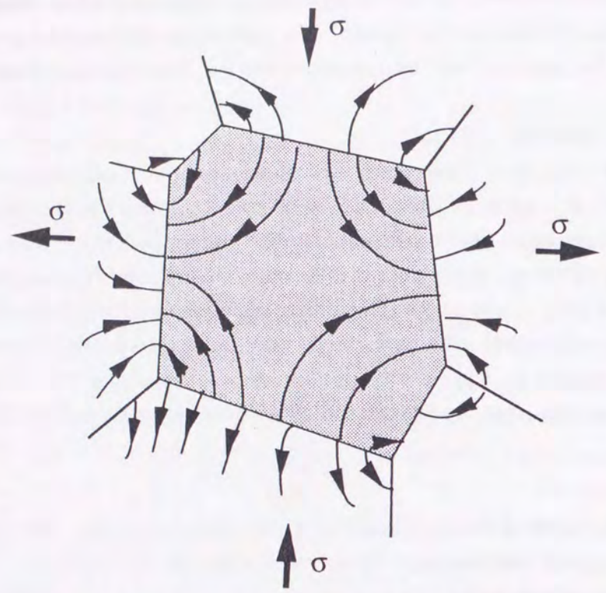

Fig. 4-1 Schematic illustration of Nabarro-Herring creep.

4.3 Experimental Procedure

4.3.1 Specimen Preparation

ZrO_2 (3Y-TZP and 8YSZ) monoliths and ZrO_2/SiC nanocomposites were fabricated using a conventional method as descried in Chapter 2. Sintered materials were machined into rectangular bar specimens (3 x 4 x 36 mm) for evaluation of strength and (3 x 4 x 18 mm) for toughness, respectively. The specimens were polished with 0.5 μm diamond paste and their edges of tensile surface were beveled at about 45° to avoid the fracture from the specimen edges. The detail of each sample was shown in Tables 4-1 and 4-2.

Table 4-1 Characteristic properties of the 3Y-TZP monolith and 3Y-TZP/SiC nanocomposites for high-temperature mechanical properties measurement.

	R. density / %	Grain size / μm	R.T. σ / MPa	R.T. K_{IC} / MPam$^{1/2}$
3Y-TZP1500	100	0.465	1595	3.65
3Y5S1700	100	1.083	1521	4.71
3Y20S1750	100	0.752	1554	4.76

3Y-TZP1500 : 3Y-TZP monolith sintered at 1500℃
3Y5S1700 : 3Y-TZP/5 vol% SiC nanocomposite sintered at 1700℃
3Y20S1750 : 3Y-TZP/20 vol% SiC nanocomposite sintered at 1750℃
R. density : Relative density
R.T. σ : Fracture strength at room temperature
R.T. K_{IC} : Fracture toughness at room temperature measured by SEPB method

Table 4-2 Characteristic properties of the 8YSZ monolith and 8YSZ/SiC nanocomposites for high-temperature strength measurement.

	R. density / %	Grain size / μm	R.T. σ / MPa
8YSZ1400	99.3	6.98	297.9
8Y5S1700	100	2.62	584.2
8Y20S1850	100	1.03	746.6

8YSZ1400 : 8YSZ monolith sintered at 1400℃
8Y5S1700 : 8YSZ/5 vol% SiC nanocomposite sintered at 1700℃
8Y20S1850 : 8YSZ/20 vol% SiC nanocomposite sintered at 1850℃
R. density : Relative density
R.T. σ : Fracture strength at room temperature

4.3.2 Evaluations

Fracture Strength

Fracture strength at high temperatures was measured by three point bending method using and universal testing machine (Autograph, model AG-10TC, Shimazu Co. Ltd., Japan) in Ar. Crosshead speed and the span were 0.5 mm/min and 30 mm, respectively. The strength was given by Eq. (3-3).

Fracture Toughness

Fracture toughness at high temperatures was measured by SEPB method[17] with span of 16 mm at crosshead speed of 0.5 mm/min in an Ar atmosphere up to 1400°C as described follows. Vickers indentation was placed at the center of the polished surface (tensile plane) with load of 98 N. The indented specimen was located on the supporting groove of the anvil as illustrated in Fig. 4-2, and then the crack starter was aligned with the center of

the bridge configuration. The load was applied to the specimen, and increased gradually until a pop-in sound was detected. The load was immediately released after the introduction of pop-in crack. Three point bending measurement was conducted to the specimen with pre-crack. The toughness, K_{IC} (MPam$^{1/2}$), was calculated from the pre-crack length, *a*, as illustrated in Fig. 4-3 using Eq. (4-2),

$$K_{IC} = \frac{PS}{BW^{3/2}} f(a/W) \times 0.3101 \qquad (4\text{-}2)$$

where *P*, *S*, *B* and *W* are fracture load (kgf), the span (in this case, 16 mm), thickness of specimen (3 mm) and width of specimen (4 mm), respectively, and in the case that *S/W* is 4, *f(a/W)* is expressed as following Eq. (4-3),

$$f(a/W) = 3(a/W)^{1/2} \frac{1.99 - (a/W)(1-(a/W))(2.15 - 3.93(a/W) + 2.7(a/W)^2}{2(1+2(a/W))(1-a/W)^{3/2}} \qquad (4\text{-}3)$$

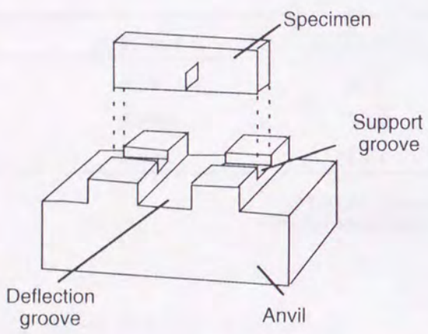

Fig. 4-2 Perspective view of an anvil. Central groove for the deflection of a specimen surface a pair of support grooves perpendicular to it, and side cut to keep the support span from being not more than the specimen length.

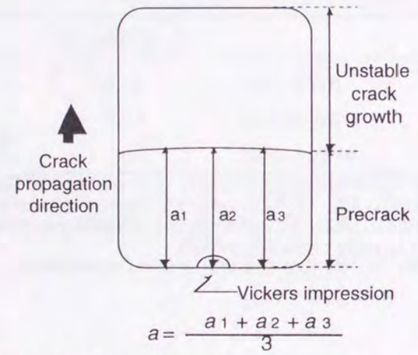

Fig. 4-3 Schematic illustration of fracture surface precracked and tested by three-point bending.

4.4 Results and Discussions

4.4.1 3Y-TZP/SiC Nanocomposites

Fracture Strength

Fig. 4-4 shows the variation of fracture strength as a function of the test temperature for 3Y-TZP monolith sintered at 1500°C (3Y-TZP1500), 3Y-TZP/5 vol% SiC nanocomposite at 1700°C (3Y5S1700) and 3Y-TZP/20 vol% SiC at 1750°C (3Y20S1750). These three specimens have similar strength at room temperature, about 1.5 GPa as shown in Chapter 3. The grain size of the specimens was different from each other, which becomes smaller in the order of

3Y5S1700, 3Y20S1750 and 3Y-TZP1500 as described in Chapter 2. The high-temperature strength for monolith and nanocomposites rapidly decreased with increasing test temperature. This is probably due to the decrease in transformation toughening effect. The tetragonal phase is more stable with increasing temperature, and then the transformation from tetragonal (t-ZrO_2) to monoclinic (m-ZrO_2) is hard to occur. As mentioned in Chapter 3, the transformation toughening for composites is enhanced by the residual stresses, compared with 3Y-TZP monolith. However, the stresses are gradually reduced with increasing temperature. Although the enhancement of transformation toughening for nanocomposites should be gradually decreased with decrease in the stresses, it is considered that the transformation toughening affects the mechanical properties for composites until the stresses are perfectly released. Therefore the decrease in the strength for composites with temperature was smaller than that for 3Y-TZP monolith, even though the strength for 3Y-TZP does not change by incorporating SiC particulate at room temperature. However, most of the stresses should be released at 1200°C, the composites exhibited still higher strength than monolith. Thus other factors which generated the difference between monolith and composites are considered as follows.

Fig. 4-5 displays the load/displacement for 3Y-TZP1500, 3Y5S1700 and 3Y20S1750 at (a) 600°C and (b) 1200°C. Young's modulus can be estimated from the slope in the load/displacement curve, Young's modulus for 3Y20S1750 was higher than that of 3Y-TZP not only at room temperature as show in Fig. 3-3, but also at elevated temperatures in Fig. 4-

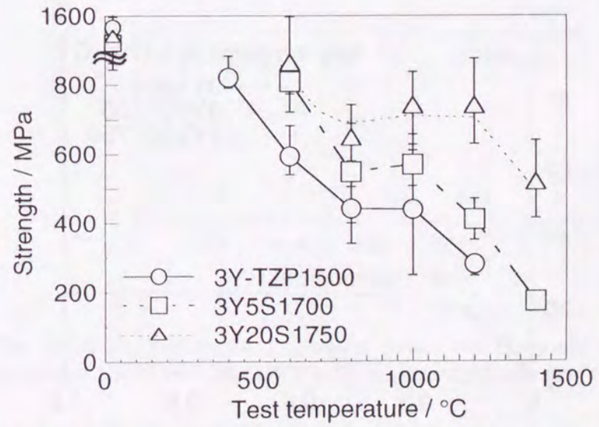

Fig. 4-4 The fracture strength as a function of temperature for 3Y-TZP monolith sintered at 1500°C, 3Y-TZP/5 vol% SiC nanocomposite at 1700°C and 3Y-TZP/20 vol% SiC at 1750°C.

5. This is due to SiC particulate with high Young's modulus. The strength for composites should be higher than that for monolith due to the improvement of Young's modulus, because strength is proportional to the square root of Young's modulus as explained by Eqs. (3-9) and (3-10). The typical load/displacement curves at various test temperatures for 3Y-TZP1500 and 3Y20S1750 are indicated in Figs. 4-6 (a) and (b). Young's modulus became small with increase in temperature obviously. This decrease in Young's modulus also results in the strength degradation.

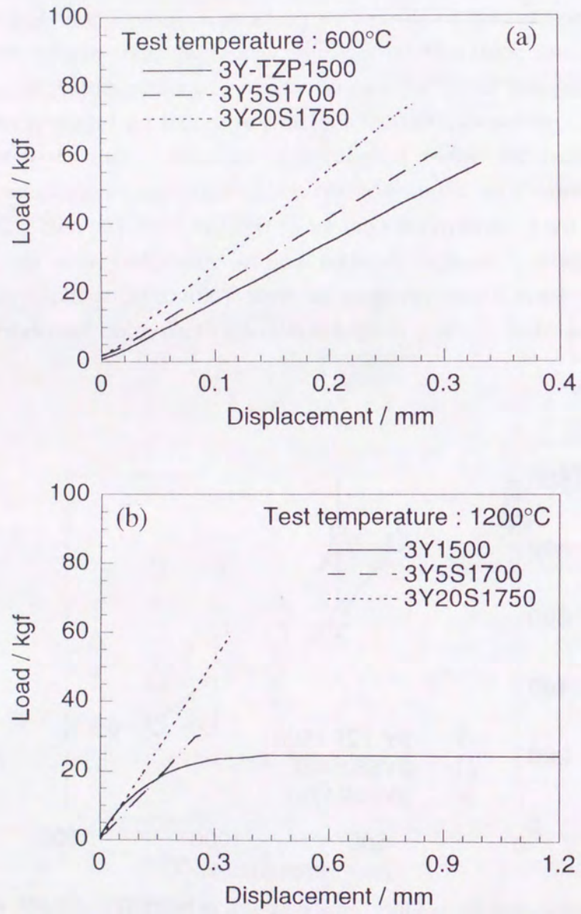

Fig. 4-5 The load/displacement at (a) 600℃ and (b) 1200℃ for 3Y-TZP monolith sintered at 1500℃, 3Y-TZP/5 vol% SiC nanocomposite at 1700℃ and 3Y-TZP/20 vol% SiC at 1750℃.

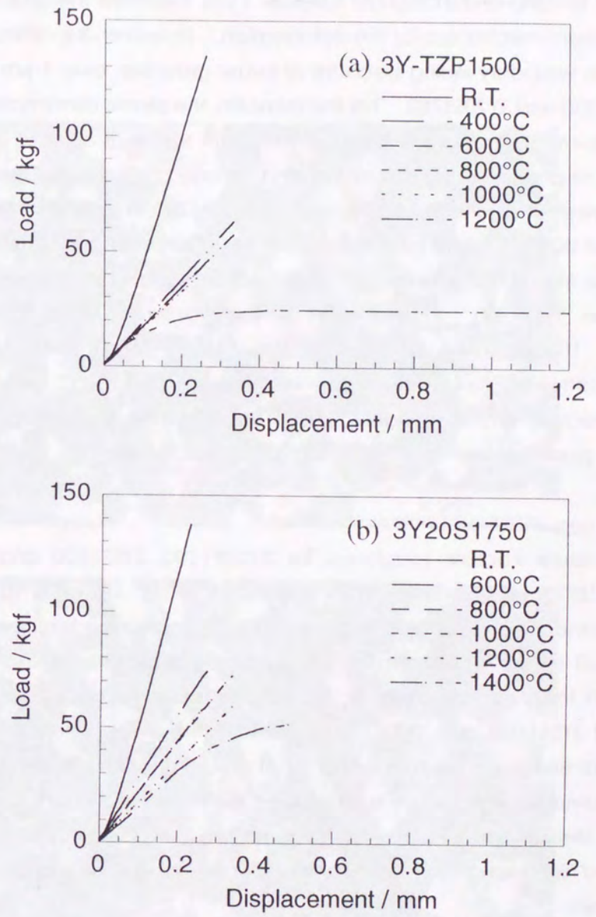

Fig. 4-6 The typical load/displacement curves at various test temperatures for 3Y-TZP monolith sintered at 1500℃ and 3Y-TZP/20 vol% SiC nanocomposite at 1750℃.

In the both cases of monolith and composites, yielding and nonlinear behavior were observed, but the yielding temperature for each specimen was different: 1200°C for monolith and 1400°C for composites. Generally, the deformation behavior changes from slip to diffusional creep with decreasing grain size, and when grain size is under sub-micron and equiaxis, the plastic deformation occurs by grain boundary sliding. In this system, the grain size for 3Y-TZP1500 and 3Y20S1750 is below 1 μm, therefore the grain boundary sliding should be dominant mechanism for the deformation. However, it is difficult for 3Y5S1700 to deform by grain boundary sliding because of larger grain size, over 1 μm, compared with that for 3Y-TZP1500 and 3Y20S1750. For the monolith, the plastic deformation behavior was observed at lower temperature, because its grain size was smaller than that of the composites. This phenomenon should depend on only grain size, because 3Y5S1700 was deformed by lower stress and temperature than 3Y20S1750, in spite of large grain size. Thus, it is obvious that SiC particulate inhibits the grain boundary sliding in composite cases. The deformation for 3Y20S1750 with lots of SiC particles at grain boundaries should be more depressed than 3Y5S1700. SEM images of the fracture surface for 3Y-TZP1500 and 3Y20S1750 at 1000°C are exhibited in Fig. 4-7. For the composites, obvious transgranular/brittle fractures was observed even at 1200°C, while for monolith, intergranular fracture was dominant. This is an evidence that added SiC particulate depressed the plastic deformation via the grain boundary sliding.

Fracture Toughness

High-temperature fracture toughness for 3Y-TZP1500, 3Y5S1700 and 3Y20S1750 was evaluated by SEPB method. The results are shown in Fig. 4-8. The toughness for both monolith and nanocomposites rapidly decreased with increasing temperature. This is due to normal fall-off of the transformation toughening effect with increasing temperature. Compared with the monolith, however, the toughness for the composites was higher and in the order of 3Y5S1700 and 3Y20S1750. Generally, the toughness for 3Y-TZP materials greatly depends on the phase transformation at ambient temperature, and thus the higher toughness of composites should be attributed to the enhanced transformation toughening by the residual stresses similar to at room temperature. In addition, the crack deflection at SiC particles and high Young's modulus should also influence the increase in the toughness for composite cases.

On the other hand, the increase in toughness was observed after decrease in the toughness. The toughness of 3Y-TZP monolith increased above 1200°C, while the increase in the toughness for composites was observed above 1400°C. The temperatures of 1200°C and 1400°C for monolith and composites were coincided the temperatures that exhibited plastic deformation for each sample as mentioned above. Thus the increase in the toughness might be attributed to the plastic deformation and/or crack blunting. SiC

dispersion has large effect on inhibition of the grain boundary sliding, and thus the temperature that the increase in the toughness was observed for composites should be higher than that for monolith.

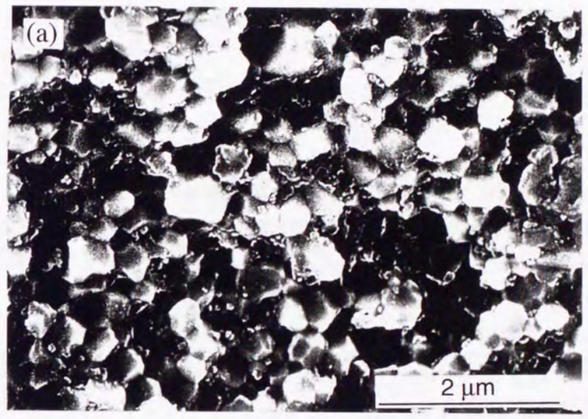

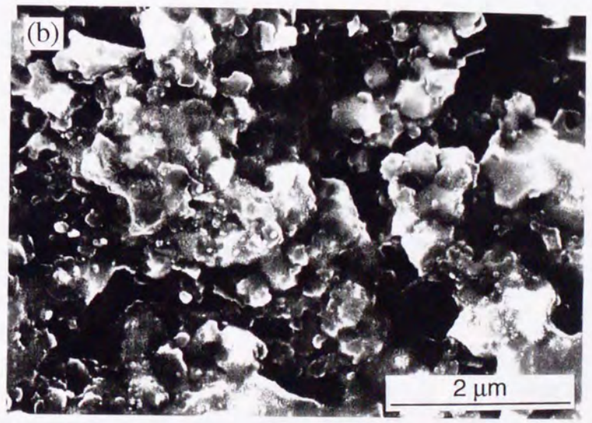

Fig. 4-7 SEM images of the fracture surface for (a) 3Y-TZP monolith sintered at 1500℃ and (b) 3Y-TZP/20 vol% SiC nanocomposite at 1750℃ at 1000℃ in test temperature.

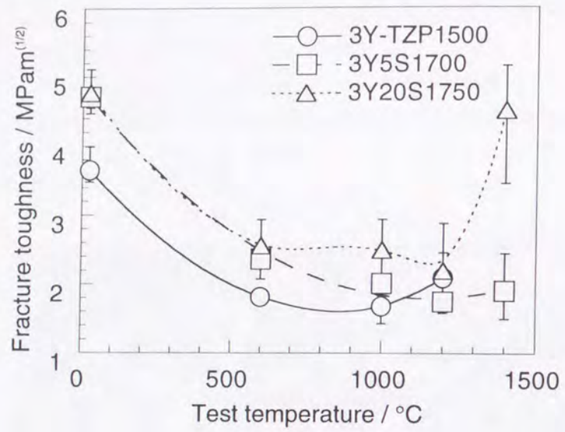

Fig. 4-8 The fracture toughness as a function of temperature for 3Y-TZP monolith sintered at 1500℃, 3Y-TZP/5 vol% SiC nanocomposite at 1700℃ and 3Y-TZP/20 vol% SiC at 1750℃.

4.4.2 8YSZ/SiC Nanocomposites

Fracture Strength

8YSZ monolith sintered at 1400°C (8YSZ1400), 8YSZ/5 and 20 vol% SiC nanocomposites hot-pressed at 1700°C and 1850°C (8Y5S1700 and 8Y20S1850) were used for measurements of high-temperature strength, which were exhibited the maximum strength in each composition at ambient temperature. Fig. 4-9 expresses the strength for 8YSZ monolith and 8YSZ/SiC nanocomposites as a function of temperature. The strength for monolith and composites slightly decreased with temperature. The strength for 8YSZ1400, 8Y5S1700 and 8Y20S1850 at 1000°C were 160 MPa, 380 MPa and 580 MPa, therefore decreasing rates of the strength from room temperature to 1000°C for 8YSZ1400, 8Y5S1700 and 8Y20S1850 were 46.7, 34.5 and 22.7 %. SiC dispersion obviously depressed the decrease in the strength at elevated temperatures. The decreasing rates for 8YSZ monolith and 8YSZ/SiC composites were smaller than that for 3Y-TZP1500, 3Y5S1700 and 3Y20S1750 which were 72.6, 62.4 and 52.3 %, because the strength for 8YSZ system is independent of the stress-induced transformation toughening. It is reported that the rapid degradation in the high-temperature strength is observed in other nanocomposite systems even though the strength for monolith gradually decreases[18], however, the rapid decrease does not occur in the 8YSZ/SiC nanocomposite system as shown in Fig. 4-9. The relationships between load and displacement at various temperatures for 8Y20S1850, and at 1000°C and 1400°C for monolith and composites are shown in Fig. 4-10 and Figs. 4-11 (a) and (b). Young's modulus

for both monolith and composites reduced with increasing test temperature, but the composites had higher Young's modulus than monolith. This higher Young's modulus for composites resulted in the higher strength than monolith. In addition, dynamic grain growth for 8YSZ monolith was confirmed during the measurements as shown in Figs. 4-12 (a) and (b). Fig. 4-12 is SEM images of fracture surface: (a) and (b) are 8YSZ1400 at room temperature and 1200°C in test temperature, (c) and (d) 8Y5S1700 at 1200°C and 1400°C and (e) and (f) are 8Y20S1850 at 1200°C and 1400°C. The grain growth observed in 8YSZ monolith should cause the decrease in the strength. On the other hand, grain growth during measurements for composites should be suppressed by SiC dispersion, thus the decrease in strength was smaller than monolith. Additionally, it is considered that the decrease in the strength for monolith is also attributed to the decrease in Young's modulus with increasing temperature and slow crack growth (SCG); a crack tends to propagate along weak grain boundaries due to high impurity concentration and lower melting point than 8YSZ grain.

From Fig. 4-11 (b), both composites exhibited plastic deformation at 1400°C, however, the 8Y20S1850 had larger displacement from yield to fracture than 8Y5S1700. The 8Y20S1850 seems to be deformation easily, even though its yield stress was higher than that for 8Y5S1700. On the other hand, the 8YSZ1400 showed brittle fracture even at 1400°C. The deformation mechanism greatly depends on grain size as mentioned above. The slip deformation by dislocation movements occurs easily when grain size is large, contrary to deformation by diffusional creep and grain boundary sliding becomes dominant with decreasing grain size. In this case, the grain size for both monolith and composites were above 1 μm, thus the diffusional creep should be dominant deformation mechanism. The diffusional creep rate is also enhanced by decreasing grain size, therefore, the plastic deformation was observed in order of 8Y20S1850, 8Y5S1700 and 8YSZ1400.

As shown in Fig. 4-12, both transgranular and grain boundary fracture modes were observed for monolith at ambient temperature (Fig. 4-12 (a)), fracture behavior turned to completely grain boundary fracture at elevated temperature around 1200°C (Fig. 4-12 (b)). The change from the grain boundary fracture to transgranular is usually attributed to strengthening the grain boundaries by SiC particles at grain boundaries. For 8Y20S1850, fracture behavior changed from transgranular at below 1200°C (Fig. 4-12 (e)) to grain boundary fracture at 1400°C (Fig. 4-12 (f)), while, for 8Y5S1700, transgranular fracture was demonstrated even at 1400°C (Fig. 4-12 (d)). The change of fracture mode for 8Y20S1850 should be related to the plastic deformation, because the deformation occurred at between 1200°C and 1400°C, and the SCG as well as monolith. The diffusional creep rate, which is mainly grain boundary mechanism, for 8Y20S1850 is higher than that for 8Y5S1700 as mentioned above, then, crack can be easily propagated along the grain boundary for 8Y20S1850 at 1400°C.

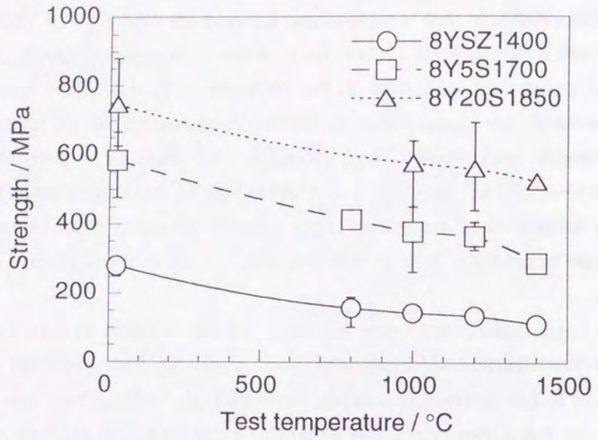

Fig. 4-9 The fracture strength as a function of temperature for 8YSZ monolith sintered at 1400℃, 8YSZ/5 vol% SiC nanocomposite at 1700℃ and 8YSZ/20 vol% SiC at 1850℃.

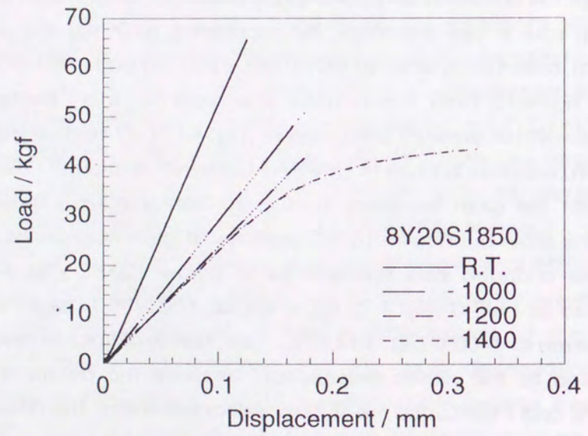

Fig. 4-10 The load/displacement at various temperatures for 8YSZ/20 vol% SiC nanocomposite sintered at 1850℃.

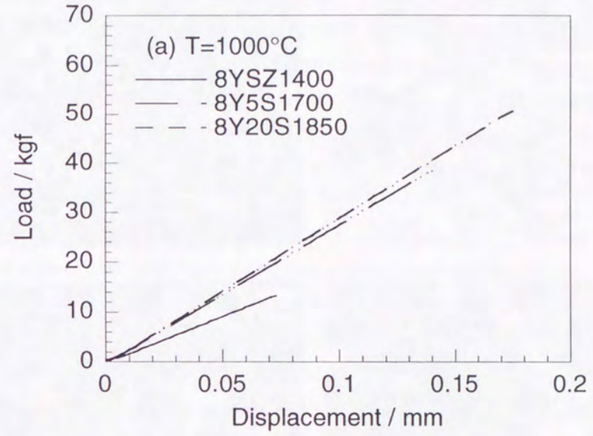

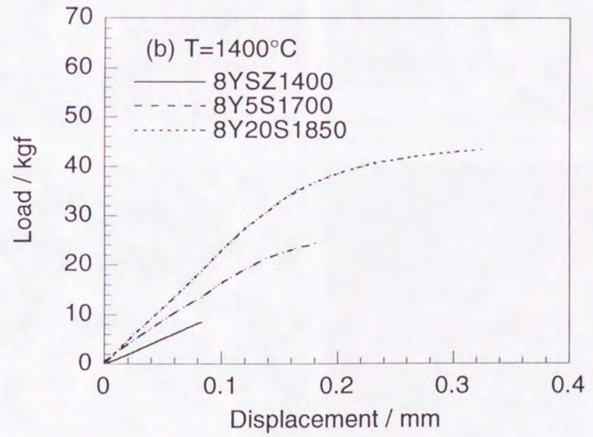

Fig. 4-11 The load/displacement at (a)1000℃ and (b)1400℃ for 8YSZ monolith sintered at 1400℃, 8YSZ/5 vol% SiC nanocomposite at 1700℃ and 8YSZ/20 vol% SiC at 1850℃.

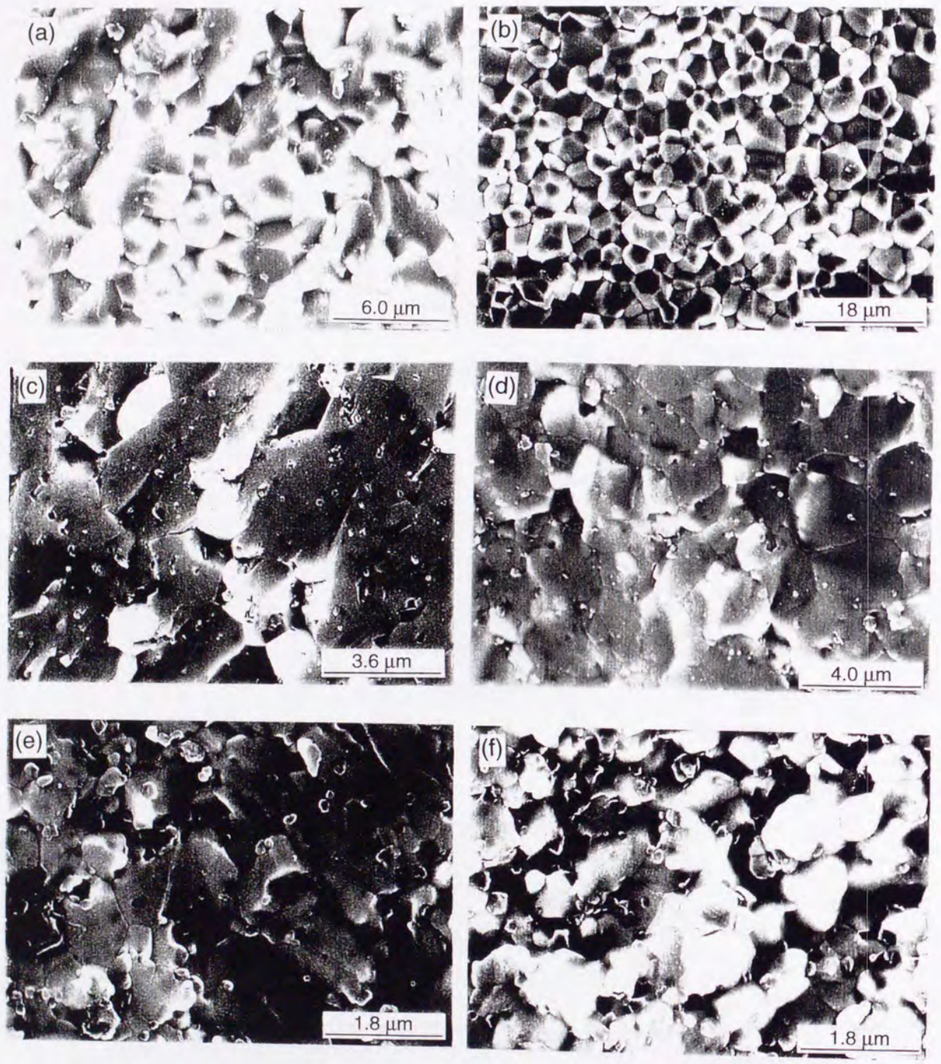

Fig. 4-12 SEM images of the fracture surfaces for (a) 8YSZ monolith at room temperature in test temperature, (b)8YSZ monolith at 1200℃, (c)8YSZ/5 vol% SiC nanocomposite at 1200℃, (d)8YSZ/5 vol% SiC at 1400℃, (e)8YSZ/20 vol% SiC at 1200℃ and (f)8YSZ/20 vol% SiC at 1400℃.

4.5 Conclusions

The high temperature mechanical properties for 3Y-TZP monolith, 3Y-TZP/SiC nanocomposites, 8YSZ monolith and 8YSZ/SiC composites were evaluated, and effects of nano-sized SiC particulate on mechanical properties and plastic deformation were investigated.

3Y-TZP/SiC nanocomposites

The high-temperature strength was slightly improved by incorporating SiC particulate. This should be due to the increase in Young's modulus and the toughness. Furthermore, plastic deformation was suppressed due to inhibition of grain boundary sliding by SiC particles at grain boundaries. On the other hand, the increase in the toughness should be attributed to the increase in Young's modulus, crack deflection and the residual stresses until the stresses were fully released.

8YSZ/SiC nanocomposites

The high-temperature strength for composites can be improved by dispersing SiC particulate. This improvement should be attributed to increase in Young's modulus, inhibition of dynamic grain growth of matrix and SCG. 8YSZ/20 vol% SiC nanocomposite had more than 500 MPa in strength at 1200°C without the rapid decrease in the strength, thus, this materials can be expected to be used as a new structure material at high temperatures such as Al_2O_3 or Si_3N_4.

References

1 M. Takaki, Mechanical properties of Y_2O_3-stabilized tetragonal ZrO_2 polycrystals after aging at high temperature, J. Am. Ceram. Soc., 39 [7](1986) 519-22

2 D. J. Green, R. H. J. Hannink and M. V. Swain, Transformation Toughening of Ceramics, CRC press, Inc., Boca Raton, Florida, USA, 1989, pp. 134-136.

3 A. D. Vasilev, S. A. Firstov, A. V. Shinkaruk, O. A. Babiy and A. V. Sameliuk, On the brittle-to ductile transition of Y-PSZ single crystals, J. Eur. Ceram. Soc., 16 (1996) 953-959.

4 G. A. Gogotsi, E. E. Lomonova and V. G. Pejchev, Strength and fracture toughness of zirconia crystals, J. Eur. Ceram. Soc., 11 (1993) 123-132.

5 N. Claussen, K. -L. Weisskopf and M. Rühle, Tetragonal zirconia polycrystals reinforced with SiC whiskers, J. Am. Ceram. Soc., 69 [3](1986) 288-292.

6 J. Hong, L. Gao, B. A. Shaw and D. P. Thompson, SiC platelet and SiC platelet-alunima reinforced TZP matrix composites, Br. Ceram. Trans., 94 [5](1995) 201-204.

7 S. Hong, L. Gao, X. X. Huang, A. Shaw and D. P. Thompson, Silicon carbide-toughened zirconia ceramics, J. Mater. Sci., 31 (1996) 957-962.

8 K. Tsukuma, T. Takahata and M. Shiomi, Strength and fracture toughness of Y-TZP, Ce-TZP, Y-TZP/Al_2O_3, and Ce-TZP/Al_2O_3, in Advances in Ceramics, vol. 24, Science and Technology of Zirconia III, Eds. by S. Somiya, N. Yamamoto and H. Yanagida, Am. Ceram. Soc., Columbus, Ohio, 1988, pp. 721-728.

9 K. Niihara, A. Nakahira, T. Uchiyama and T. Hirai, High-temperature mechanical properties of Al_2O_3-SiC composites, in Fracture Mechanics of Ceramics, vol. 7, Eds. by R. Bradt, A. G. Evans, D. P. H. Hasselman and F. F. Lange, Plenum Press, New York, 1986, pp. 103-116.

10 T. Ohji, A. Nakahira, T. Hirano and K. Niihara, Tensile creep behavior of alumina/silicon carbide

nanocomposite, J. Am. Ceram, Soc., 77 [12](1994) 3259-3262.
11 T. Ohji, T. Hirano, A. Nakahira and K. Niihara, Particle/matrix interface and its role in creep inhibition in alumina/silicon carbide nanocomposites, J. Am. Ceram. Soc., 79 [1](1996) 33-45.
12 K. Yasuda, Q. Bao and K. Niihara, The effects of fine SiC particles on the creep of MgO at high temperatures, J. Ceram. Soc. Jpn., 100 [4](1992) 514-519.
13 Y. Okamoto and T. Nishida, Advanced ceramics, Eds. by N. Ichinose, Y. Matsuo, H. Abe and Y. Matsuo, Ceram. Soc. Jpn., Ohmu-sha, 1991, pp. 160-177.
14 W. D. Kingery, H. K. Bowen and D. R. Uhlmann, Introduction to ceramics, 2nd Ed., JOHN WILEY & SONS, NY, 1976, pp. 737-739.
15 W. D. Kingery, H. K. Bowen and D. R. Uhlmann, Introduction to ceramics, 2nd Ed., JOHN WILEY & SONS, NY, 1976, pp. 739-742.
16 W. D. Kingery, H. K. Bowen and D. R. Uhlmann, Introduction to ceramics, 2nd Ed., JOHN WILEY & SONS, NY, 1976, p. 742.
17 T. Nose, T. Fujii, Evaluation of fracture toughness for ceramic materials by single-edge-precracked-beam method, J. Am. Ceram. Soc., 71 [5](1988) 328-333.
18 K. Niihara, New design concept of structural ceramics -ceramic nanocomposites-, J. Ceram. Soc. Jpn., 99 [10](1991) 974-982.

5 Ionic Conductivity for 8YSZ/SiC Composites

5.1 Introduction

Yttria stabilized zirconia (YSZ) is a representative solid electrolyte in solid oxide fuel cell (SOFC) materials because of its low electronic and high oxygen ion conductivity[1]. Instead of its excellent electrical properties, YSZ possesses low mechanical properties, for instance, 300 MPa in fracture strength. Various Al_2O_3 particles dispersed composites have been investigated to improve the poor mechanical property for YSZ[2,3,4,5,6]. Al_2O_3 is an insulator and has superior thermal conductivity and mechanical property even at high temperatures[7], compared with 8 mol% Y_2O_3 stabilized zirconia (8YSZ). Besides, Al_2O_3 dispersed tetragonal zirconia polycrystal (TZP) has the highest strength among the ZrO_2 based ceramics[8]. It has been reported that the mechanical properties of Al_2O_3 dispersed YSZ were improved, for instance, the strength improved up to 470 MPa by adding 30 vol% Al_2O_3[4]. On the other hand, for ionic conductivity of those composites, some researchers insisted that the ionic conductivity decreased with increasing Al_2O_3 content[2,3], the others reported beneficial effects of Al_2O_3 addition on the conductivity[5,6]. In this work, SiC particulate which is semiconductive material and has excellent mechanical properties was selected as a second phase dispersion. The strength at ambient temperature was remarkably improved to 750 MPa by dispersing 20 vol% SiC particles. Furthermore, the strength of about 600 MPa was achieved even at 1000°C as described in Chapters 3 and 4.

In this chapter, special emphasis was placed on understanding of the effect of fine SiC dispersion on ionic conductivity of 8YSZ. The influence on the conductivity associated with the different size of dispersed SiC was also investigated.

5.2 Experimental Procedure

Specimens for impedance measurement were machined into platelets (≈ 5 x 5 x 0.3 - 0.6 mm). The characteristic of the specimens used was shown in Table 5-1. Details of characteristic of starting powders, fabrication procedure and microstructure for the specimens were demonstrated in Chapter 2, and their mechanical properties were shown in Chapter 3.

Impedance measurement was carried out for a frequency range of 20 Hz to 1 MHz on the platelet specimens with Ag paste electrodes during cooling process from 802°C to 200°C in Ar. The ionic resistance was obtained by complex impedance plot from impedance, Z, and the phase angle, θ. Grain boundary, lattice and total conductivity, σ, were calculated by the Eq. 5-1, where the each resistance (i.e., grain boundary, lattice and

total), R, was determined as a diameter of each circle appeared in the complex impedance plot (Fig. 5-1), t is the thickness of each specimen, and s is the surface area of an electrode.

$$\sigma = \frac{1}{R \times s/t} \qquad (5\text{-}1)$$

Table 5-1 Characteristic of the specimens for impedance measurement.

	SiC / vol%	S.T.*1 / ℃	R.D.*2 / %	grain size / μm	strength / MPa
8YSZ1400	0	1400	99.3	7.0	298
8YSZ1600	0	1600	99.9	22.7	194
8Y5S1700	5	1700	100	2.6	584
8Y20S1850	20	1850	100	1.0	747
8Y5SM1700	5	1700	100	5.0	446
8Y20SM1850	20	1850	100	-*3	547

*1 : Sintering temperature.
*2 : Relative density.
*3 : Difficult to measure. 8Y20SM1800 has 2.6 μm in rain size as a reference.

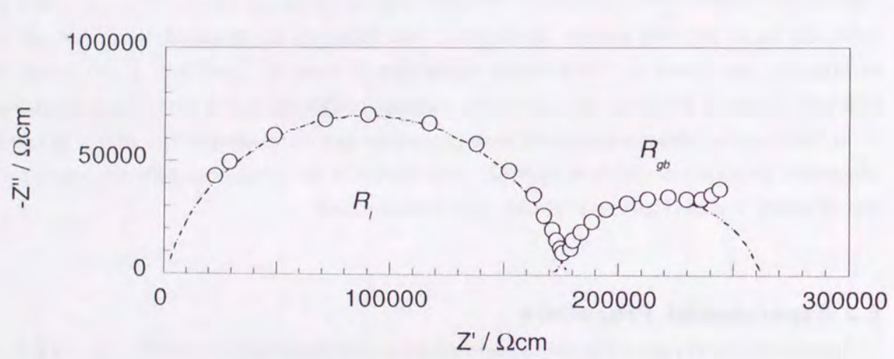

Fig. 5-1 Typical complex impedance plot for polycrystalline 8YSZ by impedance analysis. R_i, is associated with the lattice resistance, R_g, is attributed to the grain boundary resistance.

5.3 Results

The ionic conductivity was measured for 8YSZ monolith sintered at 1400°C (denoted by 8YSZ1400), 8YSZ/5 vol% SiC nanocomposite at 1700°C (8Y5S1700) and 20 vol% SiC at 1850°C (8Y20S1850) which displayed the maximum strength in each composition. The measurement was carried out for the monolith hot-pressed at 1600°C (8YSZ1600) to clarify

the effect of matrix grain size on ionic conductivity. The characteristic of each sample is shown in Table 5-1. In order to confirm the effects of nano-sized SiC dispersion, ionic conductivity was measured for 5 and 20 vol% micro-sized SiC (1.2 μm in particle size) dispersed 8YSZ sintered at 1700°C and 1850°C (8Y5SM1700 and 8Y20SM1850).

Fig. 5-1 shows a typical complex impedance plot obtained by the frequency -response analysis in this work, where the left-side arc is associated with the lattice resistance, R_i, and the second one from the left is attributed to the grain boundary resistance, R_g. Total resistance of the electrolyte, R_t, is consisted from R_i and R_g. Third arc from the left, which can not be observed clearly in this figure, depends on the resistance of electrode and/or interface between electrode and electrolyte, R_e. All arcs might be overlapped. The degree of the overlap depends on the difference of relaxation time of the conduction processes and the cell geometry[9].

SiC is a semiconductor material, however, effect of electrical conductivity of SiC might be negligible in this measurement, because each SiC particle was isolated in matrix grain and/or at grain boundaries as shown in Fig. 5-2. If SiC affects the conductivity, the conductivity for composites will become much higher than that for the monolith, since the electric resistance for SiC is 107 x 10^{-6} Ωcm at room temperature[10]. Followed detailed result will be described for 8YSZ/SiC nano- and microcomposites.

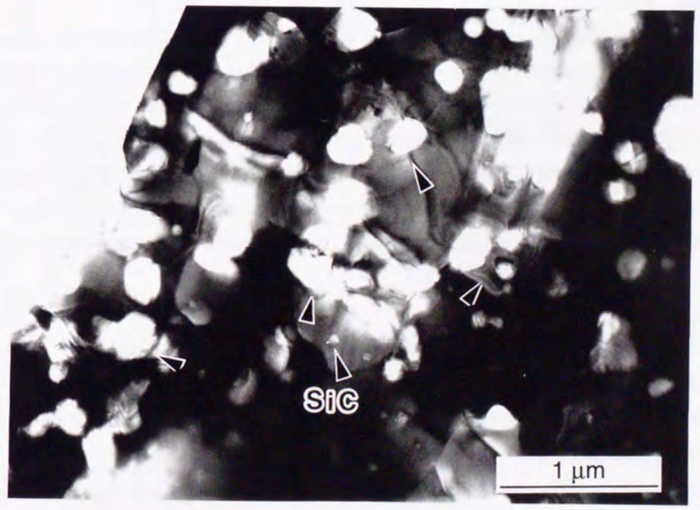

Fig. 5-2 TEM image for 8YSZ/20 vol% SiC nanocomposite sintered at 1850°C. Each SiC particle is well dispersed at grain boundary and within matrix grains and isolated.

5.3.1 Nanocomposites

Grain boundary conductivity

Temperature dependence of the grain boundary conductivity for 8YSZ monoliths and 8YSZ/SiC nanocomposites is shown in Fig. 5-3. The conductivity obviously decreased in order of 8YSZ1600, 8YSZ1400, 8Y5S1700 and 8Y20S1850. The depression of the grain boundary conductivity increased with increasing SiC content. As shown in Fig. 5-3, some difference were observed in not only composites, 8Y5S1700 and 8Y20S1850, but also monoliths, 8YSZ1400 and 8YSZ1600. The activation energy, *E*, of grain boundary conductivity for each specimen is shown in Table 5-2, which was calculated from the slop in Fig. 5-3 based on the relationship as expressed by Eq. (5-2),

$$\sigma T = A\exp(-E / RT) \qquad (5\text{-}2)$$

where, σ, *T*, *A*, and *R* are conductivity, absolute temperature, constant and gas constant, respectively. The activation energy for grain boundary conductivity increased with decreasing the conductivity, which indicated that oxygen ion with low activation energy can move easily even at low temperature. Activation energies of the composites were low compared with those of monoliths. Furthermore 8YSZ1400 had higher activation energy than 8YSZ1600, the difference between 8YSZ1400 and 8YSZ1600 was also reconfirmed in Fig. 5-3.

Lattice conductivity

The lattice ionic conductivity and the activation energy for 8YSZ1400, 8YSZ1600, 8Y5S1700 and 8Y20S1850 are described in Fig. 5-4 and Table 5-2. The lattice conductivity for 8YSZ1400 and 8YSZ1600 seems to be almost same. 8Y5S1700 also had similar conductivity with both monoliths, in spite of incorporating SiC particulate, and activation energies of 8YSZ1400 and 8Y5S1700 were almost same. However, the conductivity for 8Y20S1850 was superior to the others, especially at low temperature. This phenomenon is reflected in the activation energy. The activation energy for 8Y20S1850 is much smaller than the others.

Total conductivity

Total conductivity for both 8YSZ monoliths, 8Y5S1700 and 8Y20S1850 are shown in Fig. 5-5. The conductivity decreased in order of 8YSZ1600, 8YSZ1400, 8Y5S1700 and 8Y20S1850, which is analogous to the grain boundary conductivity. The lower conductivity, grain boundary or lattice conductivity, governs the total conductivity. Thus the total conductivity for composites seems to be dominated by the grain boundary conductivity, while for monolith by lattice conductivity. Therefore the difference of total conductivity between composites and monolith was reduced, even though the total conductivity for composites was lower than monolith.

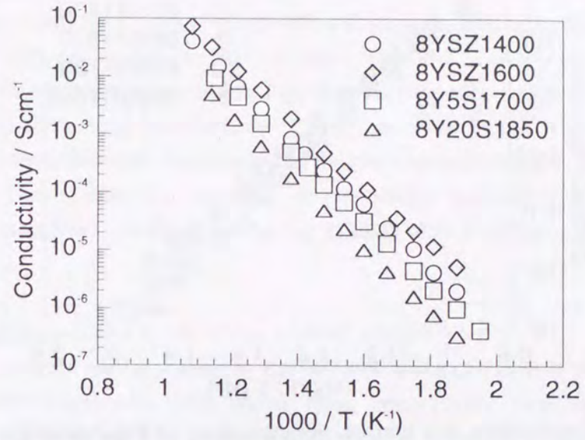

Fig. 5-3 The grain boundary conductivity as a function of temperature for 8YSZ monoliths sintered at 1400°C and 1600°C, 8YSZ/5 vol% SiC nanocomposite sintered at 1700°C (8Y5S1700) and 8YSZ/20 vol% SiC at 1850°C (8Y20S1850).

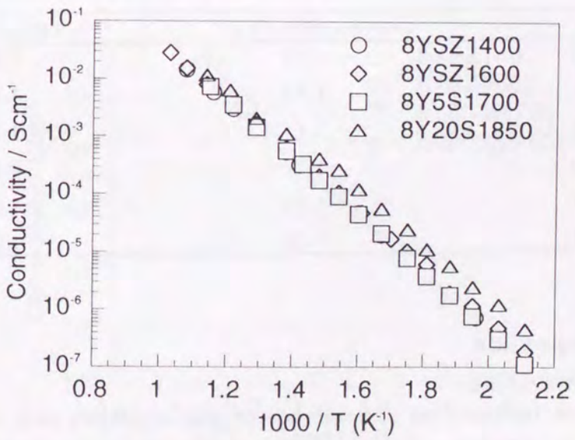

Fig. 5-4 The temperature dependence of lattice conductivity for 8YSZ monoliths sintered at 1400°C and 1600°C, 8YSZ/5 vol% SiC nanocomposite sintered at 1700°C (8Y5S1700) and 8YSZ/20 vol% SiC at 1850°C (8Y20S1850).

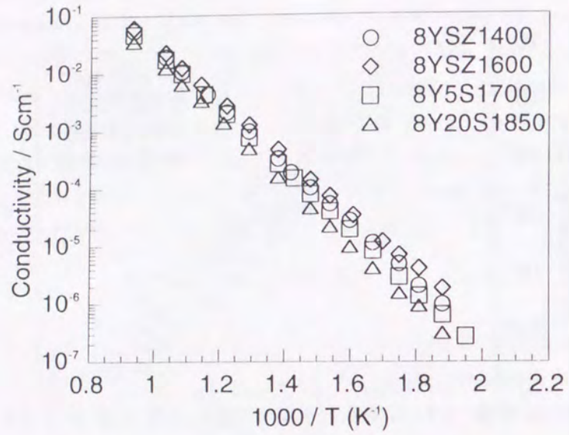

Fig. 5-5 Total conductivity as a function of temperature for 8YSZ monoliths sintered at 1400°C and 1600°C, 8YSZ/5 vol% SiC nanocomposite sintered at 1700°C (8Y5S1700) and 8YSZ/20 vol% SiC at 1850°C (8Y20S1850).

Table 5-2 Activation energy of grain boundary and lattice conductivity for the each specimen.

	Grain boundary / eV	Lattice / eV
8YSZ1400	1.12	1.03
8YSZ1600	1.10	1.01
8Y5S1700	1.14	1.04
8Y20S1850	1.17	0.95
8Y5SM1700	1.14	1.05
8Y20SM1850	1.13	1.09

5.3.2 Microcomposites

Grain boundary conductivity

Fig. 5-6 shows the temperature dependence of grain boundary ionic conductivity for 8YSZ monoliths and 8YSZ/SiC microcomposites, 8Y5SM1700 and 8Y20SM1850. The conductivity for monoliths is as same as represented in Fig. 5-3. The conductivity decreased in order of monoliths, 8Y5SM1700 and 8Y20SM1850 as well as nanocomposite. The difference of the conductivity between monoliths and microcomposites, however, was smaller than that between monoliths and nanocomposites. The activation energy for

microcomposites is also indicated in Table 5-2. The activation energy for microcomposites were similar to 8YSZ1400, and the deference from 8YSZ1600 was also small.

Lattice conductivity

The lattice conductivity and the activation energy for 8YSZ1400, 8YSZ1600, 8Y5SM1700 and 8Y20SM1850 are shown in Fig. 5-7 and Table 5-2. At lower temperatures, the conductivity for 8Y5SM1700 was lower than that for monolith, which was similar to that for 8YSZ1400 with increasing temperature. On the other hand, 8Y20SM1850 had low conductivity compared with the others, and this phenomenon is against to nanocomposite, 8Y20S1850. The specimens showed almost similar activation energy except for 8Y20SM1850, and the activation energy for 8Y20SM1850 was higher than monoliths and 8Y5SM1700.

Total conductivity

The total conductivity for monoliths, 8Y5SM1700 and 8Y20SM1850 was indicated in Fig. 5-8. The microcomposites had lower total conductivity than monoliths, and the conductivity also reduced with increasing SiC content as same as nanocomposites.

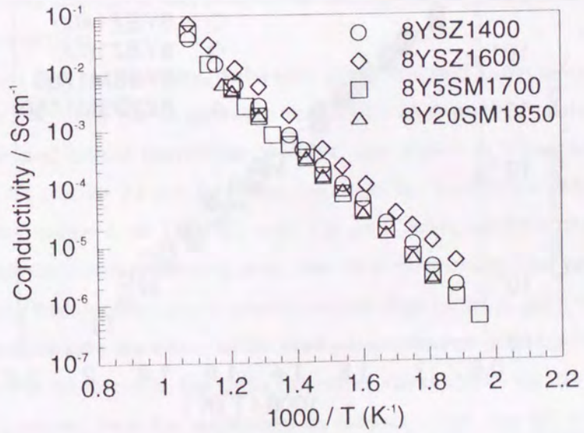

Fig. 5-6 The grain boundary conductivity as a function of temperature for 8YSZ monoliths sintered at 1400°C and 1600°C, 8YSZ/5 vol% SiC microcomposite sintered at 1700°C (8Y5SM1700) and 8YSZ/20 vol% SiC at 1850°C (8Y20SM1850).

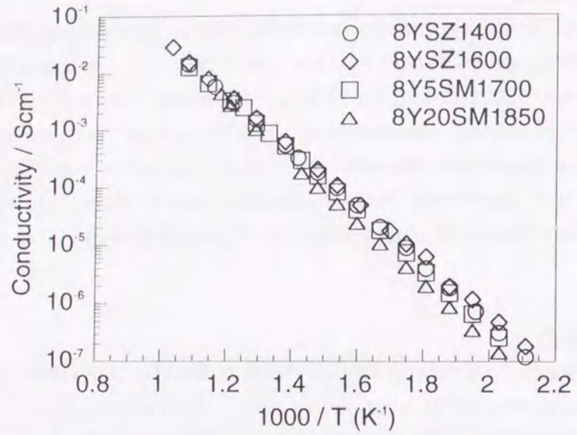

Fig. 5-7 The lattice conductivity as a function of temperature for 8YSZ monoliths sintered at 1400°C and 1600°C, 8YSZ/5 vol% SiC microcomposite sintered at 1700°C (8Y5SM1700) and 8YSZ/20 vol% SiC at 1850°C (8Y20SM1850).

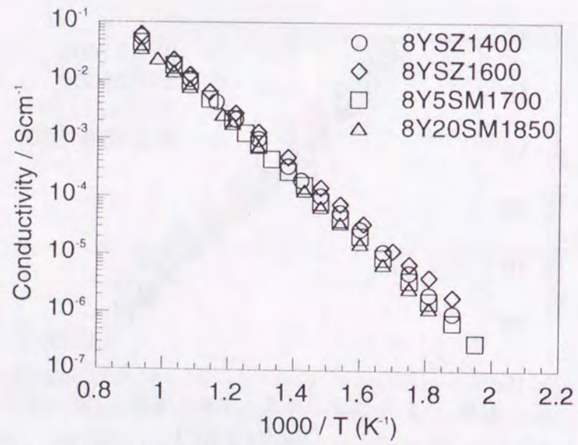

Fig. 5-8 The total conductivity as a function of temperature for 8YSZ monoliths sintered at 1400°C and 1600°C, 8YSZ/5 vol% SiC microcomposite sintered at 1700°C (8Y5SM1700) and 8YSZ/20 vol% SiC at 1850°C (8Y20SM1850).

5.4 Discussions

5.4.1 Grain Boundary Ionic Conductivity

As described in Figs. 5-3 and 5-6, some difference in grain boundary conductivity can be observed not only composites but also monoliths. In general, the grain boundary conductivity (resistance) of polycrystalline depends on its microstructure such as density and grain size. The grain boundary conductivity increases with increasing density[11]. The conductivity increases with increasing matrix grain size, hence, the resistance decreases with increasing grain size because of the decrease in the grain boundary length or area[12]. In addition, according to Badwal et al.[12], the nature and morphology of the grain boundary influence on the resistance. In detail, the nature of the grain boundary phase drastically changed at 1400°C to 1500°C for 10 mol% Y_2O_3 doped ZrO_2. The grain boundary phase such as glassy phase, which was originated by an impurity, uniformly coated grains when sintering temperature was low (i.e., 1400°C). While above 1500°C in sintering temperature, the grain boundary became cleaner, because the glassy phase become less viscous and squeezes out into triple point. In the present work, it is still unclear how the morphology and nature of the grain boundary affect the grain boundary conductivity. On the other hand, the grain boundary length should have some effects on the resistance, from the results that the grain size for 8YSZ1600 was much larger than that for 8YSZ1400 as shown in Table 5-1. All specimens, however, were fully densified as shown in Table 5-1, the influence of density should be less even if the density affects the conductivity, compared with effects of grain size.

Fig. 5-9 shows the relationships between grain size and grain boundary and lattice resistance at 402°C. The mean grain size for 8Y20SM1850 can not obtained, therefore its grain boundary and lattice resistance at 402°C are shown in Table 5-3. The grain size, however, must be above 2.6 μm, because the grain size for 8Y20SM1800 (8YSZ/20 vol% SiC microcomposites sintered at 1800°C) was 2.6 μm. From Fig. 5-9, the grain boundary resistance decreased with increasing grain size, thus composites had high grain boundary resistance due to fine microstructure associated by dispersing SiC particulate. In addition to grain boundary length, the effect of SiC particles located at grain boundary is considered as a reason for the decrease in the grain boundary conductivity for the composites. The effects of SiC particles may be explained as follows. First, the SiC particles cause the process of conduction through the boundaries to be partially blocked, as well as the case that the pore block the conduction when the density is low. Second, it is the decrease in the effective volume of grain boundary as conductive path by substitution of SiC at the

boundary for 8YSZ. These effects are proportional to volume of SiC particulate exists at grain boundaries. The content of SiC particles located at grain boundaries essentially increases with the increase in SiC volume fraction for 8YSZ and size of SiC particles. Furthermore, as mentioned for densification and grain growth in Chapter 2, the decrease in grain boundary diffusivity at the interface between 8YSZ matrix and SiC dispersion may influence on the decrease in grain boundary conductivity. Therefore grain boundary resistance for 20 vol% SiC composites with finer microstructure greatly increased, compared with 5 vol% SiC composites.

Consequently, fine microstructure by SiC dispersion and SiC particles at the grain boundary should cause the decrease in the grain boundary conductivity.

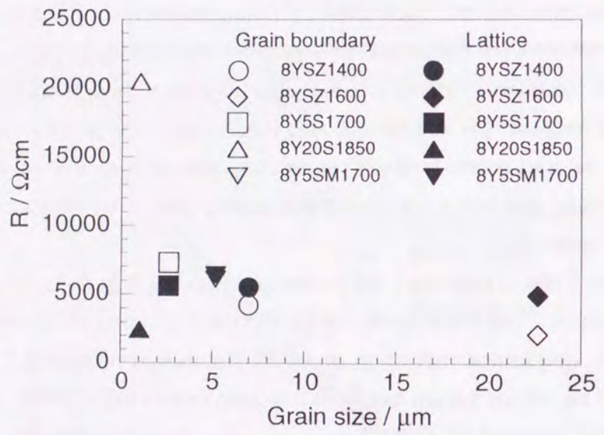

Fig. 5-9 The relationship between mean grain size and grain boundary and lattice resistance at 402°C for 8YSZ1400, 8YSZ1600, 8Y5S1700, 8Y20S1850 and 8Y5SM1700. Open symbols and solid symbols indicate the grain boundary and lattice resistance, respectively.

Table 5-3 Grain boundary and lattice resistance for 8Y20SM1850 at 402℃.

	Grain boundary / Ωcm	Lattice / Ωcm
8Y20SM1850	14207	7454

5.4.2 Lattice Ionic Conductivity

From Fig. 5-9 which shows the lattice resistance at 402°C as a function of grain size, 8YSZ1400 and 8YSZ1600 have similar resistance. Thus, it is obvious that the lattice conductivity does not depend on grain size. This result shows good agreement with the results obtained by Badwal et al.[12], in which the grain size made no effects on the lattice resistance, contrary to grain boundary resistance.

In Fig. 5-9, it can be observed that the resistance for 8Y5SM1700 is higher than that of 8Y5S1700 which has similar resistance to monoliths. Fig. 5-10 describes the lattice conductivity for 20 vol% SiC micro- and nanocomposites in order to compare both composites. The obvious difference can be detected in micro- and nanocomposites, and the difference can be confirmed also in activation energy as shown in Table 5-2. Nanocomposites clearly had higher lattice conductivity and lower activation energy than monolith, while microcomposites had lower conductivity and higher activation energy. As mentioned above, grain size makes no effect on the lattice conductivity, therefore other factors appear to be depended on the conductivity. Generally, in oxides stabilized ZrO_2, the temperature dependence of conductivity depends on the diffusion coefficient of oxygen ion, which is varied by a temperature fixed solely by the activation energy required for oxygen ion mobility[13]. The increase for 8Y20S1850 and decrease for 8Y20SM1850 in the lattice conductivity corresponds to the increase and decrease of oxygen ion diffusion coefficient by adding SiC particulate, respectively. The reasons why the difference of the oxygen diffusion coefficient in lattice generated between micro- and nanocomposites are explained by uniform and nonuniform strain as mentioned in Chapter 2.

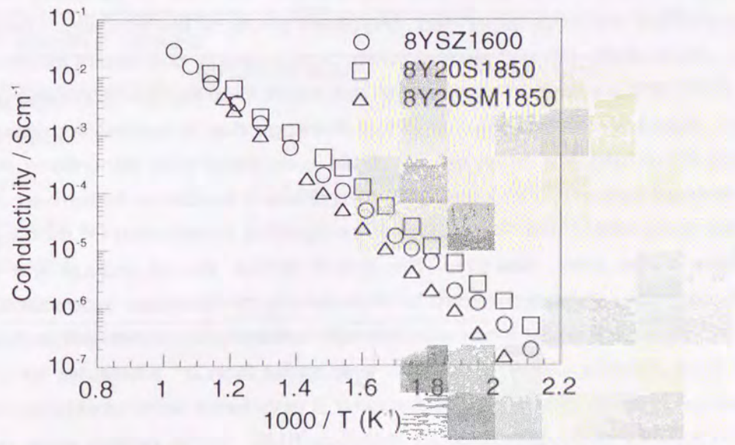

Fig. 5-10 The temperature dependence of lattice conductivity for 8YSZ1600, 8Y20S1850 and 8Y20SM1850.

Firstly, the reason why nanocomposites have higher lattice conductivity is discussed. In the 8YSZ/SiC composite cases, tensile and compressive uniform stresses due to the coefficient of thermal expansion (CTE) mismatch between the 8YSZ and SiC act on the 8YSZ matrix and SiC particulate, respectively, as shown in Table 2-3. This tensile uniform stress acting on matrix increases with increasing SiC content and a number of SiC particles within matrix grains as mentioned in Chapter 2. It introduces strain and expands of the matrix lattice. The lattice expansion can make oxygen ion (O^{2-}) movement more easily within the lattice, because the distance between zirconium ions (Zr^{4+}) or Zr^{4+} and Y'_{Zr} which indicates yttrium ion (Y^{3+}) substituted for Zr^{4+} and has a negative electric charge extends. Besides Coulomb's force that O^{2-} suffers from Zr^{4+} and/or oxygen vacancy (Vö) is attracted from Y'_{Zr} decreases due to the elongation of distance between O^{2-} and Zr^{4+} and Vö and Y'_{Zr} by lattice expansion.

On the contrary, 8Y20SM1850 exhibited a negative effect of SiC dispersion on lattice conductivity, in spite of having uniform strain as well as nanocomposites. Its uniform strain is, however, less than nanocomposite, because nanocomposite incorporating a lot of SiC particles within matrix grains possessed higher uniform stress depending on CTE mismatch than microcomposite possessing SiC particles at grain boundary. From now, the negative effect of SiC dispersion on lattice conductivity is discussed. Nonuniform and uniform strains are listed in Table 5-4. Nonuniform strain is a experimental value, while uniform one is estimated from uniform stress in Table 2-3. In fact, the uniform strain for nanocomposites must be less than the values in Table 5-4 and the real strain should be between the values estimated for nano- and microcomposites, because SiC particles located both within matrix grains and at grain boundary as shown in Figs. 2-13 (b) and 5-2. In microcomposite, most of SiC particles located at grain boundaries, which enhance to generate nonuniform strain. Some lattice should be expanded, and others shrunk by the nonuniform stress. Compared nonuniform strain with uniform strain in each composition, both strains for composites except for 8Y20S1850 are almost in similar level, and then lattice expansion in some grains by uniform strain should be canceled by the lattice shrinkage due to nonuniform strain. On the other hand, 8Y20S1850 has large uniform strain compared with nonuniform strain. Thus it is considered that 8Y20S1850 demonstrated different tendency for lattice conductivity from other composites. The expanded lattice appears to enhance O^{2-} mobility as well as the uniform strain case, however, the shrunk lattice should reduce the mobility. This phenomenon can be considered to analogous to the decrease in conductivity when some metal oxide with larger ionic radius than Zr^{4+} forms a solid solution with ZrO_2 as shown in Fig. 5-11[14]. When a cation with larger ionic radius than Zr^{4+} substitutes for Zr^{4+}, large lattice strain generates. Since oxygen vacancy is associated with substitution ion to relief the strain, mobility of oxygen vacancy is reduced[14]. In the present work, association may occur between Vö and Y'_{Zr}, because the distance between Vö and Y'_{Zr} is shorten in shrunk

lattice and compressive stress and strain imposed lattice. Thus Vö mobility decreases in shrunk lattice. The reduced Vö mobility in shrunk lattice may be rate-limiting of ionic conduction, thus whole lattice conductivity decreased in 8Y20SM1850 possessing high nonuniform strain, even though uniform tensile strain existed in matrix.

Hence, nonuniform strain should cause decrease in lattice conductivity, while uniform tensile strain realizes the improvement in lattice conductivity. The lattice conductivity for each material should be varied by the balance of uniform and nonuniform strains. The difference of the lattice conductivity between 8Y5S1700 and 8Y20S1850 would be due to the difference of the amount of uniform and nonuniform strains.

Consequently, nanocomposite system exhibits a good effect on the lattice conductivity by the uniform stress induced by the CTE mismatch between matrix and second phase. Nanocomposite technique has a possibility to increase the total ionic conductivity of 8YSZ, when large uniform stress can be obtained with low second phase content, and most of the dispersion can be located within matrix grains. Furthermore, the decrease in the grain boundary conductivity can be depressed and lattice conductivity should be improved, if lots of second phase are dispersed within exaggerated 8YSZ matrix grains. In those composites consisted from exaggerate grains incorporating fine second phase, dislocations, which are generated in matrix grains by the compressive uniform stresses imposing SiC particles form sub-grain boundaries as illustrated in Fig. 5-12. This phenomenon has already reported for Al_2O_3/SiC nanocomposites consisted large grain with sub-grain boundaries, which possesses high strength even though grain size is over 20 μm[15]. That is, it has a possibility to fabricate the composites having high total conductivity and high strength.

Table 5-4 Nonuniform strains measured by XRD and theoretical uniform strains calculated from uniform stresses in Table 2-3.

	Nonuniform strain	Uniform strain*
8YSZ1400	0	0
8YSZ1600	0	0
8Y5S1700	1.6×10^{-4}	3.9×10^{-4}
8Y20S1850	5.8×10^{-4}	14.1×10^{-4}
8Y5SM1700	3.1×10^{-4}	2.8×10^{-4}
8Y20SM1850	9.0×10^{-4}	10.0×10^{-4}

*Uniform strain, σ_t, is derived from theoretical uniform stress, σ_t, and Young's modulus, E.

$$\varepsilon = \sigma_t \times E \qquad (5\text{-}3)$$

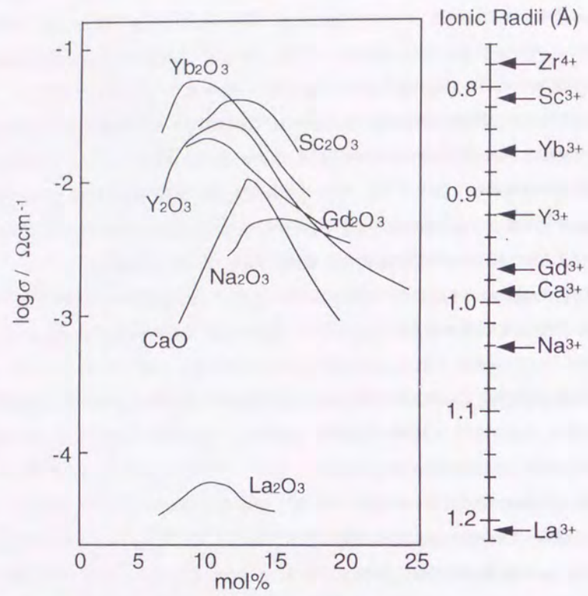

Fig. 5-11 The ionic conductivity of ZrO_2 stabilized with different oxides at 800°C, and ionic radii of dopant cations.

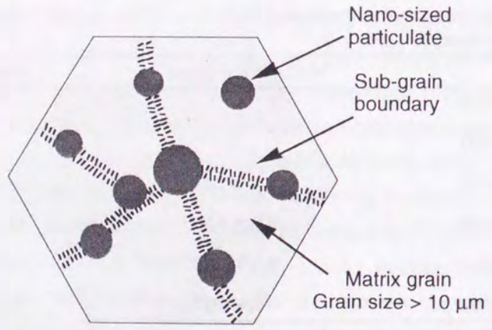

Fig. 5-12 Schematic illustration of sub-grain boundary.

5.5 Conclusions

The ionic conductivity was measured for 8YSZ monoliths and 8YSZ/SiC nano- and microcomposites. The effects of SiC particles on grain boundary and lattice conductivity was investigated and summarized as follows.

Fine microstructure by dispersing SiC particles and SiC particles at grain boundary caused the decrease in the grain boundary conductivity, while nanocomposite system exhibited a good lattice conductivity because of the residual stress induced by the CTE mismatch between matrix and dispersion. Finer second phase dispersed 8YSZ composites have a possibility to possess not only high ionic conductivity, but also high fracture strength.

References

1 N. Q. Minh, Ceramic fuel cells, J. Am. Ceram. Soc., 76 [3](1993) 563-588.

2 M. Mori, T. Abe, H. Itoh, O. Yamamoto, T. Takeda and T. Kawahara, Cubic-stabilized zirconia and alumina composites as electrolytes in planar type solid oxide fuel cells, Solid State Ionics, 74 (1994) 157-164.

3 S Terauch, H. Takizawa, T. Endo and M. Shimada, Ionic conductivity and mechanical properties of post-HIPed cubic zirconia/alumina composites, Materials and Manufacturing Processes, 9 [5](1994) 965-974.

4 K. Oe, K. Kikkawa, A. Kishimoto, Y. Nakamura and H. Yanagida, Toughening of ionic conductive zirconia ceramics utilizing a nonlinear effect, Solid State Ionics, 91 (1996) 131-136.

5 R. C. Buchanan and D. M. Wilson, in Advances in Ceramics, vol. 10, Ed. by W. D. Kingery, Am. Ceram. Soc., Columbus, Ohio, 1983, pp. 526-540.

6 J. Drennan and S. P. S. Badwal, in Advances in Ceramics, vol. 24, Science and Technology of Zirconia III, Eds. by S. Somiya, N. Yamamoto and H. Yanagida, Am. Ceram. Soc., Columbus, Ohio, 1988, pp. 807-817.

7 Cyclopedia of Fine Ceramics (in Jpn), Eds. by H. Yanagida et al., Gihodo Press, Tokyo, 1987, pp. 30-49.

8 K. Tsukuma, T. Takahata and M. Shiomi, Strength and fracture toughness of Y-TZP, Ce-TZP, Y-TZP/Al_2O_3, and Ce-TZP/Al_2O_3, in Advances in Ceramics, vol. 24, Science and Technology of Zirconia III, Eds. by S. Somiya, N. Yamamoto and H. Yanagida, Am. Ceram. Soc., Columbus, Ohio, 1988, pp. 721-728.

9 A. Kishimoto, Measurements of ionic conductivity and electron conductivity, DENKI KAGAKU, 61 [11](1993) 1264-1268.

10 Rikagaku Jiten (in Jpn), 4th Ed., Eds. by R. kubo, S. Nagakura, H. Iguchi and H. Esawa, Iwanami Shoten, Tokyo, 1987, pp. 755-756.

11 M. C. Steil, F. Thevenot and M. Kleits, Densification of yttria-stabilized zirconia impedance spectroscopy analysis, J. Electrochem. Soc., 144 [1](1997) 390-398.

12 S. P. S. Badwal and J. Drennan, Yttria-zirconia: effect of microstructure on conductivity, J. Mater. Sci., 22 (1987) 3231-3239.

13 W. D. Kingery, H. K. Bowen and D. R. Uhlmann, Introduction to Ceramics, 2nd Ed., John Wiley & Sons, New York, 1976, p. 239.

14 Y. Saito, Electrical conduction of stabilized zirconia and oxygen sensor, in Zirconia Ceramics, vol. 1, Uchida Rokakuho Publishing Co., Ltd., Tokyo, 1983, pp. 109-125.

15 K. Niihara, New design concept of structural ceramics -ceramic nanocomposites-, J. Ceram. Soc. Jpn, 99 [10](1991) 974-982.

6 Summary

In this study, the improvements in high-temperature strength for 3Y-TZP and the mechanical properties for 8YSZ were attempted by using the nanocomposite technique which is valuable to strengthening and toughening. The effects of nano-sized SiC dispersion on the microstructure and the mechanical properties for 3Y-TZP and 8YSZ were investigated. For 3Y-TZP, the effects of SiC particles on the transformation was also studied. Moreover, for 8YSZ, the SiC effect on the ionic conductivity was discussed. To investigate nano-sized SiC particles, some kinds of micro-sized SiC particles dispersed microcomposites were fabricated and their mechanical properties were evaluated. Major conclusions in this study are summarized below.

In Chapter 2, the difference of densification and grain growth between 3Y-TZP and 8YSZ monoliths and the effects of SiC particulate on densification, grain growth and residual stresses/strains were discussed.

Dominant mechanism of densification and grain growth were different between 3Y-TZP and 8YSZ; that for 3Y-TZP was lattice diffusion, and that for 8YSZ was grain boundary diffusion and movement. Therefore densification for 3Y-TZP progressed without grain growth, while enhanced grain growth was observed during densification for 8YSZ.

SiC dispersion strongly influenced on grain boundary diffusion due to the increase of the interface area between matrix and second phase which had low diffusivity, and the pinning effect. Thus 8YSZ incorporating finer SiC particles had finer and more homogeneous microstructure compared with monolith. For 3Y-TZP, which has fine microstructure intrinsically, the effects of second phase dispersion on densification and grain growth were small, compared with 8YSZ case.

Dispersed SiC particulate generated residual stresses and strains, which increase with increasing second phase content. SiC particles within matrix grains enhanced uniform stress and strain, while particles at grain boundary introduced nonuniform stress and strain. Therefore, nanocomposites, including numerous intragranular SiC particles, had higher uniform stress and strain than microcomposites, and then the lattice spacing for nanocomposites should be more expanded.

In Chapter 3, the mechanical properties at room temperature for 3Y-TZP/SiC and 8YSZ/SiC nano- and microcomposites were evaluated. The effects of SiC dispersion on the properties were investigated, and the effects of SiC particulate on the phase transformation were also studied for 3Y-TZP/SiC composites.

3Y-TZP/SiC composites

The fracture strength was not improved by dispersing SiC particles. This is attributed to grain growth during densification, because the high sintering temperature was necessary to densify composites due to the inhibition of grain growth for composites. The strength for microcomposites greatly decreased comparing with 3Y-TZP monolith.

The nano- and microcomposites had higher fracture toughness than monolith. For nanocomposites, the improvement in toughness is due to the increasing transformability and crack deflection by SiC particles. The increase in transformability is attributed to residual stresses by CTE mismatch between 3Y-TZP and SiC, and thus transformation from t-ZrO_2 to m-ZrO_2 was enhanced in composite cases. On the other hand, for microcomposites, the crack deflection, bridging by large SiC particles and microcrack are main toughening mechanism.

8YSZ/SiC composites

The fracture strength significantly improved from 300 MPa for 8YSZ monolith to 750 MPa for 8YSZ/20 vol% SiC nanocomposite due to fine and homogeneous microstructure by dispersing finer SiC particulate. It is suggested that finer SiC particles are more effective to improve the strength. The fracture toughness was also improved by adding SiC particles due to the crack deflection at the crack tip. The improvements in mechanical properties were also observed in microcomposite cases. The strength and toughness were 550 MPa and 3.1 $MPa\,m^{1/2}$, which is due to grain size refinement and crack bridging, respectively.

In Chapter 4, the high-temperature mechanical properties for 3Y-TZP monolith, 3Y-TZP/SiC nanocomposites, 8YSZ monolith and 8YSZ/SiC nanocomposites were evaluated. The effects of nano-sized SiC particulate on mechanical properties and plastic deformation were investigated.

3Y-TZP/SiC nanocomposites

The high-temperature strength was slightly improved, due to the increase in Young's modulus and the toughness by incorporating SiC particulate. The increase in the toughness should be attributed to the increase in Young's modulus, crack deflection and the residual stresses until the stresses were fully released. Furthermore, plastic deformation was suppressed due to inhibition of grain boundary sliding by SiC particles at grain boundaries.

8YSZ/SiC nanocomposites

The high-temperature strength for composites was improved by dispersing SiC particulate, which was caused by increase in Young's modulus, inhibitions of grain growth of matrix and SCG. 8YSZ/20 vol% SiC composite had more than 500 MPa in strength at 1200°C without the rapid decrease in the strength, thus, this materials can be expected to be used as a new structural material such as Al_2O_3 or Si_3N_4.

In Chapter 5, the ionic conductivity for 8YSZ monoliths and 8YSZ/SiC nano- and microcomposites were measured. The effects of SiC particles on grain boundary and lattice conductivity was investigated and obtained following results. Fine microstructure by dispersing SiC particles and SiC particles at grain boundary caused the decrease in the grain boundary conductivity, while nanocomposite system exhibited high lattice conductivity because of the residual stress induced by the CTE mismatch between matrix and dispersoid. 8YSZ composites with finer second phase dispersed have a possibility to possess not only high ionic conductivity, but also high fracture strength.

Finally, the conclusions in this work were summarized in this chapter. The disadvantages of both 3Y-TZP and 8YSZ can be improved by dispersing nano-sized SiC particles, therefore which will contribute to widen their applications, especially for 8YSZ. Mechanical properties for 8YSZ both at room and elevated temperatures were remarkably improved; the results obtained in this work revealed the possibility to new applications of 8YSZ as a structural material. Materials design for 8YSZ based composites adopted in this study is enabled to enhance not only high mechanical properties, but also high electrical properties

The author hopes that the results obtained in this study will be useful for material science and engineering in the future.

List of Publications

Papers

1) Fabrication and Mechanical Properties of Nano-Sized SiC Particulate Reinforced Yttria Stabilized Zirconia Composites
N. Bamba, Y. H. Choa and K. Niihara, Nanostructured Material, 9 (1997) 497-500.

2) Microstructure and Mechanical Properties of Yttria Stabilized Zirconia / Silicon Carbide Nanocomposites
N. Bamba, Y. H. Choa, T. Sekino and K. Niihara, J. Eur. Ceram. Soc., (in press).

3) Effect of Pure-Solvents Without Deflocculants for Finer SiC Particle Dispersed MgO Based Composite
Y. H. Choa, N. Bamba and K. Niihara, J. Mater. Sci. Lett., (in press).

4) Processing and Microstructure Development in Fine SiC Particle Dispersed MgO Based Composite
Y. H. Choa, N. Bamba, T. Sekino and K. Niihara, J. Am. Ceram. Soc., (in contribution).

5) Effects of Nano-sized Silicon Carbide Particulate on Microstructure and Ionic Conductivity of 8 mol% Yttria Stabilized Zirconia Based Nanocomposites
N. Bamba, Y. H. Choa, T. Sekino and K. Niihara, Solid State Ionics, (in preparation).

6) Size Effects of SiC Dispersion on Microstructure and Ionic Conductivity of 8 mol% Yttria Stabilized Zirconia"
N. Bamba, Y. H. Choa, T. Sekino and K. Niihara, (in preparation).

7) Mechanical Properties and Microstructure of 3 mol% Yttria Doped Zirconia / Silicon Carbide Nanocomposites
N. Bamba, Y. H. Choa, T. Sekino and K. Niihara, (in preparation).

8) High Temperature Mechanical Properties of 3Y-TZP / SiC Nanocomposites
N. Bamba, Y. H. Choa, T. Sekino and K. Niihara, (in preparation).

9) Size Effects of SiC dispersion on Mechanical Properties of 3Y-TZP
N. Bamba, Y. H. Choa, T. Sekino and K. Niihara, (in preparation).

Proceeding

10) Consolidation, Microstructure and Some Properties of Fully Stabilized Zirconia Based Nanocomposites
N. Bamba, Y. H. Choa, T. Sekino and K. Niihara, Proc. 6th Int'l Symp. Ceramic Materials & Components for Engines, (in press).

List of Supplementary Publications

Papers

1) A Superconducting Filter to Separate an Oxygen and Argon Mixture
Y. Sawai, N. Bamba, K. Ishizaki and S. Hayashi, J. Porous Materials, 2 (1995) 151-155.

2) The Effect of TiO_2 Addition on Strengthening and Toughening in Intragranular Type of 12Ce-TZP/Al_2O_3 Nanocomposites
M. Nawa, N. Bamba, T. Sekino and Koichi Niihara, J. Eur. Ceram. Soc., (in press).

Proceeding

3) Nanocomposite Structural Ceramics with Advanced Properties
K. Niihara, T. Sekino, Y. H. Choa, T. Kusunose, Y. Hayashi, K. Akamatsu, N. Bamba, T. Hirano and S. Ueda, Proc. 4th Japan International SAMPE Symposium, (1995) 394-399.

Acknowledgments

The author would like to express her gratitude to Professor Koichi Niihara at The Institute of Scientific and Industrial Research, Osaka University for his kind guidance, helpful suggestions and warm encouragement. The author would like to appreciate Professors Toshikazu Hirao and Seiichi Tagawa at Department of Materials Chemistry for reviewing this thesis and their helpful advice. The author wishes to express the deep appreciation to Dr. Satoru Ueda and Dr. Tohru Sekino and Mr. Atsuo Koreeda, and special thanks to Dr. Yong-Ho Choa at Niihara Laboratory.

The author wishes to make grateful acknowledgment to Professor Kozo Ishizaki at Department of Mechanical Engineering in Nagaoka University of Technology (NUT) for giving the opportunity to come to Osaka University and his hearty encouragement.

The author thanks to Professor Katsuaki Suganuma, Professor Yoshihiko Hirotsu at Osaka University, Professor S. W. Lee at Sun Moon University, Dr. Takeshi Hirano at the Japan Defense Agency and Mr. Masaki Yasuoka at National Industrial Research Institute of Nagoya and Mr. Masahiro Nawa at Matsushita Electric Works, Ltd. for their helpful advice.

Acknowledgments are given to Professor Ginya Adachi and Mr. Kobayashi, Dr. kenichi Ota at Osaka University for the impedance measurement and helpful advice and Mr. Hiroyuki Hayashi at Niihara Laboratory for the TEM observation. The author appreciated to Dr. Atsushi Nakahira at Kyoto Institute of Technology for his helpful guidance and encouragement.

Acknowledgments are made to Mmes. Emiko Kitaura and Rie Suehiro for their hearty encouragement and helpful assistance. The author thanks to the author's colleagues Mr. Young-Keun Jeong, Mr. Yoshikazu Suzuki and all other members of Niihara Laboratory for their friendships and helps.

The author also thanks to Dr. Koji Watari at National Industrial Research Institute of Nagoya, Dr. Yuichi Sawai at Hitachi, Dr. Makoto Nanko at Tokyo Institute of Technology, Dr. Tomohiro Yanai at the Japan Defense Agency, Dr. Naruki Saito at INAX and Mr. Yoshiaki Kinemuchi at NUT. The author thanks all of her friends.

Financial supports from Fellowship of Hosokawa Powder Technology Foundation in Japan is greatly appreciated.

Finally, the author is much indebted to the author's parents, grand mother and sister, Yoshio Bamba, Toshi Bamba, Ishi Bamba and keiko Bamba for their hearty encouragements, understanding and support.

Noriko Bamba

January, 1998
Osaka, Japan